UNIVERSITY OF CALIFORNIA, SAN DIEGO

Understanding the Surface and Interface Properties of Electrode Materials in Alkali-ion Batteries

--- A Combination of Experimental and Computational Studies

A dissertation submitted in partial satisfaction of the requirements for the degree

Doctor of Philosophy

in

Nanoengineering

by

Danna Qian

Committee in charge:

Ying Shirley Meng, Chair
Gaurav Arya
Renkun Chen
Miaofang Chi
Eric Fullerton
John Weare

2015

The Dissertation of Danna Qian is approved, and it is acceptable in quality and form for publication on microfilm and electronically:

Chair

University of California, San Diego

2015

TABLE OF CONTENTS

SIGNATURE PAGE.....iii

TABLE OF CONTENTS.....iv

LIST OF FIGURES.....vii

LIST OF TABLES.....xii

ACKNOWLEDGEMENTS.....xiii

VITA.....xvi

ABSTRACT OF THE DISSERTATION.....xviii

1 INTRODUCTION TO HIGH-ENERGY HIGH-POWER CATHODE MATERIAL FOR LITHIUM ION BATTERIES.....1

1.1 Lithium Ion Batteries 1
1.2 High-energy high-power cathode materials in Li-ion batteries 3
1.3 Interface and surfaces.....4
1.4 Objectives and overview.....5

2 FIRST PRINCIPLES METHOD AND ITS APPLICATION ON ALKALI-ION BATTERY MATERIALS.....8

2.1 Thermodynamics of intercalation materials.....8
2.2 First principles energy calculations.....9
2.2.1 General energy approximation.....9
2.2.2 Density-functional theory.....10
2.2.3 Generalized gradient approximation.....10
2.2.4 Pseudopotential approximation.....11
2.3 Surface and interface energy calculations.....12

3 ADVANCED ANALYTICAL ELECTRON MICROSCOPY FOR ALKALI-ION BATTERIES.....16

3.1 Introduction.....16
3.2 Recent progress in TEM.....17
3.3 High resolution electron microscopy for battery materials.....19
3.3.1 Electrodes.....19

3.3.2 Electrolyte....25
3.4 Dynamic/In-situ electron microscopy for battery research....28
3.4.1 Open-cell configuration....29
3.4.2 Liquid-cell configuration....31
3.4.3 All-solid-state micro-battery....32
3.5 Conclusions and perspectives....34

4 ELECTRON SPIN TRANSITION IN NANO-SIZE STOICHIOMETRIC $LiCoO_2$ AND ITS APPLICATIONS IN OXYGEN EVOLUTION REACTION / OXYGEN REDUCTION REACTION (OER/ORR) CATALYTIC PROCESS....42

4.1 Electron spin transition in nano-size stoichiometric LCO....42
4.1.1 Introduction....42
4.1.2 Methodologies....43
4.1.2.1 Computation....43
4.1.2.2 Synthesis....44
4.1.2.3 XRD....45
4.1.2.4 XPS....45
4.1.2.5 ^{7}Li NMR....45
4.1.2.6 Fitting Equation for the Curie Constant....46
4.1.3 Results and Discussions....46
4.1.4 Conclusions....52

4.2 The application of surface-spin-transitioned nano-size stoichiometric LCO in OER/ORR catalytic process....53
4.2.1 Introduction....53
4.2.2 Methodologies....54
4.2.2.1 Electrochemical measurements....54
4.2.2.2 TEM....54
4.2.2.3 EELS....55
4.2.3 Results and Discussions....55
4.2.4 Conclusions....58

5 UNCOVERING THE ROLES OF OXYGEN VACANCY ON CATION MIGRATION IN LITHIUM EXCESS LAYERED OXIDES....77

5.1 Introduction....77
5.2 Methodologies....78
5.2.1 STEM/EELS....78
5.2.2 Computation....79
5.3 Results and Discussions....80
5.4 Conclusions....85

6 SURFACE COATING ON CATHODE MATERIALS IN LIB.....91

6.1 Lithium lanthanum titanium oxides: a fast ionic conductive coating for lithium-ion battery cathodes.....91
6.1.1 Introduction.....91
6.1.2 Methodologies.....93
6.1.2.1 Computational methods.....93
6.1.2.2 Experimental methods.....94
6.1.2.3 Electrochemical characterization.....95
6.1.3 Results.....96
6.1.3.1 Computational results.....96
6.1.3.2 Experimental results.....98
6.1.4 Discussions.....103
6.1.5 Conclusions.....106

6.2 AlF_3 coating for lithium-ion battery cathodes.....106
6.2.1 Introduction.....106
6.2.2 Methodologies.....108
6.2.2.1 TEM.....108
6.2.2.2 a-STEM/EELS.....108
6.2.3 Results and Discussions.....109
6.2.4 Conclusions.....111

7 STEM/EELS STUDY OF P2-$Na_{2/3}[Fe_{1/3}Mn_{2/3}]O_2$.....122

7.1 Introduction.....122
7.2 Methodologies.....123
7.3 Results and Discussions.....124
7.4 Conclusions.....125

8 SUMMARY AND FUTURE WORK.....130

8.1 Summary.....130
8.2 Future work.....131
8.2.1 Surface and interface properties of Na based electrode materials....131
8.2.2 Computational study on layer/spinel and layer/rocksalt interface....132

REFERENCES.....133

LIST OF FIGURES

Figure 1.1: Working principles of LIB (charging) 6

Figure 1.2: Theoretical and practical gravimetric energy densities of different cathode materials.....6

Figure 1.3: Crystal structure of layered $LiMO_2$ (Blue: transition metal ions; Red: Li ions) 7

Figure 2.1: Three types of Tasker ionic crystal surfaces.....15

Figure 2.2: Schematic plot of surface and bulk.....15

Figure 3.1: Overview of the implementation of TEM in AIB.....36

Figure 3.2: HAADF STEM images of Li-excess materials (a) pristine and (b) after cycling; (c) &(d) EELS comparison of pristine and cycled surface and bulk; (e) Spatial resolved O K-edge EELS from surface to bulk in cycled Li-excess.....37

Figure 3.3: (a) Top: Schematic figure of the probable configuration of Fe_{Li} with a higher Fe oxidation state. Bottom: (Left) EELS data of Fe_{Li} and the Fe in bulk. (Right) Compared L3/L2 ratio with reference different iron compounds; (b) ABF image of half charged state showing the Li staging.....38

Figure 3.4: (a) HAADF and (b) ABF of local clustering of A-site vacancies and O4 square window lithium. (c) HAADF STEM images of a LLTO grain boundary. EELS data of (d) Li K edge, (e) Ti L edge for the grain boundary and the bulk.....39

Figure 3.5: (a) Schematic of the volatile cell set up; (b) a high density of dislocations emerging from the reaction front was revealed in single SnO_2 nanowire.....40

Figure 3.6: (a) Experimental set up of non-volatile cell set up with liquid electrolyte; (b) & (c) in-situ observation of inhomogeneous lithiation, lithium metal dentritic growth and solid-electrolyte interface formation; (d) an example of all-solid-state battery.....41

Figure 4.1: (a) {104} and (b) {110} surfaces of $LiCoO_2$ (c) Octahedrally, square pyramid and pseudo-tetrahedrally coordinated Co ions. (red- oxygen, green – lithium, blue Co).....60

Figure 4.2: Spin density plot of the {104} plane of the bulk (a) and the surface (b). (Notice the scale differences in the spin density).....60

Figure 4.3: (a) XRD and (b) XPS spectra of nano-sized stoichiometric $LiCoO_2$.....61

Figure 4.4: ^{7}Li MAS NMR spectra of $LiCoO_2$ with varying particle sizes. (a) Percentages of the Li near by low spin Co (III) in $LiCoO_2$ are listed in (a). Peak assignment and percentages of Li ions in environments nearby paramagnetic ions can be found in enlarged spectra. (b) Asterisks 62

Figure 4.5: (a) Molar magnetic susceptibilities of particle size 10nm, 16nm, 20nm, 30nm and 40nm samples as a function of temperature. (b) The Curie constants of these samples determined from the $1/\chi$ vs T. (Both are measured with sample holder corrected).....62

Figure 4.6: Projected density of states (DOS) of Co ions on the surface and bulk of $LiCoO_2$. Upper: {104} surface Co with IS (left) and bulk Co with LS (right); Bottom: {110} Surface Co with IS (left) and Bulk Co with LS (right).....63

Figure 4.7: Electrochemical data for both bulk-$LiCoO_2$ (black) and 10nm-$LiCoO_2$ (red) in a lithium half-cell.....64

Figure 4.8: (a) Representative TEM image of a nanorod from the $LiCoO_2$ sample with an average rod diameter of 40 nm. (b) High-resolution TEM image of a representative nanorod $LiCoO_2$ with its associated selected-area electron diffraction pattern. (c) Histograms of the length and diameter distributions...65

Figure 4.9: (a)(b) Representative EELS spectra of pristine 9-nm $LiCoO_2$: (a) Co L edge, (b) O K edge. (c)-(e) Two types of representative EELS spectra of 9-nm sample held at 0.7 V vs. RHE for ORR. Middle row is one set of (c) Co L edge and (d) O K edge (case 1); bottom row (e) and (f) is the other set.....66

Figure 4.10: (a) Cyclic voltammetry of ORR current of different $LiCoO_2$ samples in O_2-saturated 0.1 M KOH at 10 mV/s. (b) Potentiostatic measurements of OER current of different $LiCoO_2$ samples in O_2-saturated 0.1 M KOH at different voltages. (c-f) Tafel plots of ORR and OER activities.....67

Figure 4.11: (a) CV curves of different Co compounds in the Co redox region. (b) Calculation scheme of charge transfer during Co 2+/3+ and 3+/4+ redox reactions by integrating the redox peaks. (c) Charge transferred per surface area of tip and side surfaces of $LiCoO_2$ during 2+/3+ and 3+/4+ redox.....68

Figure 4.12. Two types of representative EELS spectra of 9 nm sample held at 1.55 V vs. RHE for OER. Upper row is one set of (a) Co L edge and (b) O K edge (case 1); bottom row (c) and (d) is the other set of spectra (case 2).....69

Figure 4.13. Representative EELS spectra of 9 nm sample that was immersed in 0.1 M KOH electrolyte for 1 hour without applying any potential. Then sample was rinsed by DI water and tried in air at room temperature. These spectra were taken under 300 kV. (a) Co L edge and (b) O K edge.....69

Figure 5.1: Spatial resolved O K-edge EELS spectra from bulk to surface.....87

Figure 5.2: (a) Atomic configurations of $Li[Li_{1/6}Ni_{1/4}Mn_{7/12}]O_2$; (b) Oxygen vacancy formation energy vs. Li concentration.....88

Figure 5.3: Ni diffusion barriers with oxygen vacancies in different positions at $Li_{15/28}Ni_{1/4}Mn_{7/12}O_2$.....89

Figure 5.4: Calculated Ni diffusion barriers with oxygen vacancies in different positions at $Li_{20/28}Ni_{1/4}Mn_{7/12}O_2$ 89

Figure 5.5: Neighboring TM valence change after introduction of oxygen vacancy at $Li_{20/28}Ni_{1/4}Mn_{7/12}O_2$.....90

Figure 5.6: Mn diffusion barriers with oxygen vacancies in different positions at $Li_{20/28}Ni_{1/4}Mn_{7/12}O_2$.....90

Figure 6.1: Computational model structure of $Li_{0.125}La_{0.625}TiO_3$(a) and $Li_{0.35}La_{0.55}TiO_3$ (d). Planes of interest used in NEB calculation of low lithium concentration

(b) and high lithium concentration (e). (c) and (f) are the after relaxation structure of planes in (b) and (e) respectively.....112
Figure 6.2: (a) x=3/4 plane of low lithium concentration with all equilibrium states and middle images. Two crosses are the images between Li1 and Li2, Li2 and Li3 respectively. (Other images can get from symmetry). (b) (c) Illustration of vertical oxygen square window.....113
Figure 6.3: Estimated Li diffusion path in La-poor layer (green dash lines) in low lithium concentration scenario (a) and high lithium concentration scenario (b).....114
Figure 6.4: Structural characterization of pristine and LLTO coated samples. (a) (b) and (c)(d) are the SEM images of pristine and LLT5, respectively; (e) (f) and (g) are EDS results of pristine, LLT1 and LLT5, respectively. The inset in (c) and (d) is the TEM image of LLT5.....115
Figure 6.5: (a) XRD results of pristine, LLT1, LLT2, and LLT5. (b) Zoom in of 23° ~ 26.5°. (c) Zoom in of 30.5° ~ 34.5°.....116
Figure 6.6: Electrochemical cycling and rate capability of pristine and coated electrodes. (a) Cycling retention properties of pristine, LLT1, LLT2 and LLT5. Rate capability of pristine (b) and LLT1 (c).....117
Figure 6.7: (a) Calculated Li ion diffusion coefficient of pristine (black) and LLT1 (red) from PITT tests. Impedance spectra (100kHz – 100mHz) of pristine (b) and LLT1 (c) obtained from the cell at 4.2V. Dashed lines are the CNLS fittings of the impedance spectra of the equivalent circuit model.....117
Figure 6.8: EELS mapping of LLT5 (a) before and (b) after cycling. Green: Li; Blue: La; Red: Ti.....118
Figure 6.9: The TEM and STEM of LNMO and NALNMO, a) TEM of LNMO, b) and c) TEM of NALNMO, d) STEM of NALNMO.....119
Figure 6.10: High-resolution S/TEM images of the bulk and surface of NALNMO.....120
Figure 6.11: The STEM of NALNMO with step scan of Mn EELS L edge and O EELS K edge.....120
Figure 7.1: HAADF and ABF images of pristine P2-$Na_{2/3}[Fe_{1/3}Mn_{2/3}]O2$.....127

Figure 7.2: [001] zone axis ED of pristine, charged and discharged sample.....127
Figure 7.3: EELS spectra comparison of pristine, charged and discharged sample.....128
Figure 7.4: Mechanism figure.....128

LIST OF TABLES

Table 4.1: Synthesis conditions and altered parameters to give the desired stoichiometric $LiCoO_2$ particle size. 70

Table 4.2: Rietveld Refinement fit parameters and the calculated *a* and *c* lattice parameters for the various sized stoichiometric $LiCoO_2$ nanoparticles.....71

Table 4.3: Calculated surface energy w/o spin transition compared with literature.....72

Table 4.4: The mass-normalized tip, side and total surface areas of each $LiCoO_2$ sample, computed using the particle size distributions collected from TEM images.....73

Table 4.5: The O K pre-peak area of tips and sides.....74

Table 4.6: The mass-normalized and total-surface normalized charge transfer during Co 2+/3+ and 3+/4+ redox processes of each $LiCoO_2$ sample.....75

Table 4.7: The Co L3/L2 ratios of tips and sides.....76

Table 6.1: List of the layer sequence of three models and energy values obtained after relaxation.....121

Table 7.1: EELS quantification of Fe and Mn oxidation states for pristine, charged and discharged samples.....129

ACKNOWLEDGEMENTS

First of all, I would like to thank my thesis advisor Dr. Ying Shirley Meng for providing me all the opportunities to do this research and her continuous support, and good advice throughout the projects. I was sincerely honored to meet and work with her. I shall never forget her endless advice and help. I would also like to thank my other advisor during my ORNL stay, Dr. Miaofang Chi for her support and advice. I would like to express the deepest gratitude to my other committee members: Dr. Gaurav Arya, Dr. Renkun Chen, Dr. Eric Fullerton, Dr. John Weare for their time and guidance.

Secondly, I would like to acknowledge my collaborators and co-authors in UCSD, Dr. Bo Xu, Dr. Kyler Carroll, Dr. Christopher R. Fell, Dr. Dhamadaran Santhanegopalan Hyung-man Cho and Haodong Liu in LESC group as well as all other collaboration works. I am also grateful to all the group mates in LESC who have helped and inspired me in many ways.

Finally, I would like to express my thanks to my collaborators and co-authors outside LESC, Alex Han, Dr. Marcel Risch and Dr. Yang Shao-Horn from MIT, Dr. Clare P. Grey at University of Cambridge, Dr. Hailong Chen from Georgia Tech, Dr. Cheng Ma and Dr. Karen More from Oak Ridge National Laboratory for their invaluable help throughout the projects.

Chapter 1, in part, is a reprint of the material "Recent progress in cathode materials research for advanced lithium ion batteries", as it appears in Materials Science and Engineering R, 73(5-6), 51-65, by Bo Xu, Danna Qian, Ziying Wang, Ying Shirley Meng, 2012. The dissertation author was the co-primary investigator and author of the paper.

Chapter 3, in full, is a reprint of the material "Advanced analytical electron microscopy for alkali-ion batteries", as currently prepared for publication. The dissertation author was the primary investigator and author of this paper. Most of the writing was conducted by the author.

Chapter 4, part 1, in full, is reprinted with permission from the following paper "Electronic spin transition in nanosize stoichiometric lithium cobalt oxide", Journal of the American Chemical Society, 2012, 134(14), 6096-6099 by Danna Qian, Y. Hinuma, H. Chen, L-S Du, K. Carroll, G. Ceder, C. P. Grey, Y. S. Meng, Copyright (2012) American Chemical Society. The second part, in part, is reprint from "The role of $LiCoO_2$ surface termination in oxygen reduction and evolution kinetics" being submitted by B. Han, Danna Qian (equally contributed), M. Risch, H. Chen, M. Chi, Y. S. Meng, Y. S-H.. The dissertation author was the primary investigator and author of the papers.

Chapter 5, in full, is a reprint of the material "Uncovering the roles of oxygen vacancies in cation migration in lithium excess layered oxides", Phys. Chem. Chem. Phys., 2014, 16, 14665, reproduced by permission of the PCCP Owner Societies. The dissertation author was the primary investigator and author of the paper.

Chapter 6, Part 1, in full, is a reprint with the permission of the material "Lithium lanthanum titanium oxides: a fast ionic conductive coating for lithium-ion battery cathodes", Chemistry of Materials, 2012, 24(14), 2744, by Danna Qian, B. Xu, H. -M. Cho, T. Hatsukade, K. J. Carroll, Y. S. Meng, Copyright (2012) American Chemical Society. The dissertation author is the primary investigator and author of the material. Part2, in part, is a reprint of the material "Understanding the role of NH_4^+ and Al_2O_3

surface co-modification on lithium-excess layered oxide $Li_{1.2}Ni_{0.2}Mn_{0.6}O_2$" prepared for publication. The dissertation author is the primary investigator and author.

Chapter 7, in full, is a reprint of the material "STEM/EELS study of P2-$Na_{2/3}[Fe_{1/3}Mn_{2/3}]O_2$", which is in preparation for submission. The dissertation author is the primary investigator and author.

I would like to acknowledge the financial support from Northeastern Center for Chemical Energy Storage (NECCES), an Energy Frontier Research Center funded by the U. S. Department of Energy, and Advanced Short-Term Research Opportunity (ASTRO) program in ORNL. I would like to acknowledge Texas Advanced Computer Center for providing computation resources.

For the last but not least, my deepest gratitude to my parents, Xiaoman Qian and Xiaochun Yu, my husband, Ying Chen and the baby we are expecting. Their love, patience and unselfish support make everything possible.

VITA

2009	B. S. in Chemistry	University of Science and Technology of China
2015	Ph. D. in Nanoengineering	University of California, San Diego, USA

PUBLICATIONS

1. **Danna Qian**, B. Xu, H-M Cho, T. Hatsukade, K. Carroll, Y. S. Meng*, "Performance Improvement in Lithium Lanthanum Titanate Coated $LiNi_{0.8}Co_{0.15}Al_{0.05}O_2$--- A combination of first-principles calculations and experimental studies", Chemistry of Materials, 2012, 24(14), 2744-2751
2. **Danna Qian**, Y. Hinuma, H. Chen, L-S Du, K. Carroll, G. Ceder, C. P. Grey, Y. S. Meng*, "Electronic spin transition in nanosize stoichiometric lithium cobalt oxide", Journal of the American Chemical Society, 2012, 134(14), 6096-6099
3. B. Xu, **Danna Qian**, Z. Wang, Y. S. Meng*, "Recent Progress in Cathode Materials Research for Advanced Lithium Ion Batteries", Materials Science and Engineering R, 2012, 73(5-6), 51-65
4. K. Carroll, **Danna Qian**, C. Fell, S. Calvin, G. M. Veith, M. Chi, L. Baggetto, Y. S. Meng*, "Probing the electrode/electrolyte interface in the Li-excess material $Li_{1.2}Ni_{0.2}Mn_{0.6}O_2$ ", Phys. Chem. Chem. Phys., 2013, 15, 11128
5. C. Fell, **Danna Qian**, K. Carroll, M. Chi, J. L. Jones, Y. S. Meng*, "Correlation between oxygen vacancy, microstrain and cation distribution in Lithium-excess layered oxides during the first electrochemical cycle", Chem. Mater., 2013, 25(9), 1621-1629
6. Y. Janssen, D. Santhanagopalan, **Danna Qian**, M. Chi, X. Wang, C. Hoffman, Y. S. Meng and P. Khalifah*, "Reciprocal Salt Flux Growth of LiFePO4 single crystals with Controlled Defect Concentrations", Chem. Mater., 2013, 25(22), 4574
7. D. Santhanagopalan, **Danna Qian**, T. Mcgilvary, Z. Wang, F. Wang, F. Camino, J. Graetz, N. Dudney, Y. S. Meng*, "Interface limited lithium transport in all-solid-state nano-batteries", J. Phys. Chem. Lett., 2014, 5, 298
8. **Danna Qian**, N. Hagh, Y. S. Meng*, "Insight into designing high-energy high-power cathode material for lithium ion batteries", ECS Electrochemistry Letters, 2014, 3(7), A72
9. **Danna Qian**, B. Xu, M. Chi, Y. S. Meng*, "Uncovering the roles of oxygen vacancy on cation migration in lithium excess layered oxides", Phys. Chem. Chem. Phys., 2014, 16, 14665
10. **Danna Qian**, C. Ma, K. More, Y. S. Meng, M. Chi*, "Advanced analytical electron microscopy for alkaline ion batteries", In preparation
11. Y.-S. Yu, C. Kim, D. Shapiro, M. Farmand, **Danna Qian**, T. Tyliszczak, D. Kilcoyne, S. Marchesini, J. Joseh, P. Denes, T. Warwick, F. Strobridge, C. P. Grey, H. Padmore, Y. S. Meng, R. Kostecki, J. Cabana*, "Effect of crystal size on the nanoscale chemical phase distribution and fracture in Li_xFePO_4", Submitted.
12. **(Equal contribution)** B. Han†, **Danna Qian**†, M. Risch, H. Chen, M. Chi, Y. S. Meng*, Yang Shao-Horn*, "The Role of LiCoO2 Surface Termination in Oxygen Reduction and Evolution Kinetics", Submitted.

13. H. Liu, **Danna Qian**, M. Zhang, K. Carroll, L. Baggetto, K. An, M. Chi, Y. Chen, D. Lau, G. Veith, Y. S. Meng*, "Understanding the role of NH_4^+ and Al_2O_3 surface co-modification on lithium-excess layered oxide $Li_{1.2}Ni_{0.2}Mn_{0.6}O_2$", In preparation
14. Q. Bao, M. Zhang, L. Wu, Y. Xia, J. Wang, **Danna Qian**, H. Liu, Y. S. Meng*, Y. Zhu, Z. Liu*, "Gas-solid interface reactivation of lithium-rich layered cathode with high capacity and improved rate capability for lithium-ion battery", In preparation.
15. H. Liu, Y. Chen, K. An, S. Venkatachalam, **Danna Qian**, M. Zhang, Y. S. Meng*, "Probing the actives of Li and O in advanced Li-ion batteries via *In-operando* neutron diffraction", In preparation.
16. **D. Qian**, C. Ma, J. Xu, K. More, Y. S. Meng, M. Chi*, "STEM/EELS study of P2-$Na_{2/3}[Fe_{1/3}Mn_{2/3}]O_2$", In preparation.

ABSTRACT OF THE DISSERTATION

Understanding the Surface and Interface Properties of Electrode Materials

in Alkali-ion Batteries

--- A Combination of Experimental and Computational Studies

by

Danna Qian

Doctor of Philosophy in NanoEngineering

University of California, San Diego, 2015

Professor Ying Shirley Meng, Chair

In order to realize the commercialization of alkali-ion batteries (AIB) in electric vehicles and smart grid systems, further improvements are demanded in multiple aspects, especially the energy/power density, safety and cycle life. Due to the complexity of the system, besides each separate component, surface and interface are critical in understanding and optimizing the system.

In this dissertation, systematic studies are performed on the nanosizing effect, the surface phase transformation and surface coating of Li-intercalation cathode materials by a combination of first principles and experimental studies. In the first part, the surface spin transition of $LiCoO_2$ (LCO) was found based on first principles calculations. Different sizes of LCO were synthesized and the spin transition on the surface was

confirmed by other characterization techniques. The OER/ORR activities profoundly increased at the spin-transited surfaces. The study shed lights on the electronic properties tuning in nanosizing process, which would affect functional properties.

In the second part, the structural and chemical evolutions during electrochemical process of the Li-excess compound was probed by a combination of high-end characterization techniques especially STEM/EELS. A second phase generation together with oxygen vacancy formation and microstrain formation was found at the first cycle plateau region. A novel oxygen vacancy assisted transition metal migration mechanism was proposed using first principles calculations. These findings lead to an increased understanding of the performance fading mechanism of Li-excess family compounds, providing new insights in optimization their rate performances.

In the third part, the surface coating of LLTO has been investigated for an improved electrochemical performance of the NCA combining computation with other electrochemical tests. The good ionic conductor LLTO increases the system's ion conductivity thus the electrochemical performance. Similar investigations have also been carried out in AlF_3 coatings. These studies help the understanding of coating effect of electrode materials.

In the fourth part, a detailed STEM/EELS study on the P2 type Na cathode material was carried out.

1 INTRODUCTION TO HIGH-ENERGY HIGH-POWER CATHODE MATERIAL FOR LITHIUM ION BATTERIES

Lithium ion batteries (LIB), regarded as one of the near-term solutions for green energy storage, are well developed for portable electronic devices and have been widely used in the past twenty years. Recently, with the emerge of hybrid electric vehicles (HEV) and electric vehicles (EV) such as Toyota Prius, Nissan Leaf, Tesla etc., increasing effort has been focused on improving the energy/power density, cycling life and safety issues of the system. Further development on LIB system and materials is thus necessary and urgent.

1.1 Lithium ion batteries

A lithium ion battery can work as the energy storage device by converting electric energy into electrochemical energy. The basic working principles of LIB are shown in Figure 1.1. There are three key components in a LIB system: cathode, anode and electrolyte. For today's commercialized LIB system, both cathode and anode materials are intercalation materials. The transition metal oxides in cathode (graphite in anode) consist of a largely unchangeable host with specific sites for Li ions to be intercalated in. All Li ions are in the cathode sides initially and the battery system is assembled in "discharged" status. While charging, Li ions are extracted from the cathode host, solvate into and move through the non-aqueous electrolyte, and intercalate into the anode host. Meanwhile, electrons also move from cathode to anode through the outside current collectors forming an electric circuit. The chemical potential of Li is much higher in the anode than in the cathode, thus the electric energy is stored in the form of

(electro)chemical energy. Such process is reversed when the battery is discharging where the electrochemical energy is released in the form of electric energy. The cathode region and anode region are separated by the separator, a micro-porous membrane that allows the electrolyte to penetrate and prevent shorting between the two electrodes. The electrolyte should be ionically conducting and electronically insulating in principle, however the actual properties of the electrolyte is much more complicated. During the first cycle, a so-called solid-electrolyte-interphase (SEI) layer will be formed on the surface of electrodes due to the decomposition of organic electrolyte at extreme voltage range (typically <1.2V or >4.6V). In current LIB technology, the cell voltage and capacities are mainly determined by the cathode material that is also the limiting factor for Li transportation rate. The developments of cathode materials therefore become extremely crucial and receive much attention in recent decade.

Since 1980 when the $LiCoO_2$ was demonstrated firstly as a possible cathode material for rechargeable lithium battery, the transition metal intercalation oxides have caught the major research interests as the LIB cathodes. Categorized by structure, the conventional cathode materials include layered compounds $LiMO_2$(M = Co, Ni, Mn etc.), spinel compounds LiM_2O_4(M=Mn etc.), and olivine compounds $LiMPO_4$(M = Fe, Mn, Ni, Co etc.). Most of the researches are performed on these materials and their derivatives. New structure intercalation materials such as silicates, borates and tavorites are also gaining increasing attentions in recent years. During the materials optimization and development, following designing criterions are often considered: 1) Energy density; 2) Rate capability; 3) Cycling performance; 4) Safety; 5) Cost. The energy density is determined by the material's reversible capacity and operating voltage, which are mostly

determined by the material intrinsic chemistry such as the effective redox couples and maximum lithium concentration in active materials. For rate capability and cycling performances, electronic and ionic mobilities are key determining factors, though particle morphologies are also important factors due to the anisotropic nature of the structures and are even playing a crucial role in some cases. Figure 1.2 compared the gravimetric energy densities of different cathode materials that are currently under investigations. While some materials such as $LiFeBO_3$ and $LiFeSO_4F$ are already approaching their theoretical energy densities, for other materials including conventional layered and spinel compounds, significant gaps are still present between their theoretical and practical energy densities. These materials with promising theoretical properties have high potentials as the candidates of future generation LIB cathode; however, their rate capacity and cycling performances still need much improvement before they can be commercialized.

1.2 High-energy high-power cathode material in Li-ion batteries

From the first commercialized cathode material $LiCoO_2$ to the current one of the best candidate for EV applications, Li-excess materials, they all adopted a layered structure. The ideal structure of layered compound $LiMO_2$ is demonstrated in Figure 3. The oxygen anions (omitted for clarity in the figures) form a close-packed fcc lattice with cations located in the 6-coordinated octahedral crystal site. The MO_2 slabs and Li layers are stacked alternatively. Although the conventional layered oxide $LiCoO_2$ has been commercialized as the LIB cathode for twenty years, it can only deliver about 140mAh/g capacity, which is half of its theoretical capacity. Such limitation can be attributed to the

intrinsic structural instability of the material when more than half of the Li ions are extracted. On the other hand, the presence of toxic and expensive Co ions in $LiCoO_2$ has introduced the environmental problem as well as raised the cost of the LIB.

For improvement, Co ions in $LiCoO_2$ can be substituted by other transition metal ions such as Ni and Mn. The new substitutions can reduce the cost of the materials and make the materials more environmentally friendly by eliminating the use of Co ions, which are expensive and toxic. One of the most promising candidates is so-called Li-excess nickel manganese layer oxides $Li[Ni_xLi_{1/3-2x/3}Mn_{2/3-x/3}]O_2$. The compounds were first reported in 2001 and can be expressed as a composite of two end members of $Li[Li_{1/3}Mn_{2/3}]O_2$ and $LiNi_{1/2}Mn_{1/2}O_2$. A reversible capacity as high as 250mAh/g can be obtained routinely.

1.3 Surfaces and Interfaces

Upon electrochemical cycling, significant variations in structures and chemical distributions occur, including ion relocation, lattice expansion/contraction, phase transition, and structure/surface reconstruction, etc. These variations could impose significant influence on ion/electron transportations, and thus the performance and lifetime of the whole system. In addition, the electrode consists of the active material, a good electronic conductor (graphite usually) and a binder. The interfaces in the active material and in between all the components are essential and most of the time limiting step of the ion/electron transportations.

Moreover, during the electrochemical performances, irreversible reactions occur simultaneously with the reversible Li shuffle in between the electrodes. For example, the

formation of a solid electrolyte interface (SEI), resulting from the decomposition of electrolytes on the surface of electrodes, would affect the kinetics of the system. Understanding surface and interface properties are essential for the system optimization.

1.4 Objectives and overview

The objective of this research project is to understand the surface and interface properties of electrode materials in alkali-ion batteries using a combination of first principles computational methods and experimental characterization techniques. The project can be divided into four parts:

Part 1: Study the surface electronic and chemical properties during nanosizing effect and the associated increased functional capabilities

Part 2: Study the surface and interface structural and chemical evolution during electrochemical cycling and mechanism associated

Part 3: Study the coating effect on the electrode materials

Part 4: Study a new system in Na ion batteries

Chapter 1, in part, is a reprint of the material "Recent Progress in Cathode Materials Research for Advanced Lithium Ion Batteries", as it appears in Materials Science and Engineering R, 73(5-6), 51-65, 2012. Bo Xu, Danna Qian, Ziying Wang, Ying Shirley Meng, 2012. The dissertation author was the primary investigator and author of this paper.

Figures:

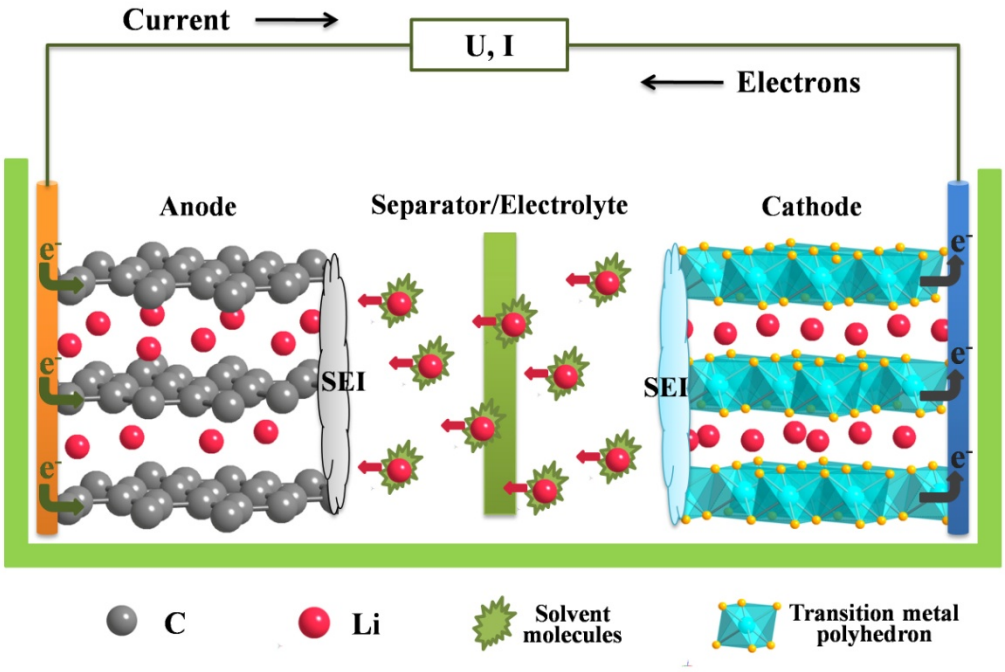

Figure 1.1: Working principles of LIB (charging)

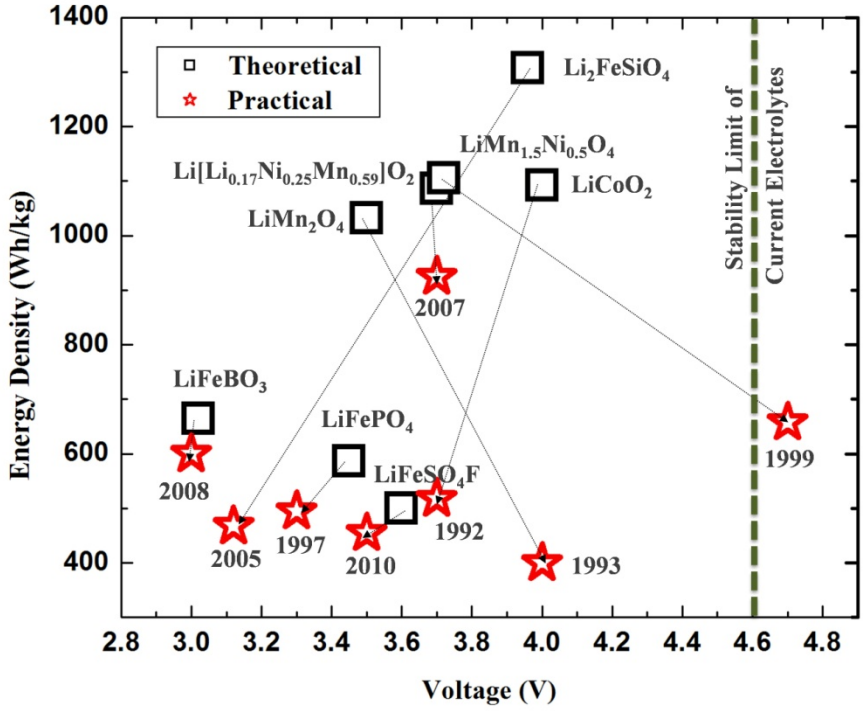

Figure 1.2: Theoretical and practical gravimetric energy densities of different cathode materials

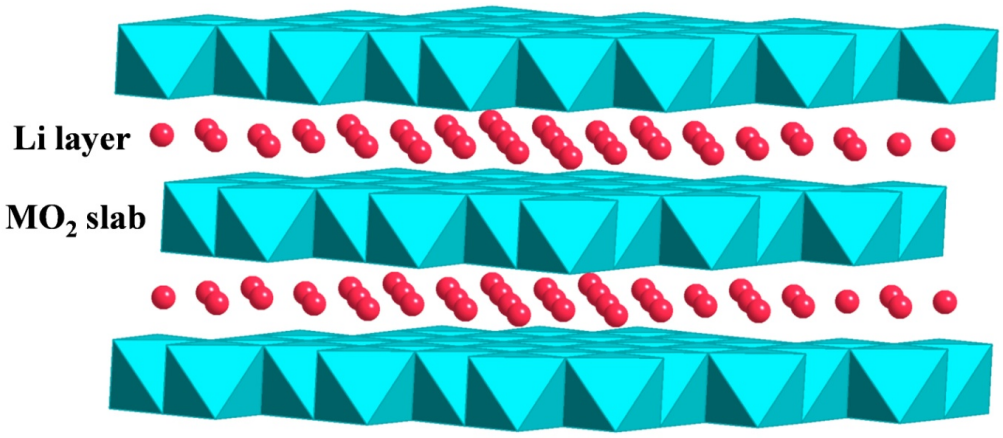

Figure 1.3: Crystal structure of layered $LiMO_2$ (Blue: transition metal ions; Red: Li ions)

2 FIRST PRINCIPLES METHOD AND ITS APPLICATION ON THERMODYNAMIC PROPERTIES OF INTERCALATION MATERIALS

2.1 Thermodynamics of intercalation materials

In intercalation material LiM, where M is the host structure and Li is the mobile ions, the following reaction happens during electrochemical charging/discharging:

$$LiM - xe^- \Leftrightarrow Li_{1-x}M + xLi^+$$

The average voltage is therefore $V = \frac{\Delta G}{xze}$, where ΔG is the Gibbs free energy for the reaction, z is the valence of Li and e is the charge of the electron. Usually, the host structure M does not change during the charging/discharging process, therefore its chemical potential does not change. The electrochemical energy comes from the chemical potential difference of Li ions in both electrodes. The voltage therefore could be derived from the Nernst equation.

$$V(x) = -\frac{(\mu_{Li}^{cathode} - \mu_{Li}^{anode})}{ze}$$

Metal Li is always used as the counter electrode, μ_{Li}^{anode} is usually constant. From the knowledge of classical thermodynamics, the derivative of Gibbs free energy can be written as:

$$dG = Vdp - SdT + \sum \mu_i dN_i$$

Under the condition of constant pressure and temperature, the host structure does not change, therefore, the chemical potential of Li could be written as $\mu_{Li} = \left(\frac{\partial G}{\partial N_{Li}}\right)_{T,p,N_{host}}$, where N_{Li} is the number of lithium ions. The independent intensive variables of the system should be temperature T, pressure P, and the chemical potential μ. To investigate

the phase stability at different temperature or pressure, the characteristic potential should be grand canonical free energy rather than the Gibbs free energy. A Legendre transform is necessary that the grand canonical free energy

$$\Omega_{host} = G_{host} - N_{Li}\mu_{Li}$$

Since the host structure does not change, the number of host does not change. Therefore the formal transform can be rewritten as

$$\Omega_{host} = \frac{\Omega_{host}}{N_{host}} = \frac{G_{host} - N_{Li}\mu_{Li}}{N_{host}} = G_f^{host} = x\mu_{Li}$$

where x is regard as the Li concentration.

2.2 First principles energy calculations

2.2.1 General energy approximation

First principles theory is commonly used in the energy calculations. Also called as ab-initio, the theory starts directly at the level of the most basic physic laws, the atomic numbers and quantum mechanics. The Kohn-Sham energy function can be given that

$$E[\{\psi_i\}] = 2\sum_i \psi_i \left[-\frac{\hbar^2}{2m}\right]\nabla^2\psi_i d^3r + \int V_{ion}(r)\, n(r) d^3r + \frac{e^2}{2}\int \frac{n(r)n(r')}{|r-r'|} d^3r d^3r' + E_{XC}[n(r)] + E_{ion}(\{R_I\})$$

where $n(r) = 2\sum_i|\psi_i(r)|^2$ is the electronic density. On the right side of the equation, there are five terms that contribute to the total energy. The first item represents the electron kinetic energy from the original Schrödinger equation. The second term represents the electron-ion potential energy. The third term represents the electron-electron repulsion interactions. The forth term represents the exchange and correlations of

many-electron system beyond the direct coulomb repulsion. And the final term represents the coulomb interactions between different ions.

2.2.2 Density-functional theory

The density-functional theory (DFT) associates all the interactions to a uniform variable, the electronic charge density. The solution of the energy equation is obtained in a self-consistent way to ensure the accuracy. Since only the minimum of the solutions of the energy equation makes sense when investigate the ground state energy, the final term in above equation could be removed. Kohn-Sham equations therefore can be further simplified to

$$\left[-\frac{\hbar^2}{2m}\nabla^2 + V_{ion}(r) + V_H(r) + V_{XC}(r)\right]\psi_i(r) = \varepsilon_i\psi_i(r)$$

where $\psi_i(r)$ is the wave function of electronic state i. V_H is the Hatree potential of the electrons representing the electron-electron repulsion and V_{XC} is the exchange-correlation potential. All the potentials are equations related to the electronic charge density. Using self-consistent method, as long as the electronic charge density is obtained, the total energy could be calculated.

2.2.3 Generalized gradient approximation (GGA)

The major problem with DFT is that the exact functional for exchange and correlation are not known except for free electron gas. However, approximations exist which permit the calculation of certain physical quantities more accurately. The GGA, developed by Purdue and Yue, takes into account for the gradient of the density at the

same coordinate compared with local-density approximation (LDA). GGA has been proved to be more suitable in systems where the electronic states are highly localized in space, such as alkali transition metal oxides, most commonly used electrode materials. Moreover, in transition metal ions, the highly localized d electrons could cause the main error of the calculation accuracy because of the lack of cancellation of electron self-interaction. GGA + U method therefore is developed to circumvent this problem and is proved to be successful in Li intercalation materials.

2.2.4 Pseudopotential approximation

Besides the electron-electron interaction, the electron-ion interactions are also difficult to deal with because of the huge number of core-electrons of each ion. Since the core-electrons are tightly bonding with the nuclei, a large number of wave functions are needed for the fourier transformation, which will highly raise the cost of computation. It is necessary to do the full electron calculation if dealing with the fine electronic structure of the materials. However, most of the time, the major physical properties of the materials are determined by the valence electrons, which is usually no more than eight. The pseudopotential approximation is developed so that all the core-electrons are simplified as a core and the ion is divided into two parts, the "core" and the valence electrons. A local pseudopotential is set up that it will be exactly the same with the core electron potential beyond a critical distance r_c from the nuclei.

On one hand, the consistence between pseudopotential and full-electron potential beyond r_c ensures the correction of the properties that determined only by the valence electrons. On the other hand, the complicated core-electrons are substituted by only one

potential function therefore the computation cost is highly reduced. Again, since the pseudopotential of each element is only determined by the atomic number of the element, it could also be determined in a self-consistent way.

2.3 Surface and interface energy calculations

According to Tasker's definition, ionic crystals can be classified into three types. Type 1 is neutral with equal numbers of anions and cations on each plane and type 2 is charged but there is no dipole moment perpendicular to the surface because of the symmetrical stacking sequence. Both the two surfaces should have modest surface energies and may be stable with only limited relaxations of the ions in the surface region. Type 3 surface is charged and has a dipole moment in the repeat unit perpendicular to the surface. The surface can only stabilized by substantial reconstruction. The three different types of surfaces are shown in Figure 2.1.

Type 1 and 2 are called non-polar surface and type 3 is called polar surface. For the first two types of surfaces, the calculation of surface energy is pretty straightforward, while for the third type, the energy would diverge and the surface energy is becoming infinite as the electrostatic interactions between unit cells are pretty large. As a result, if we want to get accurate results for the third type surfaces, surface modifications are needed. However, one thing to point out is that this surface may exist in nanostructures. Possible methods of the modifications are adsorption or desorption, reconstruction accompanied by surface vacancy creation.

The standard for calculating the surface is to evaluate the total energy of a slab of the material of interest and to subtract from that the bulk energy obtained from a separate calculation. It is based on the general and intuitively appealing expression:

$$\sigma = \lim_{n\to\infty} \frac{1}{2}(E_{slab}^{N} - NE_{bulk})$$

where E_{slab}^{N} is the total energy of the slab and $E_{bulk}$is the bulk total energy, ½ term accounts for the two surfaces of the slab.

The reason for this equation is as follows. As plotted in Figure 2.2, Regions 1 and 3 are set wide enough so that the influence of the surface is negligible in region 2. In other words, the influence of the surface should vanish exponentially by increasing the widths of regions 1 and 3 when looking at orbitals at the surface and Wannier functions. This viewpoint suggests that with thick enough "surface regions" (regions 1 and 3) the "surface energy" should be defined regardless of the thickness of the region at the center (region 2) because the surface orbitals have negligible effect in region 2. The term "surface energy" will be used in this sense (surface energy in the infinitely thick slab limit) onwards.

Handling interface between two materials is similar to handling the surface of one material with vacuum. However, there are still many unsolved problem in this study.

The most straightforward methodology derived from the one surface calculation is that the interface energy can be extracted from the slab total energy minus the bulk energy of both materials. Complications arise on this point. First, for the interface buildup, two materials usually have different lattice parameters, while in nature, the interface is always perfectly formed, no strain. What is the most appropriate lattice parameter to use?

Secondly, the interface may be vague between two materials, what is the most appropriate bulk energy to use?

If we choose A's lattice parameter, B would be strained, and vice versa. If we choose the lattice parameter between A's and B's, both materials would be strained, and the effect is unknown comparing to one strained, one not. One other thing is that the strain contribution from the two materials is not known. This remains a big problem in the interface calculations.

Figures:

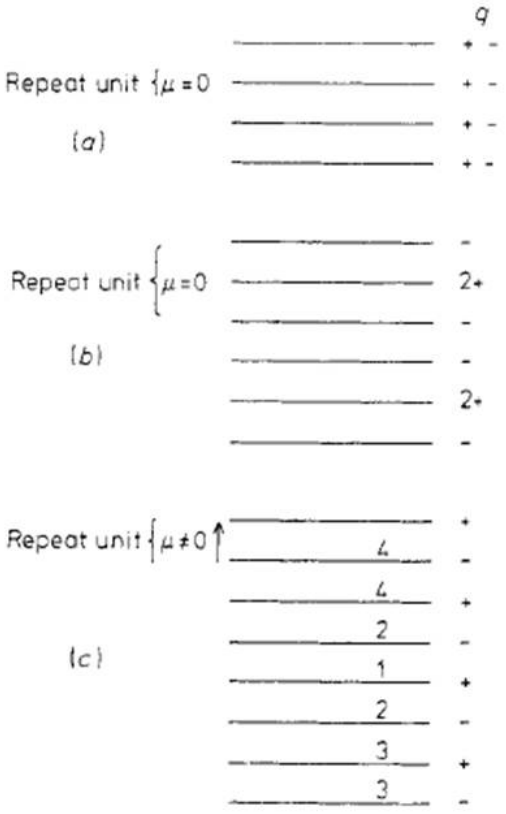

Figure 2.1: Three types of Tasker ionic crystal surfaces

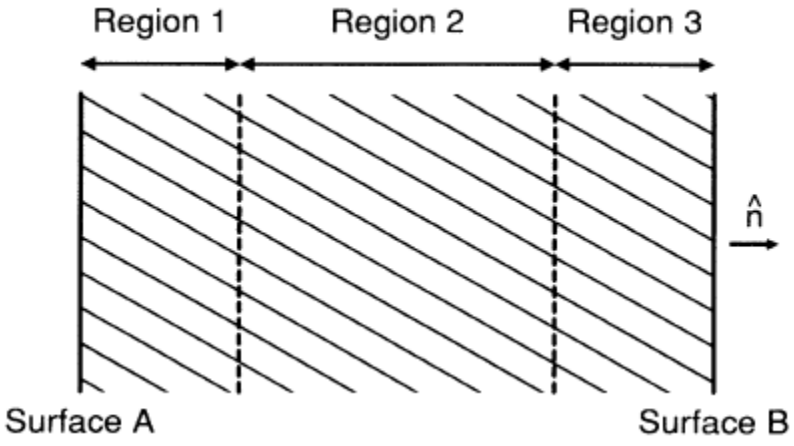

Figure 2.2: Schematic plot of surface and bulk

3. Advanced Analytical Electron Microscopy for Alkali-Ion Batteries

3.1 Introduction

In order to realize the commercialization of alkali-ion batteries (AIB) in electric vehicles and smart grid systems, further improvements are demanded in multiple aspects, especially the energy/power density, safety and cycle life. The performance of the batteries depend on the storage and diffusion of alkali-metal ions, electron transportation, structure and chemistry dynamics of the electrode/electrolyte materials, etc.. During electrochemical cycling, changes in structures and chemical distributions occur, including ion relocation, lattice expansion/contraction, phase transition, and structure/surface reconstruction, etc. These variations could impose significant influence on ion/electron transportations, and thus the performance and lifetime of the whole system. Understanding the structure-properties relationship of each component and their nanoscale evolution in the electrochemical process is essential for the design of new materials and optimization of existing systems.

The characterization of structure and electronic properties of each component is essential to understand and optimize battery materials. Multiple techniques have been developed both in-situ and ex-situ for structural and chemical characterizations, such as X-ray Diffraction, X-ray Absorption Spectroscopy, Neutron Diffraction, Nuclear Magnetic Resonance, etc.. However, only spatially averaged or surface-dominated information can be obtained from these techniques. On the other hand, structural and chemical evolutions upon electrochemical cycling often behave significantly different at nanofeatures, such as structural defects, boundaries, surfaces and interfaces, from that in

material bulk. Their influences on the functionalities of macroscopic devices are further magnified by the continuous device minimizations. Transmission electron microscopy (TEM), especially with the recently developed techniques such as aberration correctors and fast imaging cameras, has become one of the best techniques to probe these parameters at micron to atomic scale, under both static and in-situ electrochemical operations.

In this review article, firstly we will introduce the recent developments on TEM techniques that have been involved in or will be potentially valuable for the research of alkali-ion batteries. Then we will focus on the implementations of TEM in battery research by providing representative examples on how advanced microscopy significantly promotes our fundamental understanding of battery system and battery materials. Both advanced high-resolution electron microscopy and newly developed dynamic / in-situ TEM techniques for battery research will be reviewed. Last but not the least, perspectives regarding the future directions will be provided.

3.2 New progress on TEM

Over the past two decades, a number of significant improvements in TEM have provided substantial opportunities for fundamental new understanding of the working mechanisms in battery materials and systems, especially through the direct observations of atomic position and chemical bonds, as well as ion electron distributions at the atomic scale, Figure 3.1.[1-4] Aberration correction in TEMs has made it feasible to image and identify individual atoms. Single atomic columns can be routinely imaged.[5-8] In particular, taking advantage of the various scattering processes that occur between the incoming

electrons and atoms in materials, analytical imaging techniques with various sensitivities can be simultaneously applied using multiple annular detectors in scanning transmission electron microscopy (STEM). A high angle annular dark field (HAADF) image provides an image contrast proportional to atomic number ($\sim Z^{1.7}$); while a smaller annular angle detector (Annular bright field ABF) gives a contrast of $\sim Z^{-1/3}$ that is ideal for the detection of light elements, such as lithium.[9,10] A bright-field detector in STEM, which collects the elastically scattered electrons, provides phase contrast images equivalent to standard bright-field TEM images.[11] Low-angle annular dark-field imaging (LAADF), on the other hand, forms images by collecting both elastically and inelastically scattered electrons, providing opportunities for mapping strain fields in materials at atomic resolution.[12] Electron energy-loss spectroscopy allows probing electronic structures while collecting elastically scattered electrons only, and provides a complementary imaging mode with the unprecedented benefits of quantitatively probing both the chemistry and structure of nanofeatures at sub-A resolution.[6,13] With the recent development of monochromators for the electron gun, the energy resolution of EELS can now achieve 10meV, enabling not only the detections of electronic structure and atomic bonds, but also the investigations of vibration features in solid materials. [1,14]

Alongside with these developments of ultra-high spatial and energy resolutions, remarkable advances have been made in developing new *in situ* techniques and platforms for TEMs. These techniques have enabled direct observations of dynamic structural and chemical evolution in materials under a variety of external stimuli or near-real operation conditions. The progress is evident and has been demonstrated especially in the advances of *in situ* mechanical testing or heating while maintaining a high spatial resolution,[15,16] in

the studies of imaging reaction processes in gases and liquids,[17-20] and in the observations of reactions or phase transformations upon external biasing [21,22], etc. Along with the progress of *in situ* capabilities, the newly developed CMOS camera enables fast image acquisition of over 400 frame-per-second (FPS) for 1Kx1K images, and is significantly advancing real time observations of fast reactions. [23] These modern noteworthy advances in electron microscopy have opened broad opportunities for unraveling the mysteries in various materials and devices, and pinpointing the development and design of novel materials at the atomic scale.

3.3 HIGH RESOLUTION ELECTRON MICROSCOPY FOR BATTERY MATERIALS

Owing to the significantly enhanced spatial and energy resolutions, the state-of-art electron microscopy, including both atomic scale imaging and chemical analysis, has been applied extensively for probing the structural and chemical information of electrode and electrolyte materials as well as their interfaces in battery systems. These investigations have provided unique quantitative structure and chemical information benefiting both materials design and performance improvements in battery research.

3.3.1 Electrodes

Generally speaking, the electrode material can be divided into three types: intercalation, conversion and alloying materials. Intercalation based materials, which are the most commonly used in everyday batteries, are mainly transition metal oxides. The host structure does not change during the insertion and extraction of alkali-metal ions.

Conversion materials are mostly transition metal oxides and fluorides. The host structure would change upon cycling, and usually nanosized transition metal particles and lithium oxides would form after charging. For alloying type materials, the host and alkali metal would form alloy upon cycling, accompanied by volume change. TEM has played a crucial part in advancing the understanding of all three types of electrode materials. Two main aspects have been focused on using static TEM: structure identification and mechanistic study on the performance degradation mechanism. This part of the review will focus on how TEM helps and advances the development of representative compounds in the three categories.

3.3.1.1 Intercalation materials

The intercalation materials are of great interest in the history of cathode material development. Li-excess layered compounds, high voltage spinel, and olivine are the ones receiving the most attention due to their potential application in high-energy high-power electric vehicle. Even though the host structure remains the same during electrochemical process, Li concentration changes are always accompanied by diverse structural changes, such as lattice parameter variation, phase transition, surface reconstruction, etc. Electron microscopy provides a unique perspective on those processes down to the atomic level.

The family of Li-excess layered materials, $xLi_2MnO_3 \cdot (1-x)LiMO_2$ (M=Mn, Ni, Co, Fe, Cr, etc.), despite their good performances and the increasing attention they received, present many challenges for understanding the pristine-state structure and reaction mechanism that deteriorate the performances. Regarding the structure, there is a long-standing debate on whether it is a solid solution or two separate phases composing of R-

3m and C2/m. X-ray and neutron diffraction cannot give the exact information due to the overlap in peaks as well as the domain structure associated. This difficulty can be overcome by electron microscopy. Jarvis et al. discovered a solid solution in their Li-excess layered material[24] and identified planar defects formed from disordered R-3m to C2/m state.[25] Bareno et al. found a locally Li_2MnO_3-like region in the parent rhombohedral structure.[26] Boulineau observed the coexistence of two phases with the nominal composition.[27] Because of the atomic configurations unraveled by the STEM/EELS studies, it has now been agreed that the transition metal species, stoichiometry, synthesis methods, and calcination temperatures are important factors determining the structures.

The first-cycle irreversible capacity and the voltage degradation upon cycling are the main obstacles to the final commercialization. Therefore, understanding the reaction mechanism especially the first cycle is critical. Different proposals have been made including the activation of oxygen, the surface phase transformation to spinel-like/rocksalt structure, surface TM densification, etc.. Meng group carried out a series of systematic studies starting from electron microscopy.[28-31] A surface layer of defect spinel has been visualized for the first time and also been confirmed by many following studies.[27,32] The presence of the transition metal (TM) ions in the lithium layer has been evidenced by Z-contrast imaging, and the formation of defect spinel phase has been confirmed by EELS and first principles computation. By identifying the structural and chemical changes at different states of charge, a mechanism involving both bulk and surface is proposed. In addition, a novel oxygen-vacancy-assisted TM migration mechanism has been proposed to the surface phase transformation. (Summarized in

Figure 3.2) Later, Boulineau et al. proposed a densification model based on the observation of Ni/Mn segregation on the surface by STEM/EELS.[32] Researchers from PNNL also carried out several studies on this family of material and revealed the influence of nonuniform TM distribution and nanophase separation on the electrochemical performance. [33]

Li-excess family is a representative case of what electron microscopy can do in advancing scientists' understandings in battery materials. Clearly, many main pieces to solve the structure and mechanism puzzle can only be obtained by electron microscopy, such as the surface phase transformation, the chemical information along the interface, etc. By combining with other techniques, the mechanism is vividly presented.

Another good example is the investigation of atomic defects in olivine $LiFePO_4$. $LiFePO_4$ has attracted the most interest among all polyanion materials in battery research, owing to its low cost, non-toxicity, excellent thermal stability and environment friendliness. However, its intrinsic atomic structural defects, originating from the site exchange between Li and Fe (denoted as Fe_{Li}), also called as "anti-site defects", are the main structural characteristic limiting the electrochemical performance. Due to the one-dimensional Li^+ transport in LFP, such defects could significantly degrade the performance from two aspects: blocking the ion transportation and restraining the amount of available Li. Detecting the concentration and distribution of Fe_{Li} in this material thus is crucial to the performance improvement. Due to the small atomic number of Li, neutron diffraction was able to quantify the defects. The exact distribution of defects, however, remained unknown until the application of ADF imaging in electron microscope. Chung et al. discovered a locally aggregation behavior of Fe_{Li} through imaging and image

simulations.[34,35] Later on, a vacancy driven mechanism for such local segregation was proposed based electron microscopy results, depicted in Figure 3.3(a).[36]

In addition to defects quantification, the direct identification of reaction mechanisms in LPF during electrochemical process is another significant contribution of advanced electron microscopy to LFP research. It has been macroscopically identified that two-phase, i.e $LiFePO_4$-$FePO_4$ are involved in during cycling, and such reaction however was supposedly limiting the reaction dynamics. To the opposite, it shows an unexpected excellent rate capability for long-term cycling. Attention was thus attracted to the cycling mechanism at the phase boundaries. Thanks to TEM, it was possible to directly probe the phase boundary at the atomic level. Multiple novel microscopy techniques were combined to investigate such phase boundaries, including HRTEM, electron diffraction, EELS, and precession electron diffraction etc.. [37-40] Several working mechanism at $LiFePO_4$-$FePO_4$ phase boundaries, including core-shell,[38] spinodal[39] and domino cascade[40] were proposed based on microscopy results, consistent with the development of models from other techniques. Though no consensus has been achieved at current stage, these studies have provided invaluable information towards the understanding of working mechanism in 1-D diffusion battery materials.

These recent microscopy studies on intercalation materials discussed above well demonstrated the power of novel electron microscopy of its atomic-scale detectability of structure, chemistry, as well as bonding information for battery research.

3.3.1.2 Conversion and Alloying materials

Conversion materials, designed to utilize all possible oxidation states of transition metal, suffer from poor cycling retention and large hysteresis. Due to the formation of nano-sized particles after cycling, HAADF-STEM can be used to visualize the phase conversion due to the large difference between the contrast from metallic particles and that from lithium oxides/fluorides. Besides the image contrast, the elemental mapping can also provide the phase information at atomic resolution. Fluorides and oxyfluorides are attracting the attention due to their potential to serve as cathode materials with capacities up to 600mAh/g. Iron fluorides exhibit a superior cycling performance compared with other metal fluorides, for example, the reversibility of FeF_2 is much higher compared with CuF_2 while the reason was unclear. Owing to the ability of simultaneous morphology probing and elemental identification at high-spatial resolution in STEM, Wang et. al. discovered a conductive iron network formed for FeF_2 after cycling while discrete particles in the CuF_2 case by combining HAADF imaging and EELS analysis, shown in Figure 3.3 (c) & (d). This work reveals that the low electron conductivity is the source of poor reversibility in CuF_2.[41] Besides, several other research groups have used similar microscopy techniques and identified the conversion mechanisms of iron fluorides and iron oxyfluorides. [42,43]

The most representative alloying materials for battery electrodes is Si-based. These materials are considered as a strong candidate as negative electrodes, owing to an exceptional capacity of ~4200 mAh/g, compared to the 372mAh/g of the commercially used graphite. The practical use of silicon is, however, hindered by a massive 280% volume expansion during the charge–discharge process. Such a drastic change leads to loss of electric connections in the electrode.[44] It is therefore of special importance to

understand the exact chemical reactions and possible crystalline-to-amorphous transitions happening during cycling. Microscopy is an ideal tool for such studies as it provides high sensitivity not only to crystalline phases, but also amorphous ones. Using EELS, imaging and diffraction techniques, not only the final reaction products but intermediate phases of LixSi have been identified, providing valuable insights into structural and morphology optimizations of Si-based material for battery applications. [45,46] In addition, direct observations of the volume change and phase transformations in Si-based materials have been demonstrated because of the new developments of in-situ TEM techniques, which will be discussed latter in this article.

These studies demonstrated high resolution AEM provides unique insights into the atomic scale structural/chemical origin of the macroscopic behaviors during cycling. Although having limitations under certain circumstances, the TEM observation has played a vital role in understanding the electrochemical process of multiple extensively studied electrode materials.

3.3.2 Electrolyte

Due to the safety concerns associated with the flammability and leakage of conventional liquid electrolyte, the stable solid electrolytes have received tremendous attention.[47] However, the study of solid electrolytes using TEM is challenging: because of the vanishingly small electronic conductivity, the radiation damage is much more severe than that for the cathode materials.[41,48,49] As a result, the atomic-resolution TEM studies on solid electrolytes are rare.[46,49-56] Regardless, most of these papers provided unique insights into the ionic conduction behaviors, and laid important groundwork for the

design and discovery of high-performance solid electrolytes. The primary bottleneck for the application of solid electrolytes is the low conductivity. A rational improvement strategy cannot form without a proper understanding on the Li^+ transport behaviors. The perception of this phenomenon consists of three aspects: the Li^+ transport 1) within the lattice, 2) along/across the grain boundaries, and 3) across the electrode/electrolyte interfaces. While the study of the first one frequently benefits from quite a lot of characterization techniques, the other two, in many cases, can only be straightforwardly studied by TEM.

The Li^+ conduction behavior within the lattice is dictated by the Li^+ percolation pathways. As such, the crystal structure and Li distribution are consistently the focal point in literature. The high spatial resolution and sensitivity to minor structure differences make TEM particularly suitable for such a task. Using precession electron diffraction, which has the advantage of minimizing the distraction from double diffractions, Buschmann *et. al.* successfully distinguished between the tetragonal and cubic phases of the garnet $Li_7La_3Zr_2O_{12}$.[49] The disordered Li distribution in the cubic polymorph with respect to the tetragonal one is essential in explaining the high ionic conductivity of the former. In the same paper, efforts have also been made to study the atomic structure via HRTEM, but only limited information was acquired due to the quick amorphization of the material under electron beam. Recently, this difficulty was overcome by Ma *et. al.*.[56] By weakening the electron beam current and using a cryogenic stage, the atomic structure of HAADF-STEM was finally visualized. In addition to the crystal structure, TEM is also very effective in probing the local Li distribution. Gao *et. al.* has took full advantage of the imaging capability of ABF and precisely determined the

Li position in $(Li_{3x}La_{2/3-x})TiO_3$,[46] a system showing the highest bulk conductivity among all the oxide solid electrolytes, shown in Figure 3.4 (a-b).[47] Furthermore, the Li content, valence state of Ti, and geometry variation of oxygen octahedra in the alternating La-rich and La-poor layers were revealed via the associated EELS analysis.[47] The Li migration pathway was delineated based on these observations. Beyond this, the same authors reported the local structure/chemistry variation across the boundaries between the La-rich/poor ordering domain, and concluded that the domain boundaries serve as obstacles for the Li transport.[51] The precise analysis of such local features brings invaluable insights in interpreting the ionic conduction mechanism.

Although most studies on solid electrolytes focus on the Li migration within the lattice, the grain boundaries are no less important. The bulk conductivity of many solid electrolytes is actually sufficiently high for application.[47] It is their large grain-boundary resistance that lowers the total conductivity by orders of magnitude.[47] Unfortunately, due to the ignorance of the grain-boundary conduction mechanism, no effective improvement strategy has formed. Since the grain boundaries are typically as thin as several unit cells, the ultrahigh spatial resolution in TEM is an ideal tool to study them. Recently Ma *et. al.* has made the first attempt of scrutinizing the structure and chemistry of grain boundaries in $(Li_{3x}La_{2/3-x})TiO_3$, a typical example of a Li^+ superionic conductor being plagued by the poor grain-boundary conductivity, details in Figure 3.4 (c-e).[55] A local structural fluctuation was found to prohibit the abundance of Li, and thus hinders the ionic transport. The capability of TEM in resolving such issues is clearly demonstrated. Nevertheless, currently not much effort has been devoted towards this direction, and the grain-boundary conduction mechanism for many important systems remains unknown.

Finally, TEM is also very effective in studying the interfaces. Similar to the solid-electrolyte-interphase (SEI) layer in conventional Li-ion batteries with organic liquid electrolyte, interface layers were frequently observed between the intercalation cathodes and solid electrolytes.[52-54] A fundamental understanding of the structure and chemistry of the interfaces is indispensable in optimizing the battery performances. Based on the combined imaging and EDX analyses, the interface in most systems was found to form via the mutual diffusion between the cathode and solid electrolyte.[52-54] Unlike the SEI layers in the conventional Li-ion batteries, such interfaces are more detrimental than beneficial; their existence typically introduces a large interfacial resistance and degrades the battery performance.[52-54]

In summary, TEM is a very effective tool in studying the ionic transport mechanism of solid electrolytes. Its high spatial resolution offers unique convenience in studying localized features such as grain boundaries and interfaces. However, since the electron radiation damage is especially difficult to control for the solid electrolyte, currently the atomic-resolution STEM/EELS studies can only be performed in a very limited number of systems. Clearly, the implementation of such a powerful tool in the study of solid electrolytes demands a comprehensive investigation of the radiation damage mechanism that can guide the optimization of electron beam condition for each specific system.

3.4 DYNAMIC/IN-SITU MICROSCOPY FOR BATTERY RESEARCH

Due to the dynamic nature of the electrochemical process, it is important to reveal the real-time structural/chemical variations in battery materials to completely understand

the working or degradation mechanisms involved in, which however, is often beyond the ability of ex-situ characterizations. As a result, many in-situ techniques based on either spectroscopy or imaging, e.g. X-ray diffraction, Raman spectroscopy, Nuclear Magnetic Resonance, Scanning Electron Microscopy, etc., have been developed for this purpose. Among the different in-situ techniques, in-situ TEM, which possesses the unique capability of directly visualizing the materials behavior in real time with a high spatial resolution, naturally received intensive attention. However, in-situ electrochemical cycling in the high vacuum chamber of TEMs is challenging, mainly because (1) a limited size of a electrochemical cell can be investigated because of narrow pole-piece gap in microscope and the pre-request of sample thickness -- beam transparent; and (2) the cell design has to be high-vacuum friendly. The first limitation arises challenges to specimen preparation, material selection and biasing control etc., and the second one challenges the use of organic electrolytes which is the most common one being used in battery labs. In the following sections, we will discuss the details of the leading three in-situ microscopy configurations in battery research.

3.4.1 Open-cell configuration

In an open-cell configuration, as shown in Figure 3.5(a), the electrolyte is either solid Li_2O or an ionic liquid, which makes point contacts with the electrode. The low vapor pressure of ionic liquid makes it possible to be directly loaded and observed inside a TEM vacuum chamber. An overpotential is then applied and Li is driving from one electrode to the other. The lithiation process of several electrode materials is studied by this configuration. Intensive work from this type of set-up focuses on the alloying type

anode because the large volume change can be readily detectable using such simplified configuration. Liu and his colleagues reported for the first time the direct observation of anisotropic swelling of Si nanowires during lithiation.[57] Their following studies further revealed electrochemical process on nanostructured Si with different sizes.[58] Later on, the observation of such lithiation process at atomic-scale was achieved, enabling the discovery of a layer-by-layer peeling mechanism of the lithiation process on Si {111} facets. [59] Such mechanisms seamlessly explain the orientation-dependent Li mobility in Si. Using the same configuration, several other in-situ studies have been reported on multiple types of materials. Wang et. al. studied the lithiation mechanism of amorphous SnO_2 nanowires and observed a simultaneous partitioning and coarsening characteristics of LixSn through Sn and Li diffusion.[60] Zhu et al. imaged the FP/LFP phase boundary movement during electrochemical cycling for the first time. [61] In addition, the conversion reaction for FeF_2 was observed to start at the surface and propagates into the bulk similar to a spinodal decomposition by using the same half-cell point-contact configuration.[62] As such half-cell configuration uses Li metal as counter electrode and limits material choices in experiments, full-cell set-ups have also been tried. Huang applied $LiCoO_2$ as counter electrode to SnO_2 and observed a reaction front propagating in SnO_2 nanowire, depicted in Figure 3.5(b). [63]

In-situ open cell set-up in TEMs has provided invaluable nano-scale information for fundamental understandings of reaction mechanism in various electrode materials. However, its intrinsic simplified configuration not only limits the selection of materials, especially the selection of electrolytes, but also the potential of recording corresponding electrochemistry data. Furthermore, controlled reversibility, i.e. precise lithiation and

delitiation, based on such configuration is also tricky. Other in-situ configurations thus have been developed accordingly.

3.4.2 Liquid-cell configuration

The aforementioned limitations of the open-cell setup stimulated the development of other configurations that can better mimic the actual batteries. One promising strategy is the liquid-cell configuration, where a fully functioning miniature battery is sealed with silicon nitride membranes to avoid the evaporation of the liquid electrolyte. In contrast to the open-cell setup, the liquid-cell configuration not only allows for the integration of the commonly used electrolyte, but also preserves the way that the electrode is in contact with the electrolyte as in real batteries. With such advantages, valuable insights that are difficult to obtain in the open-cell configuration were acquired. When Gu et al. applied the liquid-cell configuration for battery study (Figure 3.6(a)), they not only observed the lithiation/delithiation process of single Si nanowires that are consistent with the open-cell studies, but also successfully unraveled the dynamics of the electrolyte, which is difficult to probe using the open-cell setup. This result could entail a new and effective quantitative characterization for the formation of the solid-electrolyte interphase (SEI) layer.[64] Following this pioneering work, Zeng et al. observed Li metal dendritic growth as well as the SEI layer formation (Figure 3.6(b-c)).[23] In addition, Holtz et al. also used a similar configuration to determine the lithiation state of $LiFePO_4$ in real time with a relatively high spatial resolution.[65]

Despite these valuable discoveries, the liquid-cell configuration has limitations. One of its most important drawbacks is the low spatial resolution. The presence of silicon

nitride membranes and the liquid electrolyte reduces the electron transparency of the miniature battery and undermines the spatial resolution. As a result, the liquid cell configuration is only suitable for probing the morphology change, *e.g.* Li dendrite growth, but cannot straightforwardly study the detailed structure/chemistry evolution at the atomic scale. Unfortunately, the latter is frequently more essential in perceiving the electrode processes. Clearly, preserving the full functions in miniature batteries is not sufficient for a detailed *in-situ* TEM study; minimizing/eliminating the additional thickness and maintaining the high spatial resolution are of no less importance.

3.4.3 All-solid-state micro-battery

The all-solid-state micro-battery approach can well circumvent the shortcomings of the liquid cell without sacrificing the integrity of the batteries. In this configuration, the Focused Ion Beam (FIB) is used to fabricate a cross-sectional lamella out of an all-solid-state thin film battery, as shown in Figure 3.6 (d). Such a lamella not only preserves the full functions of the thin-film battery, but also thin enough ($\leq$ 100 nm) for electron transparency. Without the interference from the silicon nitride membranes and organic electrolytes in the liquid cell configuration, the all-solid-state micro-battery approach can provide much more detailed structural and chemical information in a much higher spatial resolution. In 2010, Yamamoto *et. al.* successfully applied this configuration to visualize the electric potential variation during the charge/discharge processes for the first time.[66] Using a piece of 90 μm thick NASICON-type glass ceramic (Ohara Inc.) as the electrolyte and 800nm thick $LiCoO_2$ as the cathode, the pristine-state battery is configured as Au/$LiCoO_2$/solid-electrolyte/Pt. During the first charge, a certain thickness

of the solid electrolyte near Pt was reduced, serving as the anode in the following discharge. With such setup, the 2D potential distribution resulting from movement of Li^+ near the $LiCoO_2$/solid electrolyte interface was clearly visualized. Such a success stimulated an intensive interest in further perfecting the all-solid-state micro-battery approach for more in-depth analysis.

Despite its apparent advantages, presently this technique is much less developed than the other two discussed above; many problems remain to be addressed. First of all, the small thickness of the micro batteries (usually 100 nm or less) poses a formidable challenge. The successful cycling of a Li-ion battery usually demands a current density no larger than a few or tens of mA/cm^2 (otherwise the battery will fail catastrophically).[67] Because of the small dimension of the lamella for TEM observation, an extremely weak current of a few pA is required to meet this requirement. Realizing such a high current resolution is challenging for most *in-situ* TEM holders. Secondly, the stability of solid electrolytes also brings complications. Although not volatile like the liquid organic electrolytes, quite a few solid electrolytes are air- or moisture-sensitive. For example, the most important thin-film electrolyte, LiPON, can easily decompose by reacting with the moisture in air, and almost all sulfide solid electrolytes, despite their high conductivity, suffers severely from hydrolysis issues.[47] Therefore, appropriate air protection is needed for specimen transfer and storage. Thirdly, the re-deposition during the FIB fabrication of the micro-batteries could easily cover both the cathode and anode, shorting the entire battery stack. Last but not least, many solid electrolytes are subject to damage under intense electron beam in the (S)TEM. The imaging condition needs to be cautiously controlled to preserve the battery integrity during observation. Because of these

challenges (and possibly many other unknown difficulties), the full charge/discharge cycle has never been reported again after Yamamoto's *in-situ* electron holography study in 2010. Only several relatively successful attempts have been made. For example, Meng *et. al.* have tried to perform *in-situ* TEM studies on $Au/SnO_2/Li_{3.4}V_{0.6}Si_{0.4}O_4/LiCoO_2/Pt$ [67] and $Au/LiCoO_2/LiPON/Si/Cu$ [68] batteries. Although neither of them realized a full charge/discharge cycle, the element distribution across the interfaces was successfully visualized (Figure 3.6 (e,f)), and valuable experiences of fabricating a functioning micro-battery lamella were obtained. Clearly, the all-solid-state micro-battery configuration is still in its infancy stage compared to the open cell and liquid cell. However, it holds the greatest promise in unraveling atomic-scale structure/chemistry evolution during battery operation, and is thus attracting increasingly intense interest.

3.5. CONCLUSIONS AND PERSPECTIVES

In this review, we focus on the importance and recent progresses of (S)TEM study in alkali-ion batteries. With the remarkable development of the instruments, many of the previously formidable tasks, such as visualizing the distribution of light elements, unraveling the interface structure/chemistry at the atomic scale, and probing the SEI layers, *etc.*, have now become viable. Such capabilities greatly deepened the fundamental understanding of multiple important electrode and solid electrolyte materials. Beyond the static and *ex-situ* studies, various *in-situ* TEM techniques are also developed to study the dynamic electrochemical processes during charge/discharge. Among the three categories of the most extensively pursued *in-situ* TEM techniques, the all-solid-state micro-battery approach can well circumvent all the primary shortcomings of the open-cell and liquid-

cell configurations without compromising the battery integrity. These characteristics make it highly promising for realizing the atomic-scale observation of the real-time structure/chemistry evolution during battery operation, which is the key to comprehending and improving the battery performances. Therefore, although this technique is still in its infancy and poses many challenges, it is attracting increasingly intense research interests.

Chapter 3, in full, is a reprint of the material "Advanced analytical electron microscopy for alkali-ion batteries", as currently being submitted for publication in Asia Materials. The dissertation author was the primary investigator and author of this paper. Most of the writing was conducted by the author.

Figures:

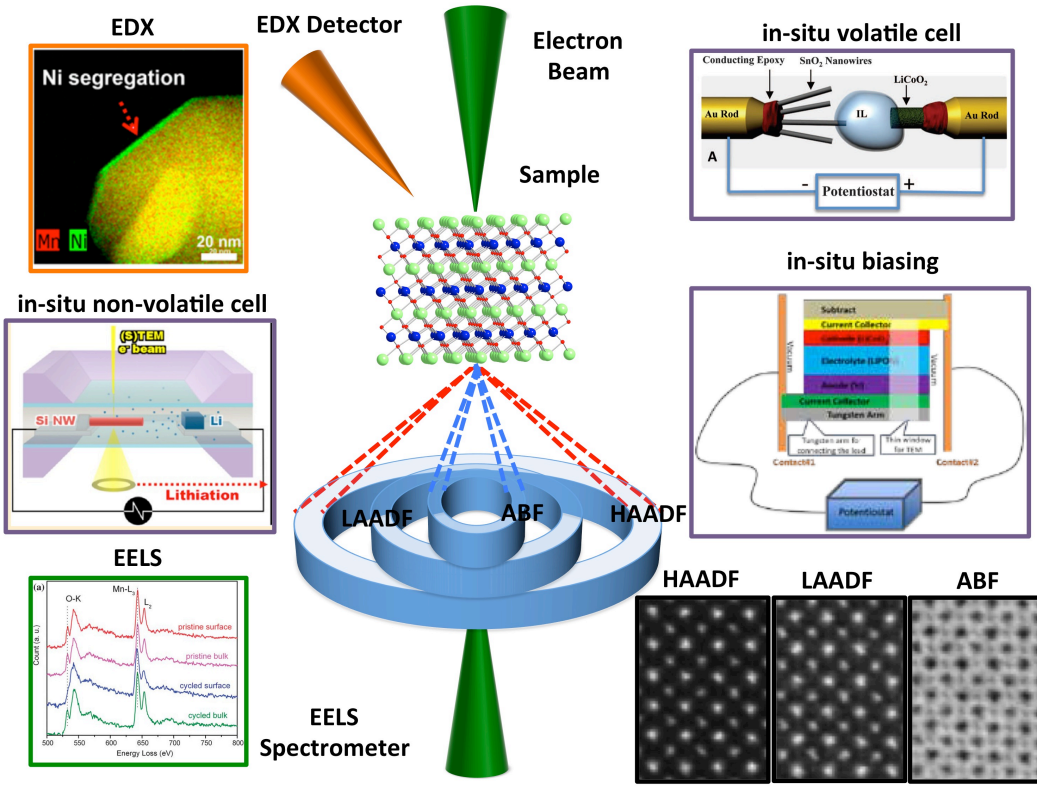

Figure 3.1: Overview of the implementation of TEM in AIB.

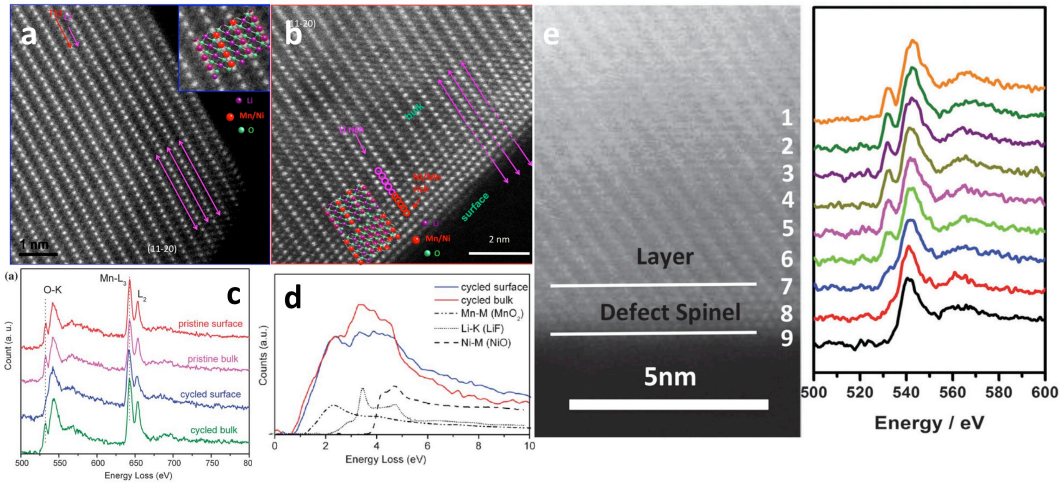

Figure 3.2: HAADF STEM images of Li-excess materials (a) pristine and (b) after cycling; (c) &(d) EELS comparison of pristine and cycled surface and bulk; (e) Spatial resolved O K-edge EELS from surface to bulk in cycled Li-excess.

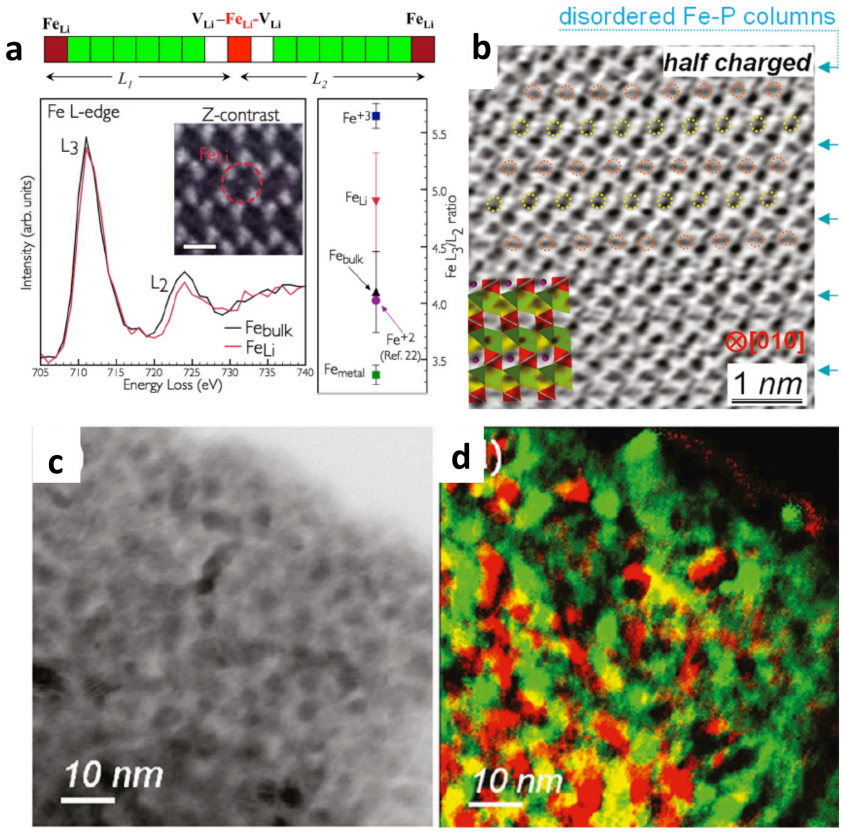

Figure 3.3: (a) Top: Schematic figure of the probable configuration of Fe_{Li} with a higher Fe oxidation state. Bottom: (Left) EELS data of Fe_{Li} and the Fe in bulk. (Right) Compared L3/L2 ratio with reference different iron compounds; (b) ABF image of half charged state showing the Li staging; (c) BFTEM and (d) false-color elemental map of charged FeF_2 with Fe (green) and LiF (red), showing a interconnected network.

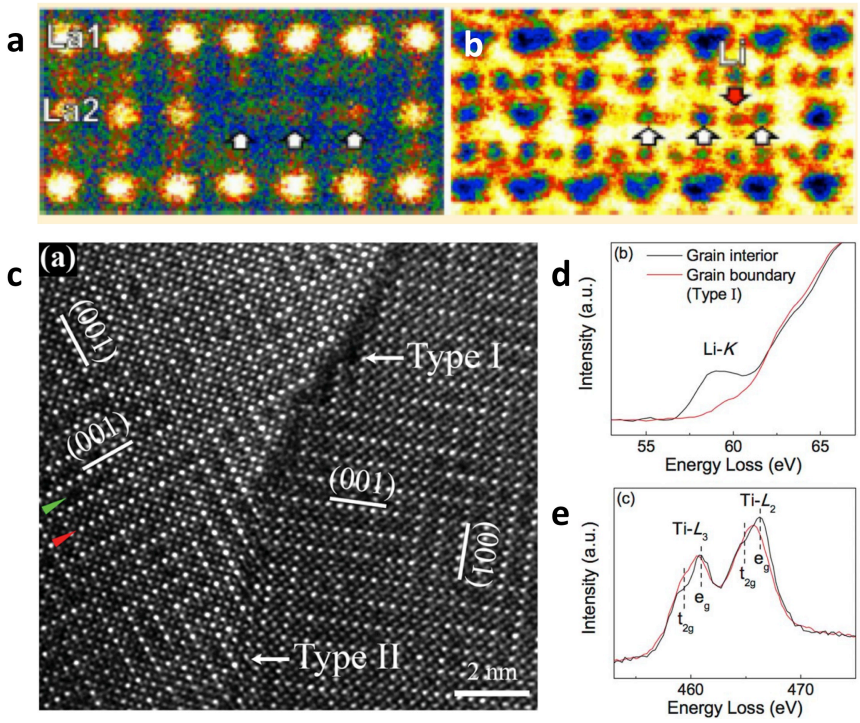

Figure 3.4: (a) HAADF and (b) ABF of local clustering of A-site vacancies and O4 square window lithium. (c) HAADF STEM images of a LLTO grain boundary. EELS data of (d) Li K edge, (e) Ti L edge for the grain boundary and the bulk.

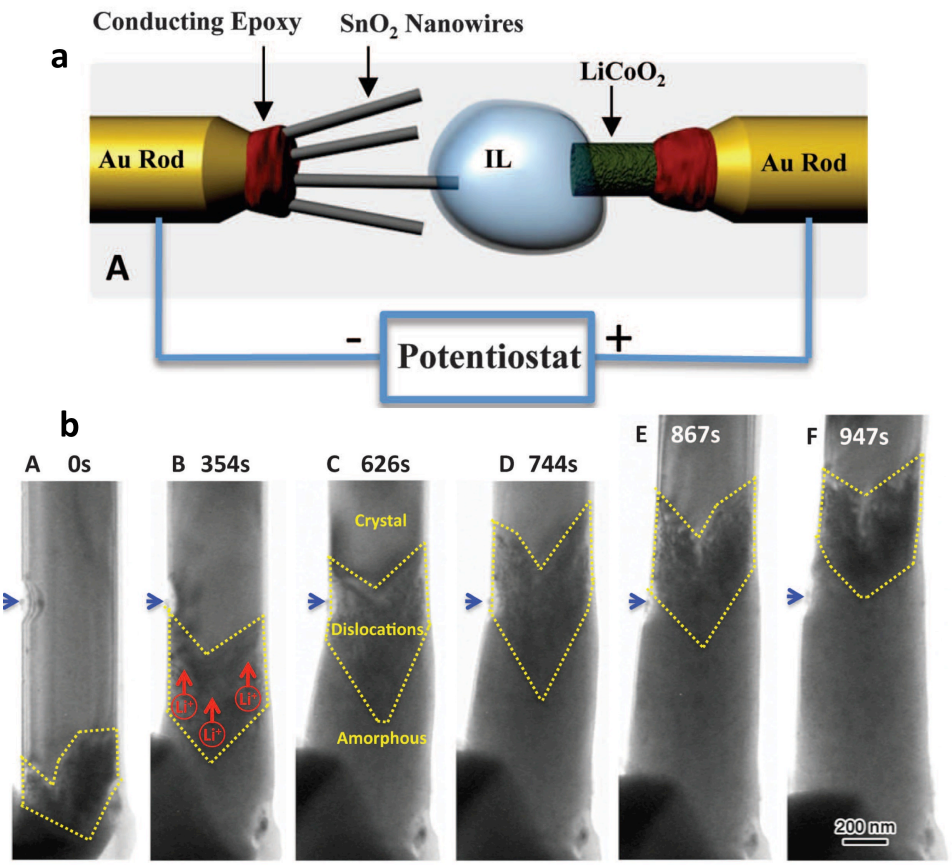

Figure 3.5: (a) Schematic of the volatile cell set up; (b) a high density of dislocations emerging from the reaction front was revealed in single SnO_2 nanowire.

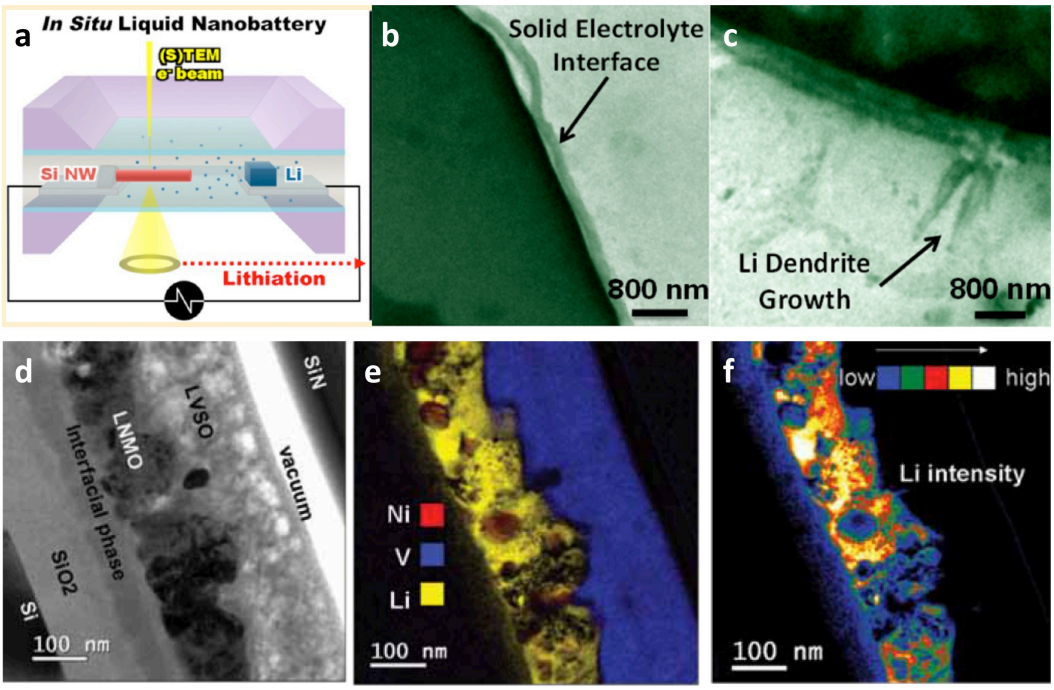

Figure 3.6: (a) Experimental set up of non-volatile cell set up with liquid electrolyte; (b) & (c) in-situ observation of inhomogeneous lithiation, lithium metal dentritic growth and solid-electrolyte interface formation; (d) an example of all-solid-state battery with the configuration of Au (current collector) / SnO_2 (anode) / $Li_{3.4}V_{0.6}Si_{0.4}O_4$ (electrolyte) / $LiNi_{0.5}Mn_{1.5}O_4$ (cathode) / Pt (current collector); (e) & (f) the EELS mapping of Ni, V, Li and Li intensity.

4 SURFACE SPIN TRANSITION IN NANO-SIZE STOICHIOMETRIC $LiCoO_2$ AND ITS APPLICATIONS IN OXYGEN EVOLUTION REACTION / OXYGEN REDUCTION REACTION (OER/ORR) CATALYTIC PROCESS

4.1 Electronic Spin Transition in Nano-size Stoichiometric Lithium Cobalt Oxide

4.1.1 Introduction

Lithium cobalt oxide ($LiCoO_2$) is a compound of great importance, as it has been the most widely used positive electrode material for lithium ion batteries for nearly two decades. $LiCoO_2$ adopts the α-$NaFeO_2$-type crystal structure with rhombohedral symmetry (space group R-3m) and Li^+ and Co^{3+} ions sitting in octahedral sites formed by alternating layers of oxygen. Because of such an ordered layered structure, Li^+ can be reversibly deintercalated and re-intercalated from $LiCoO_2$ to $Li_{0.5}CoO_2$ with a high electrochemical potential of up to 4.2V (vs Li^+/Li). In recent years, it has been demonstrated that ultra fast charge/discharge rate capabilities can be achieved in this compound when nano-scale (< 50nm) particles with morphology optimal for Li intercalation are prepared and tested.[69,70] Okubo et al.[69,71] observed several interesting phenomena associated with their nano-sized $LiCoO_2$: First, lattice parameter expansion is observed in particles less than 20nm; second, the magnetic susceptibility increases dramatically when compared with that of bulk-$LiCoO_2$. The authors hypothesized that these phenomena are mainly due to the presence of Co^{2+} on the surface of their nano-sized particles, Co^{2+} being present in the form of $Li_{1+x}Co^{2+}_xCo^{3+}_{1-x}O_2$, as a consequence of their hydrothermal synthetic process. However, the interpretation of the magnetic data is ambiguous since no direct evidence for the presence of Co^{2+} was obtained.[71] Moreover,

Levasseur et al.[72] pointed out that in bulk lithium over-stoichiometric ("Li-excess") samples, the charge is compensated by oxygen vacancies. This leads to some cobalt ions being in a square based pyramidal site with an intermediate spin (IS) configuration. In this communication we show that, for stoichiometric nano-sized $LiCoO_2$, the anomaly in magnetic susceptibility can similarly be explained by the presence of IS or HS Co^{3+}, a phenomenon which alters the lithium (de)intercalation voltage significantly.

4.1.2 Methodologies

4.1.2.1 Computational Methodology

The DFT + U calculations we adopt here treat core electrons by the projector augmented-wave method[73] as implemented in the Vienna ab initio simulation package (VASP).[74,75] The rotationally invariant approach of the on-site Hubbard U given by Liechtenstein et al.[76] is utilized at the Co sites. The U value, U_{eff} = U-J = 3eV, is chosen similar to a previous study.[77]

All calculations are performed with a plane wave cutoff of 420eV. The four-atom unit cell is used for the bulk calculations. The Brillouin zone is sampled with appropriate k-point mesh to ensure that the total energies are converged within 1meV per formula unit of $LiCoO_2$. For the surface calculation slabs, a similar dense k-point in reciprocal space only parallel to the surface is applied; the surface-plane lattice parameters of slabs are fixed to the bulk values, and only the atomic positions are allowed to relax; Both $LiCoO_2$ atomic layer thickness and vacuum thickness are set to be around 20Å, to avoid interactions between slabs.

4.1.2.2 Synthesis of stoichiometric $LiCoO_2$ nanoparticles.

Chen and Grey have shown previously that a molten salt can be used to synthesize highly stoichiometric $LiCoO_2$ nanostructures.[70] The particle size and morphology of $LiCoO_2$ can be controlled by the composition of the molten salts. Higher nitrate concentrations in the eutectic system results in a smaller $LiCoO_2$ particle size; while higher hydroxides concentration results in a larger particle size or in 3D nanostructures. In this work, the previously reported molten salt method was modified in order to synthesize stoichiometric $LiCoO_2$ with very fine and tunable particle sizes, e.g. from ~10 nanometers to a few tens of nanometers. Nano $Co(OH)_2$ was used as the cobalt source instead of cobalt nitrate. It was synthesized by a precipitation method: 1 M $Co(NO_3)_2.6(H_2O)$ solution was slowly added into a 0.1 M LiOH solution under 400 rpm magnetic stirring. LiOH was 5% excess to the stoichiometric amount. The brown precipitate ($Co(OH)_2$) was filtered and washed by distilled water and methanol several times and dried in a vacuum oven at 60^{o}C overnight. In a typical synthesis of stoichiometric nano-$LiCoO_2$, a 10-gram mixture containing lithium and potassium salts (various molar ratios were used depending on the desired size of $LiCoO_2$ (see Table 4.1)) was heated in a PTFE crucible at 200^{o}C (uniform heating was achieved by placing the crucible in an oil bath), to form a clear flux. Then 200 mg of the as-prepared $Co(OH)_2$ powder was then added into the mixture under magnetic stirring (600 rpm). The temperature of the flux was kept at 200^{o}C for a certain period of time depending on the desired particle size (see Table 4.1). The crucible was then taken out of the oil bath and quenched with distilled water. The solid product was separated from the salts by filtration,

washed with distilled water, and then dried at 90^{o}C overnight in a vacuum oven. The type and ratio of the Li and K salts in addition to the reaction times were varied to control the particle size of the $LiCoO_2$ products, as listed in Table 4.1. Crystallite size was estimated from the line broadening in the XRD patterns by using the Scherrer equation.[78] Fits were conducted on 9 peaks and averaged to give the calculated crystallite size.

4.1.2.3 XRD Instrumentation and Lattice Parameters

X-ray diffraction data was collected using a Rigaku Miniflex II Bragg-Brentano diffractometer, which features a high-power rotating anode X-ray generator operating at 13kW. The X-ray source is a Cr target. The goniometer is a 185mm radius horizontal-circle with a diffracted-beam graphite monochromator and scintillation detector. The data was collected at a step size of 0.02° every 10s.

4.1.2.4 XPS Instrumentation

Nano-sized $LiCoO_2$ samples were prepared by pressing each powder onto a strip of double-sided adhesive tape followed by mounting onto the sample holder for XPS analysis. Room temperature XPS was performed on a Thermo Scientific K-alpha microprobe with a focused monochromatic Al K_α X-ray (1486.6 eV) source. A hemispherical analyzer was equipped, with an incident X-ray beam 45° off normal to the sample while the X-ray photoelectron detector was normal to the sample, and the chamber pressure was kept at $< 10^{-10}$ Torr for all measurements. Charge compensation was employed during data collection (1 eV, 20 μA electrons) and binding energies of the photoelectron were corrected to the aliphatic hydrocarbon C 1s peak at 284.6 eV.

4.1.2.5 ^{7}Li NMR

^{7}Li NMR data were collected using 1.8 mm probe made by Dr, Ago Samoson. A spin echo pulse sequence was used (90°- t -180°- t -acq, where t is one spinning rotor period, acq is the acquisition time, and 90° and 180° radio frequency pulse durations are about 1.6 and 3.2 ms, respectively) to ensure the observation of the very broad signals which could be missing in a single pulse experiment due to the receiver dead time. The isotropic shifts of the broad peaks corresponding with negative hyperfine shifts were determined by comparing spectra collected at different spinning speeds. Quantification of the fraction of the peaks with negative hyperfine shifts was obtained by curve fitting the spectra.

4.1.2.6 Fitting Equation for the Curie Constant

$$C = p\frac{N_A}{3k_B}n(n+2)\mu_B{}^2 = 1.25\,pn(n+2)$$

Theoretical Curie constant

p = number of magnetic species per mole

n = the number of unpaired electrons in the magnetic species (n=2 for Co^{3+} mid spin)

N_A= Avogadro's number

k_B= Boltzmann constant

μ_b= Bohr magneton

4.1.3 Results and Discussions

The surface energies of $LiCoO_2$ were calculated from first principles with the Hubbard U correction on the generalized gradient approximation (GGA+U) to the density functional theory (DFT). The results are listed in Table 4.3. We find that the surface energies are minimized when the surface Co^{3+} ions are either in the intermediate (IS) or high spin (HS) state depending on the crystallographic orientation. This change in the electronic spin state on the surface can be rationalized by a change in the surface Co crystal field due to the missing Co-O bonds.

$LiCoO_2$ particles are typically dominated by the {001} surface, however this surface is not active for Li (de)intercalation. Therefore, we focus on studying the {104} and {110} surfaces, which are the two lowest energy non-polar surfaces identified by previous work.[79] Figure 4.1a shows the {104} surface of $LiCoO_2$, which represents a major, low energy surface for $LiCoO_2$; this surface slices through the Co, O and Li planes and is expected to be involved in the (de)intercalation process. This represents the {100} surface of the NaCl lattice from which the ordered rocksalt $LiCoO_2$ is derived. In the bulk, and on the {001} surface, octahedrally coordinated Co^{3+} ions are in the low spin (LS) state and do not have unpaired electrons. On the {104} surface, however, the Co^{3+} ions are coordinated by five oxygen ions, resulting in a square pyramidal configuration. The surface energy is then lowered significantly when going from the LS configuration ($1118mJ/m^2$) to the IS ($312mJ/m^2$). Figure 4.1b depicts the {110} surface of $LiCoO_2$. In this orientation, the Co^{3+} ions on the surface are coordinated by four oxygen ions with a pseudo-tetrahedral configuration. The surface energy is minimized from $2227mJ/m^2$ (LS) to $1241mJ/m^2$ (HS). The details of the crystal field splitting of *3d* orbitals and the corresponding energy levels of bulk and surface cobalt ions are shown in Figure 4.1c. A

square pyramidal crystal field breaks the degeneracy of both the t_{2g} and e_g orbitals observed for octahedral symmetry, since the missing O ion along the z-direction reduces the repulsion between *2p* electrons and *3d* electrons in orbitals pointing towards or closer to the z-axis. A pseudo-tetrahedral crystal field with two missing bonds in the *xy* plane leads to lower energies for the $3d_{xy}$ and $3d_{x2-y2}$ orbitals. A charge density plot, which represents the difference in up and down spins, of the {104} surface clearly show the unpaired electrons as compared to the case of Co^{3+} (LS) in the bulk of $LiCoO_2$. (See Figure 4.2a and 4.2b) The first principles calculations reveal that both the {104} and {110} surfaces with optimized Co coordination environments and electronic states expand normal to the surface, the displacement being on the order of 0.1-0.2Å. It is important to point out that such changes in electronic spin states are also seen in first principles simulations of surfaces of CoO and Co_2O_3, as well as $LiNiO_2$.

To validate the hypothesis that the Co^{3+} on the surface is in an intermediate spin state by experimental spectroscopic techniques, stoichiometric $LiCoO_2$ samples with extremely small particle sizes (thus very large surface areas) provide the best opportunities. However, it is difficult to make stoichiometric nanoparticles of $LiCoO_2$ by conventional solid state or hydrothermal methods.[80] Okubo et al. reported samples with small particle sizes (8 to 32 nm), but the samples are most likely over-stoichiometric, i.e., $Li_{1+x}CoO_2$.[69] By contrast, the molten salt method reported earlier[70] represents a much better approach to prepare stoichiometric $LiCoO_2$ nanoparticles. In this work, stoichiometric $LiCoO_2$ with very small particle sizes (10nm, 16nm, 20nm, 30nm and 40nm) were synthesized by using a modified molten salt method based on the previously reported method. We observed expansion of the lattice parameters from Rietveld analysis

of the XRD results, similar to that observed by Okubo et al.[69], along with magnetic susceptibility data that indicates the presence of unpaired electrons. X-ray diffraction (XRD) data indicates the formation of pure single-phase $LiCoO_2$ for the 20, 30 and 40 nm samples, all the peaks corresponding to the layered α-$NaFeO_2$ structure (Figure 4.3a). Lattice parameters are extracted and the c/a ratio is approximately 4.99, indicating a well-formed layered structure.[81] Detailed information regarding the lattice parameters is given in Table 4.2. The reflections in the XRD pattern for the 10nm particles are broad and a quantitative refinement could not be achieved.

X-ray photoelectron spectroscopy (XPS) was carried out with a Thermo-Scientific K-Alpha spectrometer using a focused monochromatic Al Kα anode source. As shown in Figure 4.3b, all compounds show a Co $2p_{3/2}$ main peak at 779.5eV with a satellite peak at 789.5eV and a Co $2p_{1/2}$ main peak at 794.5eV with a satellite peak at 804.5eV. This observation confirms that the oxidation state is Co^{3+}. This is strong evidence that our nano-sized LiCoO2 samples are stoichiometric. Co^{2+} coordinated by oxygen is characterized by a strong broadening of the main line and a very intense satellite peak at 785.5 eV (Co $2p_{3/2}$) and 802.5 eV (Co $2p_{1/2}$),[80,82] which are both absent in the spectra.

^{7}Li magic-angle-spinning (MAS) NMR spectroscopy was performed at a magnetic field strength of 4.7 T with a spinning speed of 35 kHz to explore the Li nonstoichiometry in nano-sized $LiCoO_2$. Figure 4.4a shows that the spectra of the 10 to 30 nm particles are dominated by a single resonance at 0 ppm, as expected for a stoichiometric, diamagnetic $LiCoO_2$ sample.[72] The larger NMR linewidth observed for the 10 nm sample compared to the others may be due to the presence of a trace amount (<1%) of Co_3O_4 impurity, which

results in faster transverse relaxation leading to larger line width. A weak, hyperfine shifted resonance is observed at +185 ppm for the 30 nm sample. This shift, along with peaks at 3, -6 -16, -40 ppm (not observed in our system here, presumably because they are too weak) were previously suggested to be associated with excess Li ions that replace Co^{3+} sites in the bulk, resulting in a defect structure discussed above, with two adjacent square-based pyramids containing two intermediate-spin Co^{3+} ions per oxygen vacancy.[72] Even in the 30 nm sample, the percentage of excess Li is only approximately 0.6%. Two new hyperfine-shifted resonances were observed at -115 and -260 ppm (Fig. 4.4b), which are attributed to the presence of intermediate and/or high spin Co^{3+} (IS, HS). To the best of our knowledge, these shifts have not been reported in the literature. An analysis of the spin density on the {104} surface, as shown in Figure 4.2(b), indicates that the Li^{+} ions on this surface contain negative spin density and will thus give rise to a negative shift. Integration of the spin density around the Li nucleus to 0.8 Å, using the approach developed by Carlier et al.[83] confirms this observation and indicates that the Li nuclei in the subsequent {104} surface is negative, while the spin density of the Li in the layer below is smaller, but positive (and thus it may be difficult to resolve from the intense bulk $LiCoO_2$ resonance/and or be buried under the spinning sidebands). Further calculations will focus on the direct calculations of hyperfine shifts[84,85] on this and a wider range of surfaces. Importantly, quantitative fitting of the NMR spectra to extract the concentration of Li^{+} ions nearby paramagnetic Co ions, confirms that the percentage of paramagnetic ions increases with decreasing particle size.

Magnetic measurements were performed, using a superconducting quantum interference device (SQUID), at a magnetic field of 1.0 T in the temperature range of 5-

300K. The molar magnetic susceptibility of the various sized nano-$LiCoO_2$ particles are plotted as a function of temperature in Figure 4.5a. The magnetic susceptibility of bulk $LiCoO_2$ is low and practically temperature independent, which is attributed to a Van Vleck-type of paramagnetism associated with diamagnetic Co^{3+} (LS) in the layered structure.[86] In contrast, our nano-size $LiCoO_2$ exhibits a typical Curie-Weiss behavior for T>100K. The Curie constant was determined in the temperature range of 200-300K. The Curie constant increases with decreasing particle size and fitting of the Curie constant indicates that the molar Curie constant is as high as 0.20 in 10nm-sized $LiCoO_2$.

Careful transmission electron microscopy (TEM) examination of the nano-sized $LiCoO_2$ shows that all particles exhibit plate-like morphology, plates corresponding to the {001} planes; the edges are dominated by the {104} planes justifying our computational study of this surface. If the planes are terminated by the {001} surface, according to first principles computation of this work and previous work by Kramer and Ceder,[79] Co^{3+} remains octahedrally coordinated with a low-spin configuration. The contribution of Co^{3+} (IS) on the {104} and the Co^{3+} (HS) on the {110} surfaces are most likely attributing to the abnormally high magnetic susceptibility seen in nano-size $LiCoO_2$.

The proposed electronic spin state of the surfaces relevant for (de)intercalation has significant impact on the lithium (de)intercalation voltage profile, as revealed by first principles computation performed to calculate the Li extraction potential from different surfaces. If Co^{3+} remains as LS on the {104} surface, the voltage of lithium extraction is as low as 2.32V; by contrast, when a spin transition from LS to IS occurs, the voltage of lithium extraction is 3.69V, close to the bulk value of 3.65V. The narrowing energy gap between the occupied and unoccupied states in IS and HS state Co ions indicates that the

insulating nature of $LiCoO_2$ can be altered due to the change in spin state (see Figure 4.6). This helps in explaining the fact that in the lithium half-cell with nano-sized $LiCoO_2$ as the cathode, a clear first order phase transition, associated with the metal-insulator-transition, is absent as no flat voltage plateau is observed upon the first charge[87] (see Figure 4.7).

4.1.4 Conclusions

In conclusion, it is proposed in this work that electronic spin state transitions occur on the surfaces of stoichiometric $LiCoO_2$, where trivalent cobalt ions adjacent to the surface adopt an intermediate spin state if it they are square pyramid coordinated and a high spin state if they are pseudo-tetrahedrally coordinated. This phenomenon is quantified in nano-sized stoichiometric $LiCoO_2$. We also observed in first principles calculations that both {104} and {110} surfaces with optimized electronic spin states expand normal to the surface and the displacement is of the order of 0.1-0.2Å. This work suggests that changes in electronic spin state could be a common phenomenon in transition metal oxides. The low coordinated geometries on the surface of the oxides result in spin states that are distinct from the bulk. Consequently, unique magnetic and electronic properties arise and alter the materials performance in devices. We show that in this case, the voltage profile of (de)intercalation is dramatically changed. It is therefore promising to control the surfaces and interfaces of nano-sized materials to alter the electronic and magnetic properties, significantly different from the bulk behaviors.

4.2 The Role of $LiCoO_2$ Surface Terminations in Oxygen Reduction and Evolution Kinetics

4.2.1 Introduction

Recent studies have shown that electronic structure features of oxides such as e_g occupancy[88-90] of transition metal ions could govern the ORR/OER activities of transition metal oxides, where having an e_g occupancy close to unity showed maximum specific ORR and OER activity.[88,89] More recently, it has been found that moving the O p band center closer to the Fermi level leads to much enhanced specific OER activity.[91] In addition, a better flexibility of transition metal atoms to adopt various oxidation and spin configurations is also correlated to higher OER activity.[92]

From the previous studies, it has been reported the nanosized stoichiometric rod-shaped $LiCoO_2$ rods have low-spin Co^{3+} on the nanorod sides terminated with (003) facets and intermediate- or high-spin Co^{3+} on tips that are usually dominated by high-index surfaces such as (104).[93] The difference would result in the electronic structure differences from tips to sides, with a narrowing in band gap for the spin-transited Co^{3+} on the tips compared to the sides from the DOS (density of states) calculations. The corresponding electrochemical performance alters from the nanorods to the bulk $LiCoO_2$, lacking a plateau corresponding to the metal-insulator transition.

In this study, the ORR and OER activities and pseudo-capacitance of these rod-shaped $LiCoO_2$ were studied in 0.1 M KOH. Higher specific ORR and OER activities accompanied by higher charge transfer per surface area during Co 2+/3+ and 3+/4+ redox processes were found at the tips, compared with the side surfaces (due to the difference in e_g occupancies for sides and tips)

4.2.2 Methodologies

4.2.2.1 Electrochemical Measurements

The rotating disk electrode (RDE) configuration was employed for electrochemical measurements. All potentials were calibrated to the reversible hydrogen electrode (RHE) using H_2/H^+ redox. $LiCoO_2$ samples were mixed with the oxides: AB carbon: Nafion® ratio of 5:1:1, and the oxides loading on the disk is 0.25 mg/cm^2_{disk}. All electrochemical measurements were done in 0.1 M KOH, with IR (resistance determined using electrochemical impedance spectroscopy) and double-layer capacitance corrections when available. All measurements were repeated 3 times to establish good reproducibility.

4.2.2.2 Transmission Electron Microscopy

TEM images were taken on JEOL 2010F with a point resolution of 0.19 nm, used to determine particle size distributions and general morphology of the catalyst nanoparticles. High resolution TEM images were formed without an objective aperture and were analyzed using Gatan Digital Micrograph v2.01 (Gatan Inc.). $LiCoO_2$ particles were assumed to have a rod shape with different sizes and are noted using their average diameters of 9nm, 14nm, 31nm and 40 nm, determined by TEM images. The surface areas were computed using the particle dimension distributions (Figure 4.8c) collected from TEM images and the following equations[94]:

$$S_{tip} = \frac{\sum_i 2\pi D_i^2/4}{\rho \sum_i \pi D_i^2 L_i/4} = \frac{2\sum_i D_i^2}{\rho \sum_i D_i^2 L_i} \qquad \text{Eq. 1}$$

$$S_{side} = \frac{\sum_i \pi D_i L_i}{\rho \sum_i \pi D_i^2 L_i/4} = \frac{4\sum_i D_i L_i}{\rho \sum_i D_i^2 L_i} \qquad \text{Eq. 2}$$

$$S_{total} = S_{tip} + S_{side} \qquad \text{Eq. 3}$$

where ρ is the density of bulk $LiCoO_2$, D_i and L_i are the diameter and length of $LiCoO_2$ nanoparticles.

4.2.2.3 EELS

Electron Microscopy work was carried out on a Cs-corrected FEI Titan 80/300-kV TEM/STEM microscope equipped with a Gatan Image Filter Quantum-865. All EELS spectra were acquired at 60 kV and with a beam size of ~0.7Å, except for those of control measurements samples which were acquired at 300 kV. Judged from the full width at half height (FWHH) of the zero loss peak, the energy resolution is ~1eV. EELS spectra shown in this work were acquired from a rectangular area of ~1 X 2 nm with an acquisition time of 3 seconds and a collection angle of 39mrad. For each sample, at least six particles' (six side-tip sets) spectra were collected. The energy axis was calibrated using the zero loss peak.

4.2.3 Results and Discussions

The $LiCoO_2$ nanorods were characterized firstly by transmission electron microscopy (TEM). These nanorods have similar morphologies but different sizes and were denoted by their average diameter of 9, 14, 31 and 40 nm (Figure 4.8). The calculation of tip and side surface areas can be found in Table 4.4. The geometric ORR and OER activity in Figures 4.11 suggested that the smaller the particle size, the higher the total activity, due to the higher total surface area of the smaller nanorods. The tip surfaces are ~10 times more active for ORR than the side surfaces, and the difference is ~4 times in OER. In addition to OER and ORR, the tip of $LiCoO_2$ nanorods was found to

be more redox active than the side surfaces in the redox of surface Co atoms, shown in Figure 4.12.

Electron energy loss spectroscopy (EELS) analysis of $LiCoO_2$ nanorods suggested that the tips could have lower hybridization of Co-O bounds than the sides. Representative EELS spectra of the pristine 9-nm sample are shown in Figure 4.9a and b, where the position of EELS acquisition is shown in Figure 4.10. The Co L_3/L_2 ratios of ~2.7 were comparable to those of our previous XPS results,[93] indicative of Co oxidation state of 3+, and no noticeable changes in the Co L_3/L_2 ratio was observed between side and tip. For O K spectra, the area of the pre-peak was linearly proportional to the product of the total number of the empty O 2p − Co 3d states (4 for Co^{3+} considering equal weighting of e_g and t_{2g} electrons) and their extent of hybridization.[90] The quantitative analysis of the difference of O pre-peak areas between sides and tips can be found in Table 4.5, where the side of pristine $LiCoO_2$ showed a ~20% larger pre-peak area in the O K-edge than the tip at around 532 eV, consistent with our previous study on $LiCoO_2$ nanorods.[93] The smaller pre-peak on tips suggested an intermediate- or high-spin Co^{3+} with weaker hybridization of O 2p and Co 3d, originated from the under-coordinated Co atoms on tip surfaces, [93] while the fully-coordinated Co atoms on nanorod sides have a low-spin state with a greater degree of O 2p and Co 3d hybridization. Such difference in electronic structures between tips and sides could play an important role in surface catalytic reactions.

The surface Co redox can also be confirmed from EELS: after ORR the Co L3/L2 ratio increased from original ~2.7 to ~3.8 for tips and to ~3.1 for sides (Figure 4.9c and Table 4.7), indicating the partially reduction of surface Co atoms[95]; while after OER, the

L3/L2 ratio decreased to ~2.5 for tips and is still ~2.7 for sides (Figure 4.12a and Table 4.7), indicating the partially oxidation of Co on tips. The change of L3/L2 ratios on tips are larger than on sides, and the change after ORR is larger than after OER, which is also in consistent with the result that tips have larger charge transfer than side and Co2+/3+ redox process has larger charge transfer than 3+/4+ redox.

After ORR or OER measurements (holding at 0.7 or 1.55 V vs. RHE for 1 h), 50% of $LiCoO_2$ nanorods examined were found to have maintained a smaller O K pre-peak on the tip (peak area <3.5, similar to the pristine tip) than that on the side (peak area >4, similar to the pristine side), as shown in Figures 4.9d, 4.12b and case 1 in Table 4.5. This indicates the open structure can be at least partially kept during OER and ORR on the tip. This can explain the higher ORR/OER activities of the tip as compared to the side, since the open structure and the under-coordinated Co ions on tips can adsorb oxygen species from the electrolyte more easily and therefore could promote ORR kinetics at the side, with the oxygen being more easily to dissociate/intercalate.[88,89,92] We also found 50% of the $LiCoO_2$ nanorods showed comparable O K pre-peak areas between tip and side after OER or ORR, all close to the pre-peak of pristine side surface (peak area ~4.5), as shown in Figures 4.9f, 4.12d and case 2 in Table 4.5. This can also be observed in a control experiment with the pristine sample immersed in O_2-saturated 0.1 M KOH electrolyte for 1 h (Figure 4.14 and Table 4.5). This changing of tip pre-peak area is probably due to the under-coordinated surface Co on the tip getting bonded by water or OH/OOH groups and then the surface reconstructed, making the coordination and chemical environment of Co atoms on the tip become similar to that on the side. During control experiment, the $LiCoO_2$ nanorods statically contacted and adsorbed water

or OH/OOH groups for a long time, which led to the gradually reconstruction of all the under-coordinate Co on tips; while during ORR or OER, the OH/OOH group adsorbed on under-coordinate Co ions is continuously consumed and re-adsorbed, and therefore the active Co sites on the tip surface are cyclically regenerated without long-time OH/OOH group adsorption, which might be the reason that only some of the nanorods lost their under-coordinated tips after ORR or OER.

4.2.4 Conclusions

In summary, we report that the tip surface of rod-shaped $LiCoO_2$ nanoparticles, with high index surfaces such as (104), has higher ORR and OER activity as compared to the side with low index surfaces. In addition, the tip surface has larger specific charge transferred than the side for both Co 2+/3+ and 3+/4+ redox processes. The easier access to oxygen species and easier redox of under-coordinated Co atoms on high-index tip surfaces are used to explain the difference in catalytic performance between tips and sides. These findings showed that the surface catalytic reactions, such as OER and ORR, are closely related to surface terminations that determine the surface atomic and electronic structures of transition metals oxides. Therefore, the controlling and modification of surface terminations could be an effective way to design future catalysts.

Chapter 4, part 1, in full, is reprinted with permission from the following paper "Electronic spin transition in nanosize stoichiometric lithium cobalt oxide", Journal of the American Chemical Society, 2012, 134(14), 6096-6099 by Danna Qian, Y. Hinuma, H.

Chen, L-S Du, K. Carroll, G. Ceder, C. P. Grey, Y. S. Meng, Copyright (2012) American Chemical Society. The second part, in part, is reprint from "The role of $LiCoO_2$ surface termination in oxygen reduction and evolution kinetics" being submitted by B. Han, Danna Qian (equally contributed), M. Risch, H. Chen, M. Chi, Y. S. Meng, Y. S-H.. The dissertation author was the primary investigator and author of the papers.

Figures:

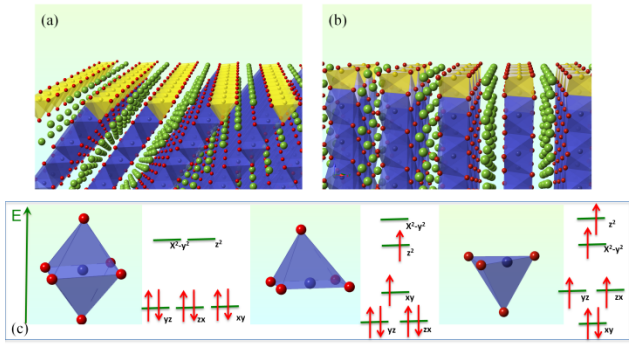

Figure 4.1: (a) {104} and (b) {110} surfaces of $LiCoO_2$ (c) Octahedrally, square pyramid and pseudo-tetrahedrally coordinated Co ions. (red- oxygen, green – lithium, blue – Co)

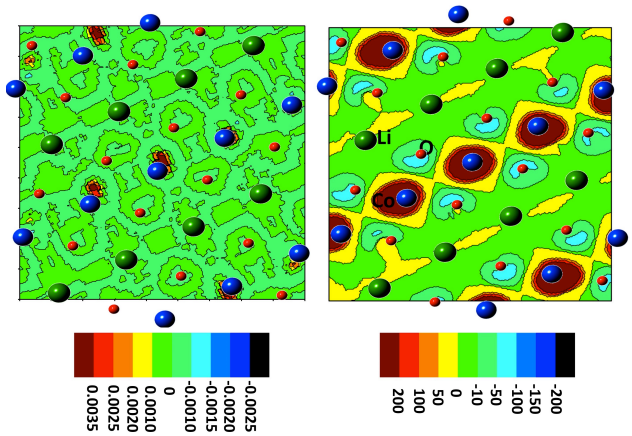

Figure 4.2: Spin density plot of the {104} plane of the bulk (a) and the surface (b). (Notice the scale differences in the spin density)

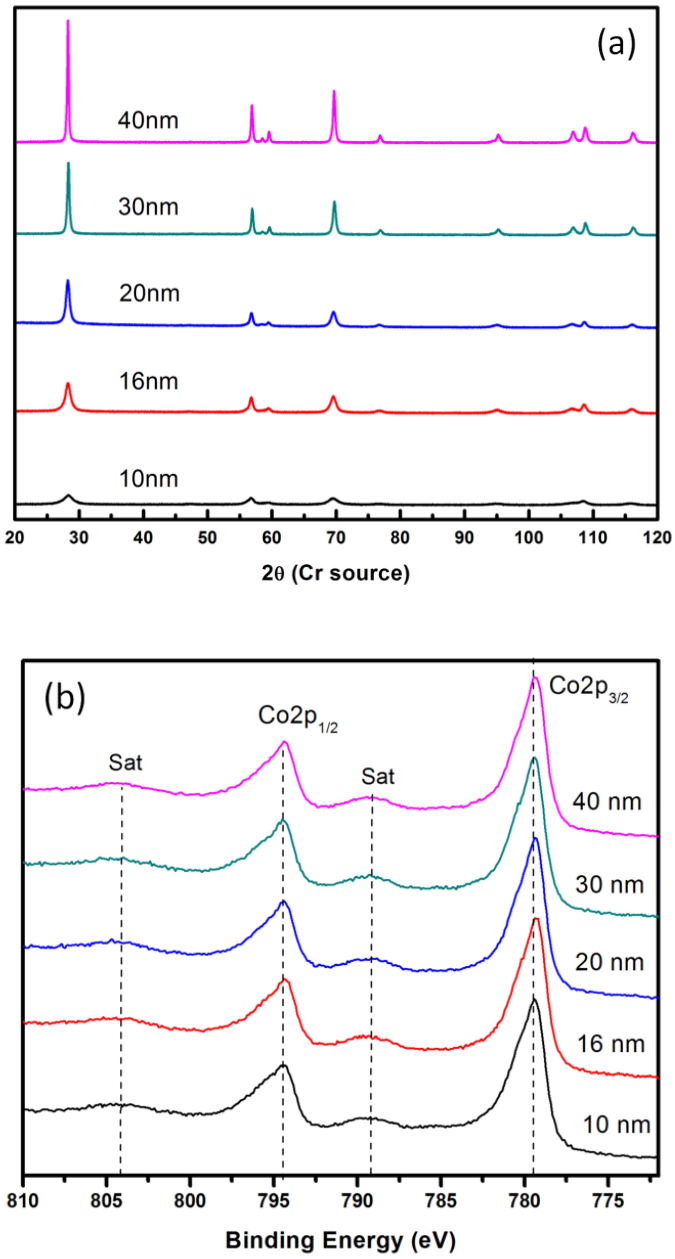

Figure 4.3: (a) XRD and (b) XPS spectra of nano-sized stoichiometric $LiCoO_2$.

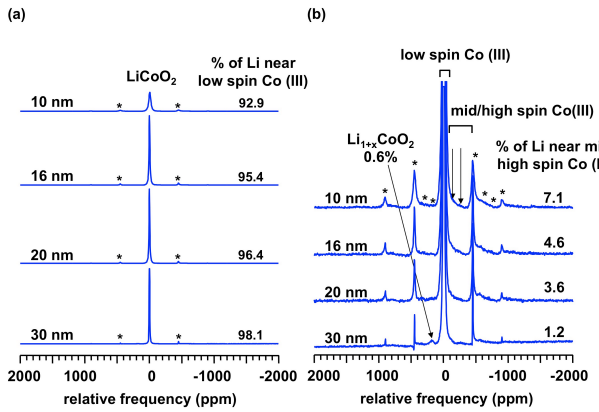

Figure 4.4: ^{7}Li MAS NMR spectra of $LiCoO_2$ with varying particle sizes. (a) Percentages of the Li near by low spin Co (III) in $LiCoO_2$ are listed in (a). Peak assignment and percentages of Li ions in environments nearby paramagnetic ions can be found in enlarged spectra. (b) Asterisks denote spinning sidebands.

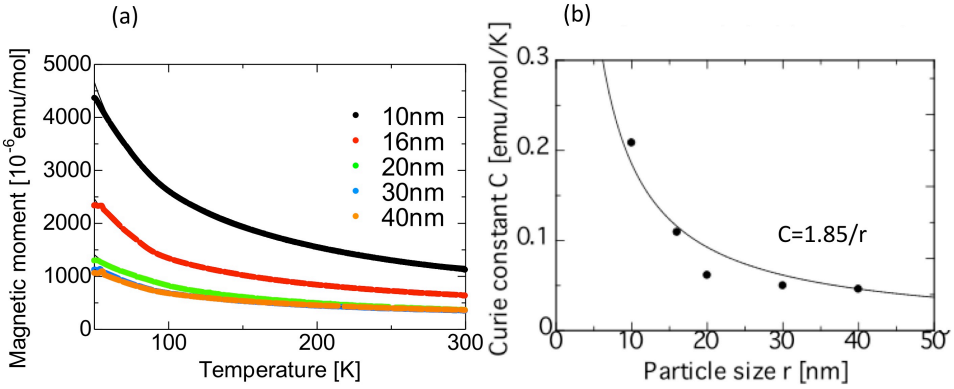

Figure 4.5: (a) Molar magnetic susceptibilities of particle size 10nm, 16nm, 20nm, 30nm and 40nm samples as a function of temperature. (b) The Curie constants of these samples determined from the $1/\chi$ vs T. (Both are measured with sample holder corrected)

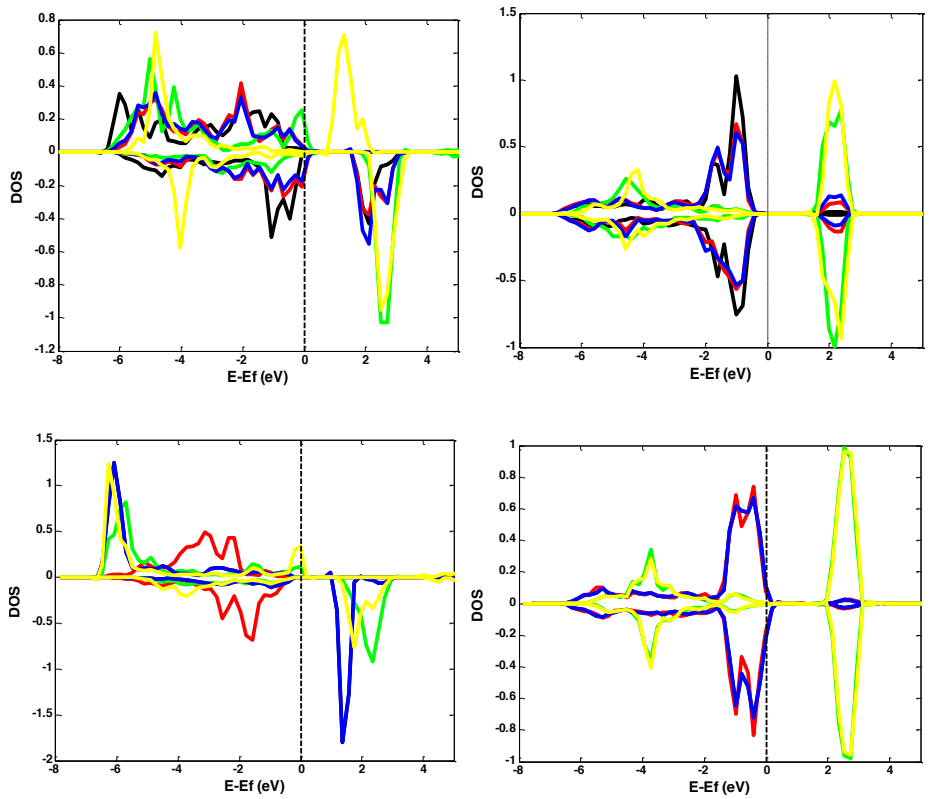

Figure 4.6: Projected density of states (DOS) of Co ions on the surface and bulk of $LiCoO_2$. Upper: {104} surface Co with IS (left) and bulk Co with LS (right); Bottom: {110} Surface Co with IS (left) and Bulk Co with LS (right)

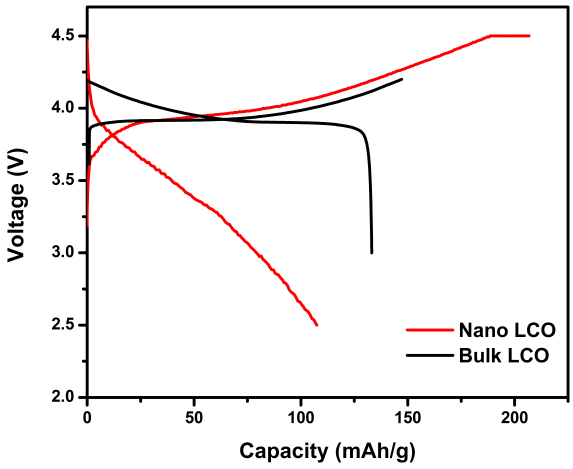

Figure 4.7: Electrochemical data for both bulk-$LiCoO_2$ (black) and 10nm-$LiCoO_2$ (red) in a lithium half-cell.

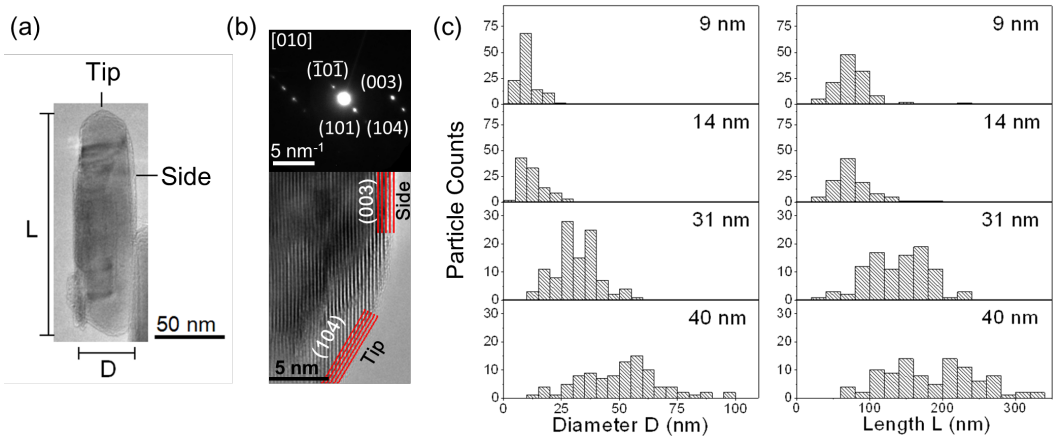

Figure 4.8: (a) Representative TEM image of a nanorod from the $LiCoO_2$ sample with an average rod diameter of 40 nm. (b) High-resolution TEM image of a representative nanorod $LiCoO_2$ with its associated selected-area electron diffraction pattern. (c) Histograms of the length and diameter distributions of different $LiCoO_2$ samples.

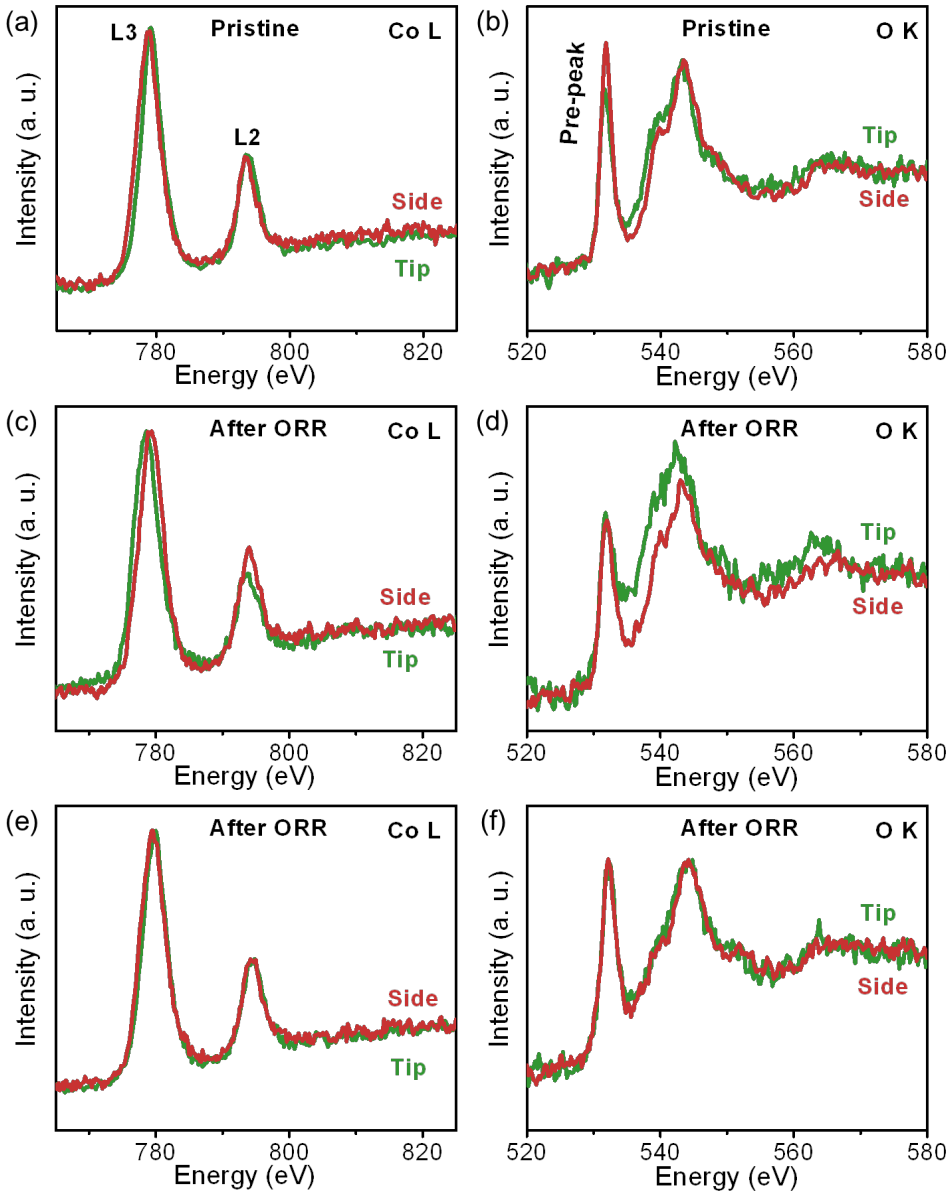

Figure 4.9: (a)(b) Representative EELS spectra of pristine 9-nm $LiCoO_2$: (a) Co L edge, (b) O K edge. (c)-(e) Two types of representative EELS spectra of 9-nm sample held at 0.7 V vs. RHE for ORR. Middle row is one set of (c) Co L edge and (d) O K edge (case 1); bottom row (e) and (f) is the other set of spectra (case 2). The analysis of O K pre-peak (at 532 eV) intensities can be found in Table 4.5.

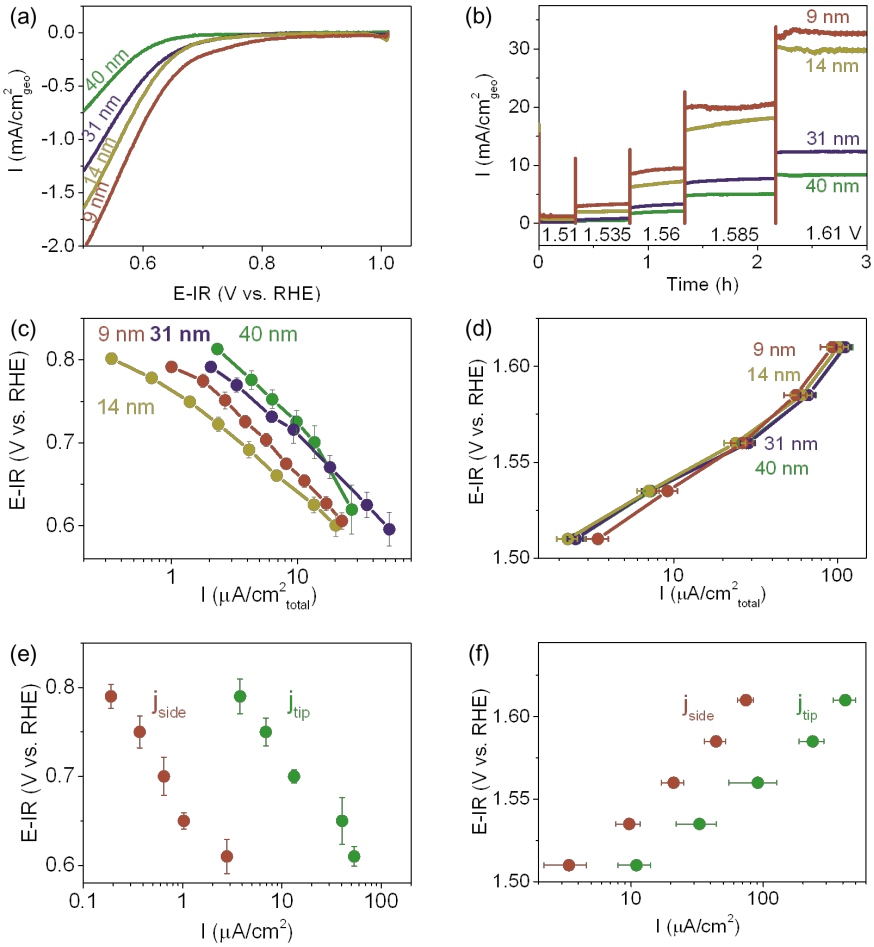

Figure 4.10: (a) Cyclic voltammetry of ORR current of different $LiCoO_2$ samples in O_2-saturated 0.1 M KOH at 10 mV/s. (b) Potentiostatic measurements of OER current of different $LiCoO_2$ samples in O_2-saturated 0.1 M KOH at different voltages. (c-f) Tafel plots of ORR and OER activities: (c) and (d) Tafel plots of ORR and OER activities of $LiCoO_2$ normalized by total surface area estimated from TEM particle size distribution,[94] respectively. The error bars represent the standard deviation of three different measurements for each sample. (d) and (f) Tafel plots of the specific ORR and OER activities of tip and side surfaces of $LiCoO_2$. The error bars were obtained from linear regression of j_{side} and j_{tip} .

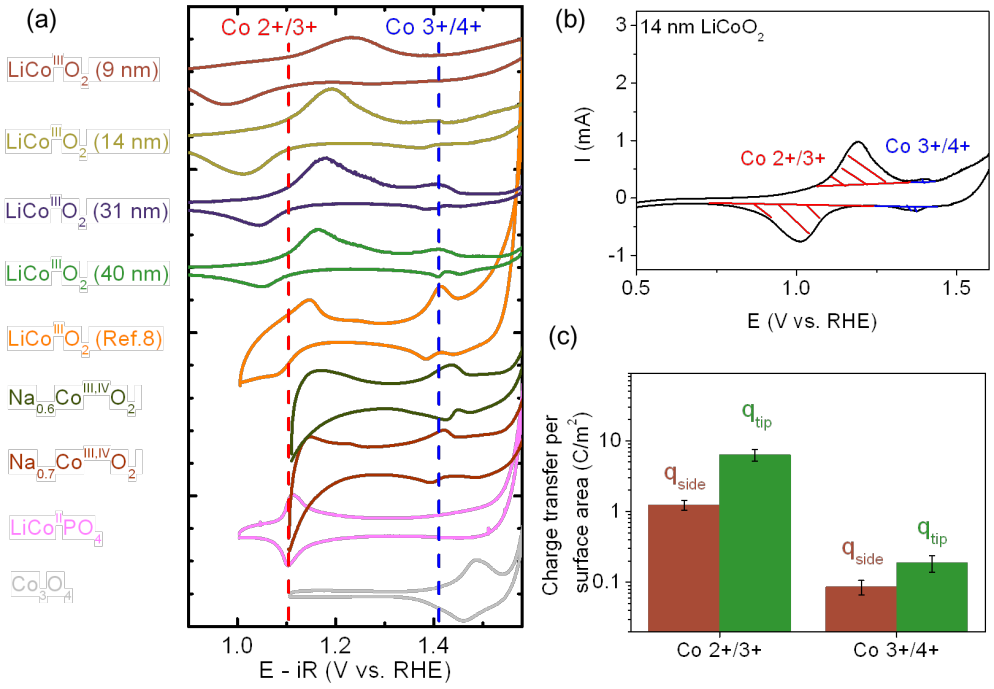

Figure 4.11: (a) CV curves of different Co compounds in the Co redox region. (b) Calculation scheme of charge transfer during Co 2+/3+ and 3+/4+ redox reactions by integrating the redox peaks. (c) Charge transferred per surface area of tip and side surfaces of $LiCoO_2$ during 2+/3+ and 3+/4+ redox processes.

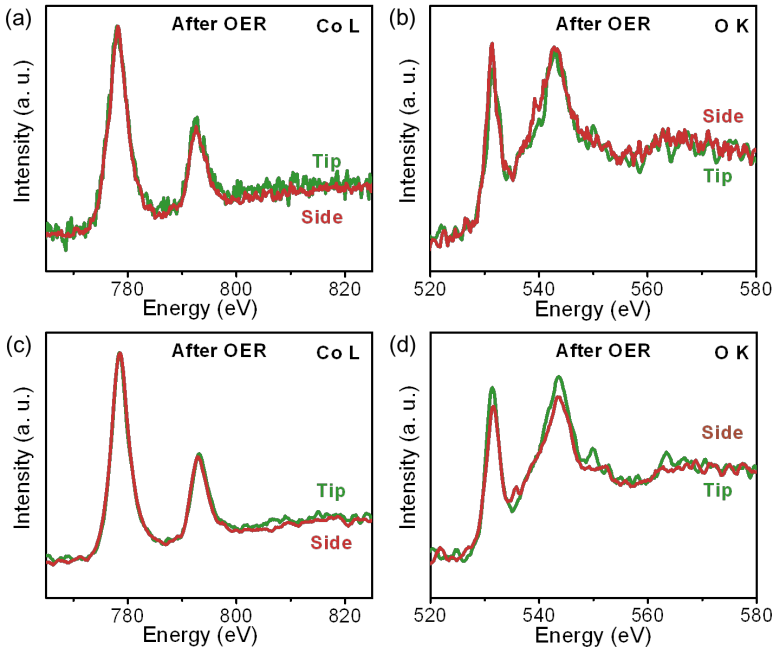

Figure 4.12. Two types of representative EELS spectra of 9 nm sample held at 1.55 V vs. RHE for OER. Upper row is one set of (a) Co L edge and (b) O K edge (case 1); bottom row (c) and (d) is the other set of spectra (case 2). These two types of spectra were observed at the same frequency on particles.

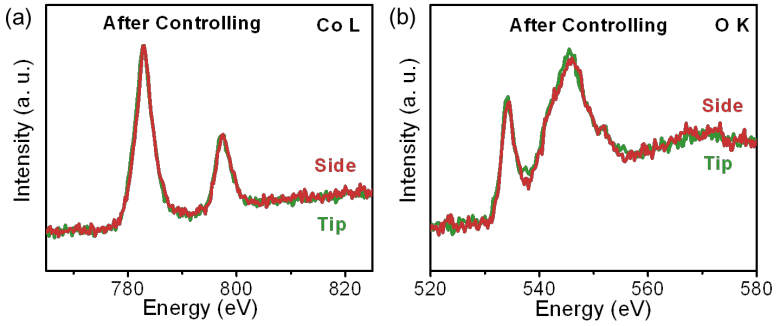

Figure 4.13. Representative EELS spectra of 9 nm sample that was immersed in 0.1 M KOH electrolyte for 1 hour without applying any potential. Then sample was rinsed by DI water and tried in air at room temperature. These spectra were taken under 300 kV. (a) Co L edge and (b) O K edge.

Tables:

Table 4.1: Synthesis conditions and altered parameters to give the desired stoichiometric $LiCoO_2$ particle size.

$LiCoO_2$ Sample	Molten salt composition (molar ratio)	Heating time (hour)
10 nm	$LiNO_3$-LiOH (6 : 4)	0.5
16 nm	$LiNO_3$-KOH-LiOH (6 : 2.8: 1.2)	1
20 nm	KOH-LiOH (7 : 3)	0.5
30 nm	KOH-LiOH (7 : 3)	2
40 nm	KOH-LiOH (7 : 3)	6

Table 4.2: Rietveld Refinement fit parameters and the calculated *a* and *c* lattice parameters for the various sized stoichiometric $LiCoO_2$ nanoparticles.

Size (nm)	**R_{wp}**	**R_b**	**a**	**c**	**c/ a ratio**
40	3.74	0.7717	2.816738	14.056028	4.990
30	4.27	0.7956	2.817727	14.065305	4.992
20	8.8	1.749	2.814981	14.062336	4.996
16	6.78	1.371	2.822156	14.069565	4.985
10	N/A				

Table 4.3: Calculated surface energy w/o spin transition compared with literature

Surface	Coordination # of oxygen	γ (mJ/m^2) ref[79] with LS	γ (mJ/m^2) this work with LS	γ (mJ/m^2) this work spin trans.
{104}	5/6	1048	1118	312
{110}	4/6	2241	2227	1241

Table 4.4: The mass-normalized tip, side and total surface areas of each $LiCoO_2$ sample, computed using the particle size distributions collected from TEM images. The BET surface areas are also given for comparison. See detailed experimental session for more information.

	9nm	**14nm**	**31nm**	**40nm**
S_{tip} (m^2/g)	8.9	7.8	4.4	3.3
S_{side} (m^2/g)	133	111	40.4	26.7
S_{total} (m^2/g)	142	118	44.8	30.0
S_{BET} (m^2/g)	270	230	74	58

Table 4.5: The O K pre-peak area of tips and sides. The calculation method can be found in Figure S3. Samples were treated in O_2-saturated electrolyte at 0.7 V, 1.55 V (vs. RHE) and without applying potential for 1 h for the post-OER, and post-ORR and controlling measurements, respectively. For each column, the pre-peak intensity of three different particles were calculated to give the average value and standard deviation in the table.

	9nm pristine	9nm controlling	9nm 0.7V		9nm 1.55V	
			Case 1	Case 2	Case 1	Case 2
Tip	3.21±0.11	4.05±0.29	2.84±0.44	4.38±0.31	3.49±0.14	4.44±0.23
Side	4.47±0.13	4.23±0.45	4.04±0.25	4.23±0.23	4.21±0.20	4.38±0.15

Table 4.6: The mass-normalized and total-surface normalized charge transfer during Co 2+/3+ and 3+/4+ redox processes of each $LiCoO_2$ sample, measured from CV current in 0.1 M KOH at 5 mV/s after the double-layer current correction (see Figure 4b). The charge transfer was integrated from 0.7 to 1.3 V vs. RHE for Co 2+/3+ redox and from 1.3 to 1.4 V vs. RHE for Co 3+/4+ redox, and was averaged between forward and backward scanning.

	9nm	**14nm**	**31nm**	**40nm**
$Q_{Co2+/3+}$ (C/g)	240	198	74	56
$q_{Co2+/3+}$ (C/m^2)	1.70	1.68	1.65	1.87
$Q_{Co3+/4+}$ (C/g)	21	18	8	6.2
$q_{Co3+/4+}$ (C/m^2)	0.14	0.15	0.18	0.21

Table 4.7: The Co L3/L2 ratios of tips and sides. The ratio was calculated after a double-step background correction.[95] Samples were treated in O_2-saturated electrolyte at 0.7 V, 1.55 V (vs. RHE) and without applying potential for 1 h for the post-OER, and post-ORR and controlling measurements, respectively. For each column, the ratio of three different particles were calculated to give the average value and standard deviation in the table. The standard L3/L2 ratios for Co 2+, 3+ and 4+ are about 4.8, 2.8 and 2.0, respectively.[95]

	9nm pristine	9nm controlling	9nm 0.7V		9nm 1.55V	
			Case 1	Case 2	Case 1	Case 2
Tip	2.73±0.09	2.82±0.11	3.77±0.24	3.09±0.05	2.50±0.10	2.61±0.08
Side	2.70±0.11	2.80±0.12	3.07±0.15	2.92±0.05	2.74±0.15	2.63±0.09

5 UNCOVERING THE ROLES OF OXYGEN VACANCY ON CATION MIGRATION IN LITHIUM EXCESS LAYERED OXIDES

5.1 Introduction

In spite of researches on various kinds of materials in the past decades, lithium intercalation compounds still provide the best performances as the cathode materials for lithium ion batteries (LIB). Among all candidates, the lithium-excess layered oxides have gained growing research interests in recent years. It can reach more than 250 mAh/g capacity with average voltage of 4V, making it the candidate with highest energy densities among all known intercalation compounds for cathode materials.[96-102] Being source of major capacity improvement, the extra lithium ions, on the other hand, also cause unexplained phenomena in lithium-excess layered oxides. The rate performances of these materials are usually poor, and electron sources for the extra capacities have been under debate for years.[99,103-106] In classical layered oxides, the transition metal (TM) oxide host TMO_2 should remain its host structure during initial discharging/charging, while lithium ions are intercalated/de-intercalated from the host. In contrast, recent studies suggested that in lithium-excess layered oxides, certain amount of surface transition metal ions migrate from the transition metal layers to lithium layers during the very first charging/discharging cycle.[107-112] These migrated ions are very stable in the lithium layers. They will likely block the lithium diffusion pathways and slow the lithium diffusion rates. Since the migrated surface transition metal ions could be one of the main factors that limit the material rate performances, and possibly cause instabilities in voltage profile, it is crucial to understand their diffusion mechanism. Our previous work[29,30,112,113] has suggested that the migration may be assisted by oxygen vacancies

generated in the late charging states of first cycle, but two critical questions remain unanswered: 1) how can we visualize the change in structure and chemical content at atomic level and 2) what is the energy required for oxygen vacancies formation upon cycling and how do they assist transition metal migrations. To answer these questions, a systematic study on generations of oxygen vacancies in Li-excess layered oxide $Li[Li_{1/6}Ni_{1/6}Co_{1/6}Mn_{1/2}]O_2$ was performed using Scanning Transmission Electron Microscope / Electron Energy Loss Spectroscopy (STEM/EELS) experiments, and studies by first principles computational method were performed on its analogue $Li[Li_{1/6}Ni_{1/4}Mn_{7/12}]O_2$. EELS characterized the local oxygen and TM environments at the two phases and the interface region. The local diffusion barriers of TM ions were calculated with the presence of oxygen vacancy, and a hypothesis of transition metal ion migration mechanism is proposed.

5.2 Methodologies

5.2.1 STEM/EELS

Electron Microscopy work was carried out on a Cs-corrected FEI Titan 80/300-kV TEM/STEM microscope equipped with a Gatan Image Filter Quantum-865. All STEM images and EELS spectra were acquired at 300 kV and with a beam size of ~0.7Å. EELS spectra shown in this work were acquired from a square area of ~0.5*0.5 nm with an acquisition time of 3 seconds and a collection angle of 35mrad. HAADF images were obtained with a convergence angle of 30mrad and a large inner collection angle of 65mrad. Images acquired by an HAADF detector with a small convergence angle and a relative large inner collection angle are also called “Z-contrast” images, where the

contrast is proportional to $Z^{1.7}$.[114,115] In atomic resolution Z-contrast images, the contrast of the atomic columns thus can be used to differentiate different elements and provide atomic-structural information.

To minimize possible electron beam irradiation effects, EELS and HAADF figures presented in this work were acquired from areas without pre-beam irradiation.

5.2.2. Computation details

First principles calculations were performed in the spin-polarized GGA+U approximations to the Density Functional Theory (DFT). Core electron states were represented by the projector augumented-wave method[116] as implemented in the Vienna ab initio simulation package (VASP).[74,117,118] The Perdew-Burke-Ernzerhof[119] exchange correlation and a plane wave representation for the wavefunction with a cutoff energy of 450eV were used. The Brillouin zone was sampled with a dense k-points mesh by Gamma packing. The four-layered supercell composed of 12 formula units of $Li[Ni_{1/4}Li_{1/6}Mn_{7/12}]O_2$ used in previous work is used again to obtain the trend of oxygen vacancy formation energies. The atomic positions and cell parameters are fully relaxed to obtain total energy and optimized cell structure. To obtain the accurate electronic structures, a static self-consistent calculation is run, followed by a non-self-consistent calculation using the calculated charge densities from the first step. The cell volume is fixed with internal relaxation of the ions in the second step calculation. The Hubbard U correction was introduced to describe the effect of localized d electrons of transition metal ions. The applied effective U value given to Mn ions is 5eV and to Ni ions is 5.96eV.[120]

A new supercell composed of 24 formula units by doubling previous supercell along the c direction is used to investigate Ni diffusion mechanisms. Nudged Elastic Band (NEB) method is used to find the minimum energy path and the energy barrier for Ni diffusion inside the materials. All models are established as bulk materials, and no oxygen diffusion is considered in this work.

To calculate formation energies of oxygen vacancy in $Li_xNi_{1/4}Mn_{7/12}O_2$ bulk, both types of supercells were used for investigations and only one vacancy was created in each cell. This is equivalent to oxygen vacancy concentration between 2% to 4%, which satisfies the dilute defect conditions. Following two equations were used to calculate the formation energy of oxygen vacancies in $Li_xNi_{1/4}Mn_{7/12}O_2$:

$$E_{fov} = E\left(Li_nNi_3Mn_7O_{23}\right) + 1/2\,E\left(O_2\right) - E\left(Li_nNi_3Mn_7O_{24}\right) \quad (1)$$

and

$$E_{fov} = E\left(Li_mNi_6Mn_{14}O_{47}\right) + 1/2\,E\left(O_2\right) - E\left(Li_mNi_6Mn_{14}O_{48}\right) \quad (2)$$

where $E(O_2)$ is the calculated energy of the oxygen gas plus a 1.36 eV correction according to previous reports [121].

5.3 Results and Discussions

To visualize the material structural change upon cycling from atomic level, aberration corrected high angle annular dark field (HAADF) STEM images of the material particles were obtained and shown in Figure 5.1(left). Similar to previous observations, TM ions were found in Li layer in the surface and subsurface region, forming a defect spinel structure that is different from the layered structure in bulk.[112] For

quantitative analysis, EELS experiments were carried out on the phase transformation region. Spatially resolved EELS were obtained at a step of ~0.6 nm from surface to bulk and the spectra are presented in Figure 5.1(right). The data points are aligned with the STEM image to indicate where each spectrum was taken. For example, the black (data point 9) and red curves (data point 8) were acquired from the surface and near surface region, the blue (data point 7) curve was acquired from the spinel-layered interface, and the orange (data point 1) curve was acquired from the bulk. The onset energy of O K-edge pre-peak is aligned to 532eV. Therefore, our analysis of the O K-edge is limited to the fine structures and not the chemical shift of O K-edge. In Figure 5.1, there is a clear O pre-peak in the spectra obtained in bulk. This pre-peak starts to decrease when it comes to the interface region of the spinel-like and layer phase, and disappears completely in the spinel-like phase near surface. The splitting of the O K-edge usually corresponds to the splitting of the TM *3d* orbitals in six-coordinated environment. The disappearance of the pre-peak can be ascribed to the following two main reasons: 1) the neighbor TM being reduced; 2) oxygen vacancy formation, the splitting of neighbor TM 3d orbitals is no longer the same as six-coordinated. Usually the TM reduction comes along with oxygen vacancy formation due to charge compensation. In this case, there were synchrotron XRD studies showing oxygen loss at the late charging state.[122] Therefore it is strongly evident that oxygen vacancies were presented mostly at the surface region where the spinel-like phase formed, and gradually disappeared when it came to the bulk of the layer phase.

From the STEM/EELS results, it is clear that TM ion migration only happens in the region where the oxygen vacancy presented. First principles calculations were then carried out for deeper understandings of the material from atomic level. As depicted in

the inset of Figure 5.2(a), each oxygen ion is bonded with 6 nearest cations. Three of them are Li ions in lithium layer and the other three in TM layer can be Li, Ni or Mn. There are four different combinations of the three cations in TM layer. These configurations are indicated by black circles in Figure 5.2(a) and noted by *a, b, c* and *d*. Oxygen vacancies can be located in these different local atomic configurations at different lithium concentrations. More than 70 calculations were performed with oxygen vacancies in different atomic configurations. A general trend of calculated oxygen vacancy formation energies (E_{fov}) versus lithium concentrations is shown in Figure 5.2(b).

The lithium concentration of these calculations covers from 28/28 (fully lithiated) to 14/28 (half delithiated), the range of which correspond to the slopy region of the first charging voltage curve. It is clear that E_{fov} decreases sharply from ~2.7eV at fully lithiated state to less than 1eV for Li concentration between 20/28 to 14/28. Note that at Li concentration 20/28, the tetrahedral Li-Li dumbbells begin to form, leading to the possible formation of spinel-like phases.[112] After that, E_{fov} becomes relatively stable. Our data show a surprisingly consistent trend of E_{fov} in terms of local atomic configurations. E_{fov} is usually low in configuration *d* while is usually high in configuration *a*. The results show a strong preference to certain local atomic environments for vacancy formation. Oxygen vacancies are more likely to form when their local environments are Li-Ni-Mn combinations in transition metal layer. Electrostatic effect may partially contribute to this phenomenon. As in the metal oxides, oxygen vacancies exhibit positive charges (Kroger notation $Vo^{\cdot\cdot}$) therefore should be more stable near the cations with less positive charges.

In this work, all calculations were bulk calculations, while in reality, it is easier to form oxygen vacancies at material surfaces or sub-surfaces than in the bulk.

In order to investigate the migration mechanism of TM ions, the transition state theory is adopted in this work, as it has been extensively utilized to describe cation diffusion mechanism in the materials[123]. In $Li_xNi_{1/4}Mn_{7/12}O_2$, both Ni and Mn ions are located originally in the octahedral site in TM layer. An empty tetrahedral site in Li layer is face-sharing with the TM octahedron. The shared-face is composed of three oxygen ions forming a triangular oxygen plane. When the three Li ions near the empty tetrahedral site are extracted, the TM ion may be able to migrate from the octahedral site to the empty tetrahedral site through the shared oxygen plane and then migrate to another octahedral site. If no oxygen vacancies present, the diffusion barriers for TM ions are usually high (0.7~0.8 eV for Ni^{2+}, 2.6 eV for Mn^{4+}, comparable to previous studies[124]), but the barriers can be significantly reduced when oxygen vacancies are introduced. The possible reasons of the large differences between Ni^{2+} and Mn^{4+} diffusion barriers are suspected to be their electronic structure differences as well as the higher charge of Mn^{4+}.

Ni diffusions from initial octahedral sites in TM layer to the nearest tetrahedral sites in Li layer were investigated at three different Li concentrations: $Li_{25/28}Ni_{1/4}Mn_{7/12}O_2$, $Li_{20/28}Ni_{1/4}Mn_{7/12}O_2$ and $Li_{15/28}Ni_{1/4}Mn_{7/12}O_2$ (shown in Figure 5.3). Three different Ni migration pathways are investigated when oxygen vacancies are introduced (shown in Figure 5.4): oxygen vacancy present 1) in the shared oxygen plane between octahedral site and tetrahedral site; 2) in the octahedral vertex but not in the shared oxygen plane; and 3) in the tetrahedral vertex but not in the shared oxygen plane. Although the exact values of Ni diffusion barriers are different for different diffusion paths, the trend is

consistent over all Li concentrations. Therefore only results at $Li_{20/28}Ni_{1/4}Mn_{7/12}O_2$ are discussed below as the representative case. After the introduction of oxygen vacancy, the neighbor Ni will be reduced (Figure 5.5), therefore, the diffusion barrier of Ni^{2+} ions was investigated for a consistent comparison. Figure 5.4 shows the calculated Ni diffusion barriers at $Li_{20/28}Ni_{1/4}Mn_{7/12}O_2$ with oxygen vacancies in different locations mentioned above. It is clear that the locations of oxygen vacancies have significant impact on the Ni diffusion barriers. When Ni diffuses through the shared oxygen plane with vacancy, although the oxygen electron charge density may be less dense, the Ni diffusion barriers are around 1eV, which are slightly higher than the barriers without oxygen vacancies. When Ni migrates from five-coordinated octahedral site, it will be much more unstable in the regular tetrahedral site and Ni diffusion barriers are reduced to as low as 0.2 eV to 0.5 eV. When the vacancy appears at the tetrahedral vertex, which is not in the shared oxygen plane, the three-coordinated tetrahedral site becomes unstable with significant valence change of nearby transition metal ions. In this case, calculated Ni diffusion barrier is a mixing of barriers raised from Ni ion migration and charge transferring between ions, therefore is not included in Figure 5.4. A study on Mn diffusion was also performed at $Li_{20/28}Ni_{1/4}Mn_{7/12}O_2$, and similar observations were obtained (shown in Figure 5.6). With no oxygen vacancies, Mn is much more stable in the octahedral site than in the tetrahedral site, and the barrier is as high as 2.6 eV. However, when oxygen vacancy is introduced in octahedral site but not in the shared plane, the diffusion barrier can be reduced to ~ 0.7 eV. Besides, if oxygen vacancy is introduced in tetrahedral site but not the shared plane, Mn becomes very unstable in the three-coordinated tetrahedral site and will automatically diffuse to nearby octahedral site with no barrier. How oxygen vacancy

would assist TM migration is shown quantitatively for the first time from computations; our findings reveal that during the oxygen vacancy presence both Ni and Mn have the potential to diffuse at room temperature and Ni has lower barrier, while the experimental evidence needs future investigations.

5.4 Conclusions

Combining both STEM/EELS experimental observations and first principles computational studies, we demonstrated that in the Li-excess materials oxygen vacancies are presented in these regions and assisting the TM ion migration through a novel mechanism proposed below: during first cycle charging, after most TM ions are fully oxidized, oxygen ions start to participate in oxidation process (lose electron) and oxygen vacancies would form with formation energy about 0.5-0.6eV. Possibly due to the slow oxygen migration, oxygen vacancies mostly form near the material surfaces and sub-surfaces with 5-6 atomic layers. A significant fraction of the TM ions in these regions therefore are subjected to five (or even less) O-coordinated due to either presences of oxygen vacancies or the broken TM-O bonds on the particle surfaces. TM ions in those five (or less) O-coordinated defect polyhedral sites become much unstable and will spontaneously migrate to the fully-coordinated polyhedral sites nearby in the Li layer. On the other hand, although many of the Li ions are extracted upon charging, stable Li-Li dumbbells are also formed leaving only certain sites in Li layers that are available for TM occupation. Combination of the above two reactions therefore causes the formation of a spinel-like phase from material surface towards the bulk until reaching a region (2~3 nm

beneath surface after first cycle) where oxygen vacancy concentrations are too low to assist the TM ion migration. It was reported that although it might be subjected to further phase change, this TM-ion-migrated region is present for 50 cycles with its thickness unchanged.[32] Our work rationalizes these observations and shed light on the atomic level structure change upon cycling in this class of high energy density cathode materials. The critical role of oxygen ions must be considered for further optimization of this class of materials. Surface coating or doping elements with stronger affinity to oxygen is expected to reduce the phase transformation.

Chapter 5, in full, is a reprint of the material "Uncovering the roles of oxygen vacancies in cation migration in lithium excess layered oxides", Phys. Chem. Chem. Phys., 2014, 16, 14665. The dissertation author was the primary investigator and author of the paper.

Figures:

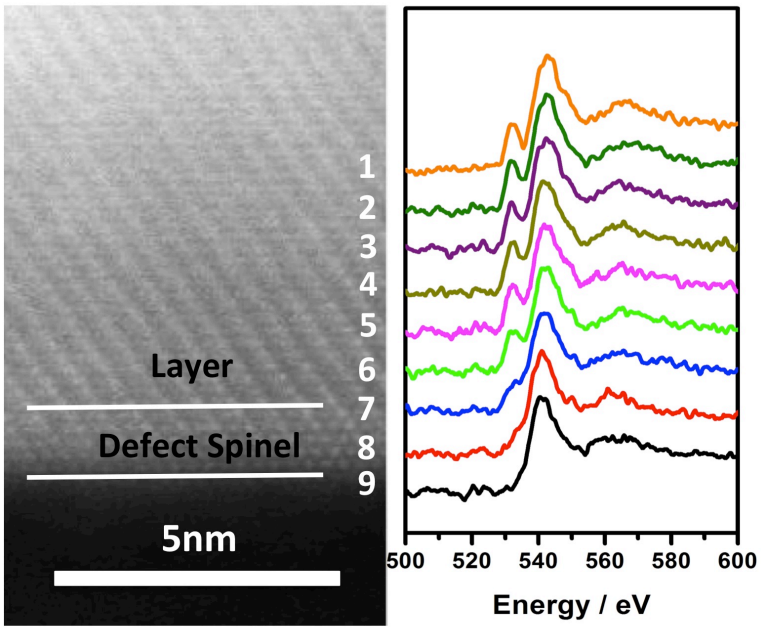

Figure 5.1: Spatial resolved O K-edge EELS spectra from bulk to surface.

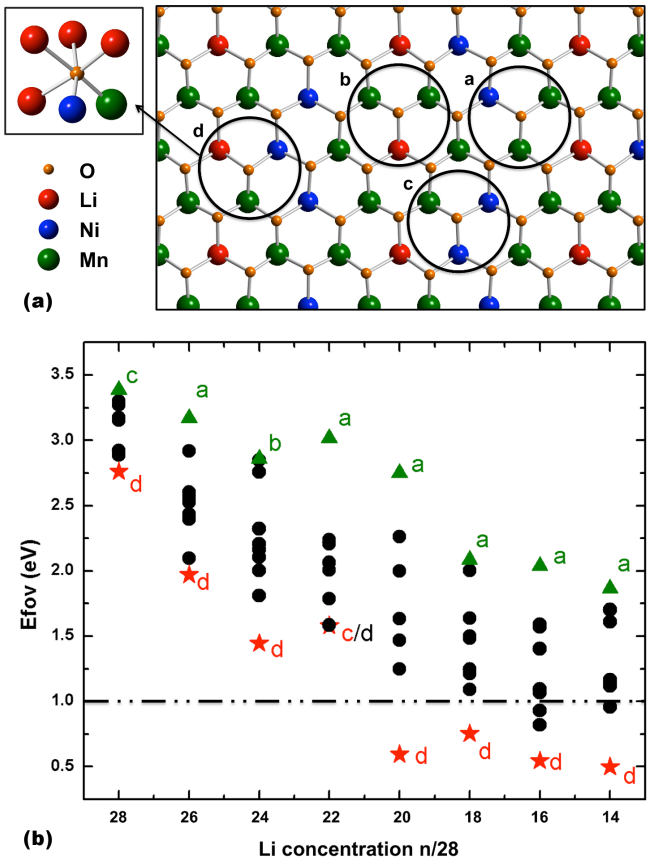

Figure 5.2: (a) Atomic configurations of $Li[Li_{1/6}Ni_{1/4}Mn_{7/12}]O_2$; (b) Oxygen vacancy formation energy vs. Li concentration

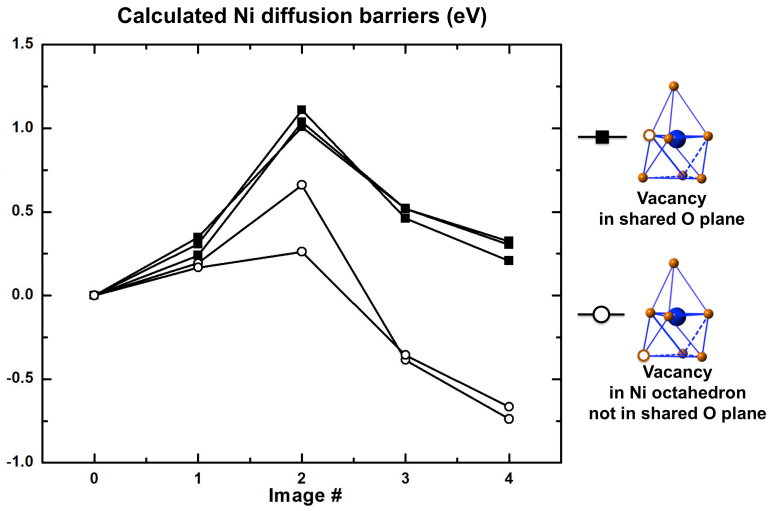

Figure 5.3: Ni diffusion barriers with oxygen vacancies in different positions at $Li_{15/28}Ni_{1/4}Mn_{7/12}O_2$

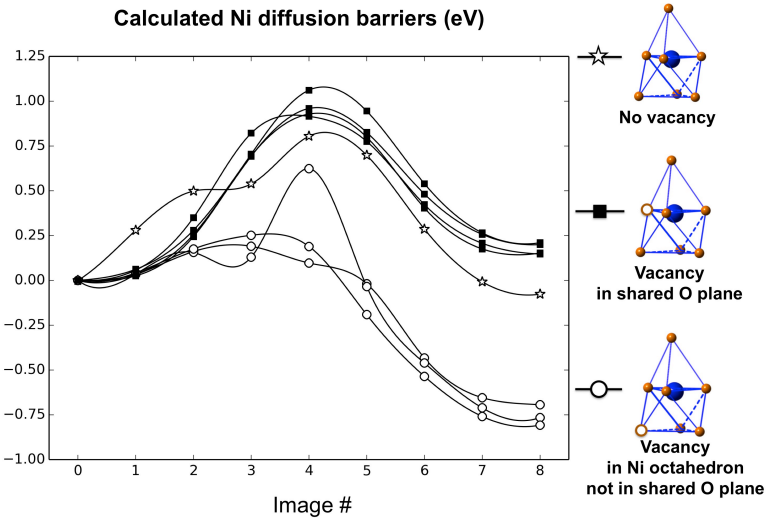

Figure 5.4: Calculated Ni diffusion barriers with oxygen vacancies in different positions at $Li_{20/28}Ni_{1/4}Mn_{7/12}O_2$ (Vacancy in tetrahedron but not in the shared plane unstable)

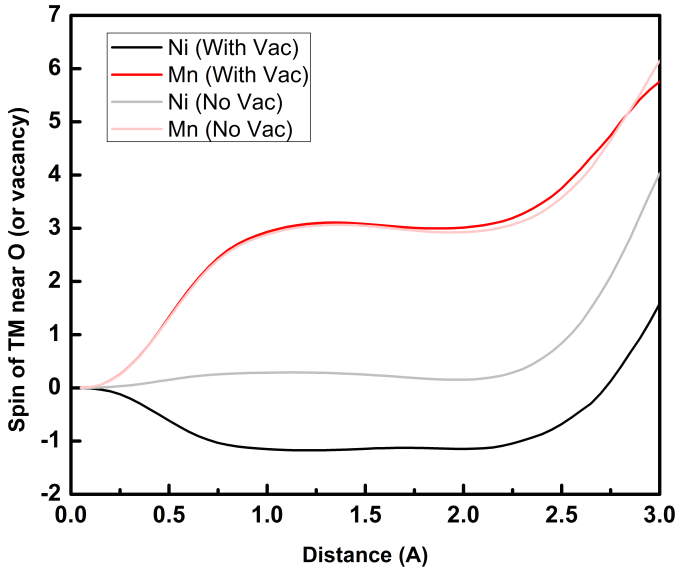

Figure 5.5: Neighboring TM valence change after introduction of oxygen vacancy at $Li_{20/28}Ni_{1/4}Mn_{7/12}O_2$

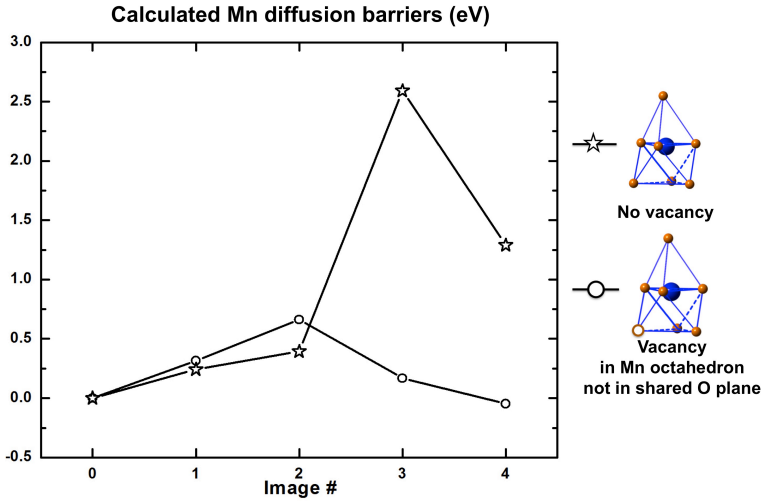

Figure 5.6: Mn diffusion barriers with oxygen vacancies in different positions at $Li_{20/28}Ni_{1/4}Mn_{7/12}O_2$

6 SURFACE COATING ON CATHODE MATERIALS IN LIB

6.1 Lithium lanthanum titanium oxides: a fast ionic conductive coating for lithium-ion battery cathodes

6.1.1 Introduction

Lithium Lanthanum Titanate (LLTO) is one of the fastest lithium ion conductors to date. $Li_{3x}La_{(2/3)-x}\square_{(1/3)-2x}TiO_3$ adopts the perovskite structure ABO_3 with A=Li, La and B=Ti. [125-130] This series of materials are considered to have fast lithium transportation and the bulk ionic conductivity can be achieved as high as 1×10^{-3} Scm^{-1} at room temperature when x=0.11. [131,132] Applying this material as the solid electrolyte in all-solid Li-ion battery is under intensive studies. [133-135]

At present, the electrolyte of secondary lithium ion batteries in the market is mainly based on $LiPF_6$ salt dissolved in an organic solvent (such as ethylene carbonate). Electrolyte needs to be a fast Li ion conductor, but an electron insulator. A major concern about the liquid electrolyte is the safety issue, including poor thermal stability and low resistance to leakage. In addition, conventional electrolyte has narrow voltage window, decomposition would happen at both extremely low and high voltage ranges causing electrode/electrolyte parasitic reactions. Upon cycling, the electrolyte would get consumed and the cell eventually fails. Solid electrolyte can mitigate these problems but to have fabricate a continuous layer of solid electrolyte layer at large dimensions remains a major challenges. In this study, we are applying solid electrolyte as a coating material for cathode in lithium ion batteries to resolve the current issues in the second-generation layered transition metal oxide materials, such as $LiNi_{0.8}Co_{0.15}Al_{0.05}O_2$ (NCA).

The current problems (fading capacity and poor cyclability etc.) present in pristine NCA layered cathode material have been attributed to the dissolution of the cation into the electrolyte, as well as the surface layer-to-spinel phase transformation happening in most layered materials. [112] Coatings such as AlF_3, ZrO_2, Al_2O_3 etc. have been studied intensively to improve the performance. Suppression of the phase transitions, increases in the structural stabilities, as well as decreases in the disorder of cations in the crystal sites have been observed. However the surface modification mechanism still remains open for different coating materials. Furthermore, few studies have been reported on the characterization of continuous effect of coating upon cycling.

In this study, first principles calculations were performed to explore the lithium diffusion pathways and calculate the lithium diffusion activation barriers in $Li_{3x}La_{(2/3)-x}\square_{(1/3)-2x}TiO_3$ when $3x = 0.125$ and 0.35. To study the effect of LLTO as a coating for cathodes, the LLTO coating has been applied to $LiNi_{0.8}Co_{0.15}Al_{0.05}O_2$ (NCA). We show significantly improved electrochemical performances of the coated samples. To systematically study the mechanism of a solid electrolyte as a coating material to cathode, scanning electron microscope (SEM), energy dispersive spectroscopy (EDS), X-ray diffraction (XRD), transmission electron microscope (TEM) combined with electrochemical property measurements including PITT and EIS were carried out on both the pristine NCA sample and LLTO coated sample. Scanning transmission electron microscope with electron energy loss spectroscopy (STEM_EELS) mapping was collected on coated sample before and after cycling.

6.1.2 Methodologies

6.1.2.1 Computational Methodology

In this work, two models of $Li_{3x}La_{(2/3)-x}\square_{(1/3)-2x}TiO_3$ are created with low lithium concentration(x=1/24) and high lithium concentration (x=7/60). For low-lithium-concentration LLTO, the atomic models and notations are adopted from previous work done by Catti. [136,137] The supercell is composed of eight formula units of $Li_{0.125}La_{0.625}TiO_3$. For high lithium concentration LLTO, an original model is proposed in this study with twenty formula units of $Li_{0.35}La_{0.55}TiO_3$. First principles calculations were performed in the spin-polarized GGA+U approximation to the Density Functional Theory (DFT). Core electron states were represented by the projector augmented-wave method[73] as implemented in the Vienna ab initio simulation package (VASP). [74,75] The Perdew Burke Ernzerhof correlation [74] and a plane wave representation for the wavefunction with a cutoff energy of 420eV were used. The Brillouin zone was sampled with a mesh including gamma point. The density of the k-point mesh for all calculations is approximately one point per 0.01 $Å^{-3}$.The atomic positions and cell parameters were fully relaxed to obtain total energy and optimized cell structure. Effective U value is applied in the Liechtenstein approach with exchange energy J = 1.0eV. [76,138] U_{eff} = 7.5eV is applied to the La 4f states to correct their position relative to La 5d levels. [139] It is reported that the experimentally observed position of 4f bands can be reproduced within this approach. [140] The Nudged Elastic Band (NEB) method is used to find the minimum energy path and the energy barrier for Li diffusion in LLTO. [141]

6.1.2.2 Experimental Methodology

Materials: All the samples, NCA pristine sample with particle size of around 100nm, together with 1wt%, 2wt% and 5wt% LLTO coated NCA samples (named as LLT1, LLT2 and LLT5, respectively), are synthesized by the company CheMat Technology.

Materials Characterization: The particle morphology and size distribution of the synthesized powders were determined using an FEI XL30UHR SEM (ultra high resolution SEM) with a Sirion column, which enables very high resolution imaging at low kV. All images were collected under an accelerating voltage of 10kV. The powders were suspended on a double-sided carbon tape placed on a specimen holder.

EDS was taken using a Phillips XL30 field-emission environmental high resolution SEM with an Oxford EDS attachment.

XRD spectra were taken using a Bruker D8 advance diffractometer with a Bragg Brentano theta-2theta geometry and a Cu Kα source. Samples were scanned from 10° to 80° with a scan rate of 0.025° per second.

TEM images were collected using an FEI Tecnai G2 Sphera cryo-electron microscope with an operation voltage of 200kV. The powders were suspended on a 300mesh copper grid with lacey carbon.

STEM-EELS data was collected using a Cs-corrected FEI Titan 80/300-kV TEM/STEM microscope equipped with a Gatan Image Filter Quantum-865. All STEM images were acquired at 300kV. EELS spectra shown in this work were acquired with a convergence angle of 30mrad.

6.1.2.3 Electrochemical Characterization

Cathodes were prepared by mixing 80 wt % pristine and coating powder with 10 wt % acetylene carbon black (99.9%) and 10 wt % poly (vinylidene fluoride) in *N*-methyl pyrrolidone solution. The slurry was cast onto Al foil using a doctor blade and dried overnight in a vacuum oven at 80°C. The electrode disks were punched and dried again at 80°C for 6h before storing them in an argon- filled glove box (H_2O level of <1 ppm). 2016 type coin cells were used to study the electrochemical behavior of the compounds. Lithium metal ribbon and 1 M $LiPF_6$ in a 1:1 EC: DMC solutions were used as anode and electrolyte, respectively. A Celgard model C480 separator (Celgard Inc.) was used as the separator. The coin cells were assembled in the same argon-filled glove box and tested on an Arbin battery cycler in galvanostatic mode. The cycling tests were conducted between 2.5V and 4.2V and the rate tests were in the window of 2.0V-4.4V.

The PITT experiments were carried out by applying potential steps of 10 mV and measuring the current as a function of time for the first charge. The potential step was advanced to the next level when the measured current fell below the threshold limit of 10 μA, corresponding to a C/200 rate. The voltage window was set at 3.45-4.2 V.

Solartron 1287 system coupled with a Solartron 1260 frequency response analyzer was used for the EIS measurement. The EIS test was carried out using the three-electrode cell. For the reference electrode, the end tip of the Teflon-coated Cu wire (ϕ(Teflon) $=4.5\times10^{-4}$ m; ϕ(Cu) $=1.27\times10^{-4}$ m) was removed and placed between two separators. Details on cell configuration can be found elsewhere. [142,143] Before the electrochemical experiments, elemental Li was cathodically coated on the bare Cu wire by having Li metal as a counter

electrode. The as-prepared cell was charged to and equilibrated at 4.2 V at a rate of C/10. The impedance spectra were obtained in the frequency range of 100 kHz to 100 mHz.

6.1.3 Results

6.1.3.1 Computational Results

6.1.3.1.1 Low lithium concentration scenario

The atomic structure of $Li_{0.125}La_{0.625}TiO_3$ is shown in Figure 6.1(a). For low-lithium-concentration LLTO, the atomic models and notations are adopted from previous work done by Catti et. al. [136,137] The supercell is composed of $2a_p \times 2a_p \times 2a_p$, where a_p is the conventional cubic lattice of ABO_3 perovskite structure (38 atoms in total). La ions are located in A sites and Ti ions in B sites. Li ions are also located in A sites as initialization. Along (001) direction, four A-site ions in (001) plane can be grouped as a 2D cell. A La-rich layer (z=1/4) is composed of 4 La ions (4La) and a La-poor layer (z=3/4) composed of 1 La ion, 1 Li ion and 2 vacancies (1La+1Li+2□) (shown in Figure 6.1(b)). This La-rich and La-poor layers are alternatively arranged according to the experimental observations. [144] The after relaxation structure of z=3/4 plane is shown in Figure 6.1(c). After structural relaxation, the cubic lattice is distorted to an orthorhombic lattice where a=7.828Å, b=7.754Å, c=7.871Å. La and Ti ions are still in A and B sites respectively, while Li ions move closely to the center vertical oxygen square planar window as shown in Figure 6.2(b) and (c). These results are consistent with the previous work. [137] These sites are referred as Li equilibrium sites in this work. Figure 6.2(a) shows all the Li equilibrium sites in the 2D La-poor layer. These equilibrium sites are used as

the end-points of the NEB calculations and the corresponding energies are used as the references when calculating Li diffusion activation barriers. Based on the NEB calculation results, when Li ions diffuse between two equilibrium sites, they prefer a curved diffusion path that avoids the empty A sites (Figure 6.3(a)). The crosses in Figure 6.2(a) are the saddle points in the calculated minimum energy paths for Li diffusion. The obtained energy barriers are 230meV (from Li1 to Li2) and 22meV (from Li2 to Li3), which is much lower than the previous values reported by Catti et al.[137]. The discrepancy may be from the following possible reasons: firstly, our predicted pathway is different, which was obtained by NEB method instead of the "Frozen Ion" method adopted by previous work. NEB has been proved to be pretty reliable on predicting the pathways and finding minimum energy path on the potential energy surface. Secondly, different DFT functionals were used. However, we believe the U correction is not playing a role. Besides the data showed in this work, we have also calculated the pathway and diffusion barriers without U correction, which gives us consistent results.

6.1.3.1.2 High lithium concentration scenario

The same method used in calculations of the low lithium concentration model is adopted for the high lithium concentration scenario $Li_{0.35}La_{0.55}TiO_3$. In all cases, space group P1 is used to reduce the symmetry constrains to a minimum. It is a supercell composed of $\sqrt{5}a_p \times \sqrt{5}a_p \times 4a_p$. The 2D cell in (001) plane is composed of five A-sites occupied by Li, La or vacancies. Three different models are established with different in-plane cation arrangements and the layer stacking sequences. Similar to the low lithium concentration model, La-rich and La-poor layers are alternatively arranged; in addition, because of La ion's large radii and its strong interactions with Li ions, the principle of as

less La in the Li layer as possible is adopted in this model. The calculated energies are listed in Table 6.1. Due to the structure complexity, our investigations are focused on the La-poor layer (z=1/8, 4Li + 1 □) of model I, which is the lowest in energy among the proposed models, drawn in Figure 6.1(d). This model can be rationalized that by having the least number of La in the La-poor layer helps reducing the repulsion forces and results in the lowest energy. The corresponding 2D cell of the La poor layer (z=1/8) is shown in Figure 1(e) and the structure of this layer after relaxation is depicted in Figure 6.1(f). After structural relaxation, Li equilibrium sites are also close to the center of vertical oxygen square window, similar to the results obtained in the low lithium concentration scenario. NEB calculations are performed to find the diffusion paths and energy barrier for the circled Li. A similar curved diffusion path can be found as shown in Figure 6.3(b). The minimum energy path avoids both the empty A-site and the three other Li ions. The highest activation barrier for this diffusion path is around 390meV, and there also are barriers in other local environments around 120meV within this path.

6.1.3.2 Experimental Results

6.1.3.2.1 Materials Characterization: SEM/EDS, XRD and TEM

The morphology of pristine and LLTO coated powders were examined by scanning electron microscopy (SEM) (Figure 6.4(a-d)). The pristine particles have a very uniform size distribution of around 100 nm. The primary particle size after the LLTO coating is slightly increased ranging between 100-200 nm. It is hypothesized that some sintering of primary particles may have occurred during the LLTO coating process, as

can be seen in the SEM images. From Figure 6.5 (a), the XRD data of pristine, 1wt% LLTO coated (LLT1), 2wt% LLTO coated (LLT2) and 5wt% LLTO coated (LLT5) samples shows that the main peaks are representative of the layered structure $LiNi_{0.8}Co_{0.15}Al_{0.05}O_2$ with the $R\bar{3}m$ symmetry group; in addition, the existence of doublets at (006)/(102) and (108)/(110) indicates the well-layered structure with little Li/Ni interlayer mixing. In Figure 6.5 (b) and (c), the most intense peaks are associated with the LLTO phase [145] of 2θ=24.6°, 31.6°, 33.6° and appear for all three coated samples. All three peaks, however, shifted to a lower angle as compared to the published data on the bulk of LLTO, [145] which indicates larger interplane distances in the LLTO coating. Figure 6.4(e-g) show respectively the EDS results of pristine, LLT1 and LLT5, which represents that the amount of La and Ti elements increases with the coating weight percentage.

To further investigate the surface morphology of pristine and coated materials, TEM images were taken. The surface coating is mostly like small islands distributed on the surface of pristine material (inset in Fig 6.4(c), the while spots indicates the coating material). In addition, some particles were coated uniformly. The inset in Figure 6.4(d) depicts clearly the interface between the core material and the coating material.

6.1.3.2.2 Electrochemical property test

The electrochemical property testing of the pristine and coated electrodes were performed to examine the coating effect on cyclic performance, and rate capability. Figure 6.6(a) displays the discharge capacity retention with cut-off voltage 4.4V. As shown in the figure, materials with LLTO coating (1wt%, 2wt%, 5wt%) maintained at least 99% capacity (compared to 1st discharge) after ten cycles, while the pristine material

only retained around 85% of 1st cycle discharge capacity after ten cycles. In this work, LLT1 was adopted as the representative sample for further in-depth investigation on the role of the LLTO coating material on the NCA electrodes.

Figure 6.6(b) and (c) show the rate testing data for pristine and LLT1 electrodes at the rate of C/20 for charging and C/20, C/10, C/5, C/2, 1C, 2C for discharging, in the voltage range of 4.4-2.0V. All the cells for rate testing are with a loading density of around 5mg/cm^2. As can be seen from the graph, the capacity at C/20 has been improved from around 125mAh/g to 135mAh/g; the improvement of the coated samples is most obvious at higher rates of C/2, 1C and 2C. For C/2, 1C and 2C, the capacities for the pristine electrode are 82mAh/g, 68mAh/g, and 44mAh/g, respectively. On the other hand, the LLT1 electrode shows much higher capacity, 105mAh/g, 93mAh/g, and 82mAh/g. In addition, the OCV drop for the pristine material at the beginning of each discharge is more severe at the higher rates. In the case of the 2C rate, the cell voltage of the pristine electrode drops to 3.45V, while the LLT1 electrode remains at 4.0V.

In order to further identify the reasons for the improved rate capability of the LLT1 electrode, a PITT test was performed, and Li chemical diffusion coefficients in both pristine and LLT1 coated electrodes are extracted. The results were obtained from a step size of 10mV and current limit corresponding to a C/200 rate. The linearity of ln (I) vs. t is good enough for the analysis shown below. A semi-logarithmic plot of the current vs. time was extracted based on the long-time dependence, $\tau >> L^2/\widetilde{D}_{Li}$. The lithium diffusion can be solved with Fick's law for a semi-infinite system with a perturbation of the surface concentration in Eq. 1 [146]

$$I(t) = \frac{2Fa\ (C_s - C_0)\widetilde{D}}{L} \exp(-\frac{\pi^2 \widetilde{D}}{4L^2} t)$$

The lithium chemical diffusion coefficient was obtained from the slope of the linearity of ln (*I*) vs. t in Eq. 2

$$\widetilde{D} = -\frac{dln(I)}{dt} \cdot \frac{4L^2}{\pi^2}$$

Figure 6.7 (a) plots the calculated lithium diffusion coefficient ($\widetilde{D}_{LiLi}$) vs. the state of charge. The LLTO coating increases the chemical lithium diffusion coefficient by almost one order of magnitude at any state of charge (except for the voltage 3.7-3.8V) compared to that of the pristine electrode. Another interesting fact is that the valley of the diffusion coefficient profile moves from 3.65V for the pristine electrode to 3.75V for the LLT1 electrode. The valley in the diffusion coefficient plot is generally representative of a two-phase reaction, the value of which is usually two to three magnitudes of orders lower than the diffusion coefficient in the single-phase region. [37] There has also been a study on the two-phase reaction during the first charge of this material; and the valley is associated with the fact that another hexagonal phase would appear and coexist with the original hexagonal phase. [38] In general, the LLTO coating layer delays the occurrence of a two-phase reaction by 0.1V.

EIS measurements were carried out to study the effects of the LLTO coating on the interfacial characteristics between the electrolyte and the active materials. Figures 6.7 (b) and (c) exhibit the impedance spectra of the active materials from the three-electrode cell configuration at a cell potential of 4.2V. The impedance spectra consist of two semicircles in the high and intermediate frequency range and a line inclined in the low frequency. The two semicircles at the high and intermediate frequency are attributed to

Li^+ ion transport through the SEI and interfacial charge-transfer reaction combined with electrochemical double-layer capacitive behavior, respectively. The latter inclined line is responsible for the solid-state lithium diffusion into the active material. For the quantitative analysis, the simplified equivalent circuits presented in the insets of Figure 6.7 (b) and (c) were used. The values of all electrical parameters were taken from the CNLS (Complex non-linear least square) fitting method to the equivalent circuits, as summarized in Table 6.1.

As listed in Table 6.1, all reaction resistances in LLT1 electrode have relatively smaller numbers than those in the pristine electrode. The resistances of SEI films, R_f, interfacial charge transfer reactions, R_{ct}, and Warburg coefficient A_w which is due to the solid-state lithium diffusion in the active material, decreased by 64%, 84%, and 52%, respectively. This indicates that every elementary reaction step at the interface is considerably improved by the LLTO coating layer. In the very low-frequency (<10mHz), however, the impedance behavior of LLT1 electrode is found to be different from that of the pristine electrode. (The data are not presented in this work.) The LLT1 impedance spectra have an additional semicircle at very low frequency. One possibility is that another charge transfer reaction happens at the interface between LLTO coating and the NCA active material since there is a change in the local structures from LLTO to NCA. [147] Further investigation will be carried out to identify the charge transfer mechanism.

6.1.3.2.3 STEM_EELS mapping results

STEM images as well as EELS mapping were performed to examine the existence of coating before and after cycling. The RGB composite mapping is depicted in Figure

6.8. Signals for Ti and La elements can be clearly seen from the EELS map. It indicates that the coating will not get detached from the surface during cycling therefore has a lasting effect after cycling.

6.1.4 Discussions

In this study, first principles calculations are performed to characterize LLTO, one of the solid electrolyte candidates, fast lithium ion conductors. The fast lithium conductivity is supported by our first principles calculation results. In the low lithium concentration scenario, even the highest activation barrier of Li in-plane diffusion is as low as 230 meV, which is much lower than the typical calculated Li diffusion barriers in layered compounds such as NCA. [148] For the high lithium concentration scenario, the highest barrier is around 390 meV. Such discrepancy between the two models, however, is probably caused by the different numbers of vacancies in the same plane for the migrating Li ion. In our calculations, due to the size limitation of the model supercells, the barriers in the high lithium concentration model were calculated with only one vacancy adjacent to the migrating Li ion, while in low lithium concentration model, two vacancies were located besides the migrating Li ion. As suggested by previous study, the rate of non-perfect crystals is very sensitive to the density of discrete vacancy sources. [43] Moreover, note that the relatively high diffusion barrier is reached only in a specific local environment, and barriers in other local environments can be as low as 22meV. Since all computations are performed at 0K, Li, La ions and vacancies are arranged in a highly

ordered way. At room temperature, such site ordering is much reduced and the overall lithium diffusion activation energies should be lowered.[144]

This solid electrolyte candidate, LLTO, has been applied as a coating material to our NCA cathode material in lithium ion half-cells. SEM, EDS, TEM and XRD results consistently suggest that the coating material LLTO exists on the surface of the NCA material and it is crystalline in nature. Nevertheless, the shift of the XRD peaks for our samples of LLTO indicates larger interplane distances and therefore possible local structure change of the perovskite LLTO.

As shown in Figure 6.6(a), the cycling performances of coated samples are significantly improved, which is consistent with previous study on a different layered oxide.[149] Such improvement is generally attributed to the surface protection of the coating. For high voltage cathode materials such as NCA, the high operating voltage may cause the decomposition of the $LiPF_6$ salt, generating HF in the electrolyte. For uncoated samples, the electrode surface is in directly contact with the electrolyte, thus the active materials might be dissolved into the electrolyte due to the HF etching.[150,151] Meanwhile, the electrode surface which is unstable at high voltage undergoes structural reconstruction and forms a spinel-like phase near the surface. This phenomenon is suggested by the large OCV drop at the beginning of each discharge for the uncoated sample in this study. The LLTO coating existed on the electrode surface prevents the NCA materials from direct contact with the electrolyte, therefore can largely reduce the dissolution of active materials and suppress the surface structural change at high voltage. The capacity retention of the LLTO coated samples is significantly improved as a result.

Besides the cycling performance, the rate capability of coated sample is also enhanced as indicated in Figure 6.6 (b) and (c). The high ionic conductivity of the LLTO coating materials is regarded as a key factor affecting the rate performance. Although the introduction of a coating layer creates another interface between the active material and the coating material, which may add an extra resistance to Li transportation, it is compensated by the fast lithium transportation inside the coating layer and the suppression of SEI formation. The overall impedance therefore is reduced significantly in the coated sample. As obtained from PITT results, the Li chemical diffusion coefficient in LLTO coated sample is one order of magnitude higher than that of the uncoated sample. The EIS results also show that the SEI layer impedance of the coated sample is much lower. For the LLT1 sample, the impedance for Li^+ diffusion in the SEI layer is even lowered by more than 60%. These observations suggest that the enhancement of the solid-state lithium diffusion caused by the LLTO coating should be an important contribution factor to the improved rate capability. This kinetic process may be an explanation for the delay of two-phase (the valley) in PITT results. Furthermore, the whole impedance for the active material is reduced for LLTO coated electrode compared to the pristine electrode; this may be another reason for the higher voltage where two-phase reaction occurs.

Lastly, we note that the coating material would not decompose or detach from the NCA active material after cycling (cut-off voltage 4.2V) by STEM/EELS. It indicates that the coating has a lasting effect. A further study of LLTO coating will be carried out on other high voltage cathode materials, such as high voltage cathodes (cut off voltage

4.6-4.8V), to see whether the LLTO coating will continue to play a role in other higher voltage systems.

6.1.5 Conclusions

In summary, we demonstrated the significant improvement on rate capabilities and capacity retention on layered cathode material NCA by applying a fast ionic conduction solid electrolyte coating. We elucidate the mechanism of the solid electrolyte LLTO coating with a joint study of experiment and computation. LLTO has *intrinsically high* ionic conductivity. Therefore, besides acting as a protective coating layer, it reduces the impedance of Li^+ diffusion in the composite electrode, as well as the impedances of interfacial charge transfer and transportation through the SEI layer. In addition, the coating layer is relatively stable after cycling resulting in a continuous effect upon cycling. Our findings shed some new light on applying solid electrolyte as coating in high voltage cathode materials and understanding the mechanism of coating in lithium ion batteries. The stability of the LLTO coating material upon longer cycling, higher voltage exposure (> 4.5V) and higher temperature exposure, remains to be examined.

6.2 AlF_3 coating for lithium-ion battery cathodes

6.2.1 Introduction

The common idea of surface modification is to reduce potential side reactions, such as HF etching and the formation of undesirable products within the solid-electrolyte

interface film (SEI), between electrode and electrolyte at high working voltage[152]. Based upon published works during the past few years, there are several different surface modification strategies applied to Li-excess. The most widely used surface modification materials are oxides, fluorides, and phosphates, for example, TiO_2, Al_2O_3, AlF_3, and $AlPO_4$; [153-155] however, most of these materials are electron and ion insulators. Learning from the case of $LiFePO_4$, carbon and Al has been used as a coating layer on Li-excess, in order to improve the electronic conductivity of the material.[156,157] Other researchers have introduced an ionic conductor to the surface of Li-excess, such as, lithium phosphorus oxynitride (LiPON), $LiNiPO_4$, and Li_3VO_4.[158-161] Manthiram et al. combined the advantages of different surface modifications and developed hybrid strategies. One of their recent works combined reduced graphene oxide and $AlPO_4$, which largely suppressed undesired SEI formation.[162] In contrast to the studies mentioned above, Thackeray et. al. showed a slightly mild acid treatment will also reduce the first cycle irreversible capacity loss of Li-excess layered oxides.[163]

Although these surface modifcations improved the electrochemical performance of Li-excess, the fundemental role in terms of their chemical and structural effects, are still not well understood. In this work, we prepared Li-excess layered oxide with composition of $Li_{1.2}Ni_{0.2}Mn_{0.6}O_2$ (LNMO) through a routine hydroxide co-precipitation method. A mild acid NH_4F and metal precipitant Al^{3+} were used together to modify the surface of Li-excess. By synthesizing an Al_2O_3 surface coating via incorporation of NH_4F, the electrochemical performance of Li-excess was markedly improved. Aberration corrected transmission electron microscopy (a-STEM) / electron energy loss spectroscopy (EELS) was carried out to investigate the chemical and structural changes

after surface co-modification, enabling us to explain how the NH_4F and Al_2O_3 surface co-modification improved the initial coulombic efficiency, rate capability, and cycling stability of Li-excess. These findings will guide us in designing reasonable surface modifications in the future.

6.2.2 Methodologies

6.2.2.1 TEM

TEM images were collected using an FEI Tecnai G2 Polara cryoelectron microscope with a field emission gun and a voltage of 300 kV. The powders were suspended on a 300-mesh copper grid with lacey carbon.

6.2.2.2 *a*-STEM/EELS

Electron microscopy work was carried out on a Cs corrected FEI Titan 80/300-kV TEM/STEM microscope equipped with a Gatan Image Filter Quantum-865. All STEM images and EELS spectra were acquired at 300 KV and with a beam size of ~0.7 Å. EELS spectra shown in this work were acquired from a square area of ~0.5 ×0.5 nm using an acquisition time of 2 s and a collection angle of 35 mrad. High angle annular dark field (HAADF) images were obtained at a convergence angle of 30 mrad and a large inner collection angle of 65 mrad. Images acquired by an HAADF detector with a small convergence angle and a relatively large inner collection angle are also called "Z-contrast" images, where the contrast is proportional to $Z^{1.7}$.[114,115] Atomic resolution Z-contrast images can be used to differentiate elements and provide atomic−structural information based on the contrast of the atomic columns.

To minimize possible electron beam irradiation effects, EELS and HAADF figures presented in this work were acquired from areas without pre-beam irradiation. Mn L_3 to L_2 intensity ratio analysis was performed using the method described by Wang et al.[95]

6.2.3 Results and Discussions

High-resolution transmission electron microscopy was used to identify the Al_2O_3 coating on surface modified material. Figure 6.9 a and b are the HRTEM images of pristine (LNMO) and treated (NALNMO), respectively. The TEM images of both materials show very good layered crystal structure. Amorphous films are observed on the surface of NALNMO, while the LNMO shows a very clean surface. More than 20 particles were analyzed to examine the amorphous film. As shown in Figure 6.9 b, this amorphous film is unevenly coated on the surface, with thickness ranging from 0 nm to 2.5 nm. As our recent study indicates, the surface chemistry of LNMO varies with different preparation methods.[164] We apply the same NH_4F and Al_2O_3 surface co-modification on LNMO prepared by carbonate method, which forms uniform Al_2O_3 coating with a thickness of 1 nm as showed. In addition to the amorphous coating, there are small islands sitting on the surface of particles, as illustrated in Figure 6.9 c, which are not observed in our pristine $Li_{1.2}Ni_{0.2}Mn_{0.6}O_2$. Figure 6.9 d depicts the TEM image of these small islands at higher magnification. The island exhibits a well-layered crystal structure and particle size around 20 nm. EELS was performed on the islands to verify that it is active material instead of Al-related compounds.

Figure 6.10 depicts the differences between the bulk and surface structure of NALNMO. Multiple grains were selected for study and the results were consistent;

therefore, only representative data are shown here. The diffraction pattern of the FFT represented by the blue squared region at the surface with a "spinel-like" structure compared to the red-squared region in the bulk. After NH_4F and Al_2O_3 surface co-modification, there is a 3 nm “spinel-like” phase on the bulk, layered phase.

In addition to direct visualization of the crystal structure changes, EELS was carried out to obtain chemical information. Two representative particles were observed and studied. One is the R-3m (-101) zone axis particle as the inset electron diffraction pattern of Figure 6.11 a showed, the other is R-3m (010) zone axis particle which is presented in Figure 6.11 d. EELS was performed on NALNMO from bulk to surface, with step size of ~1 nm, as showed in Figure 6.11 a and d. The L_3 and L_2 edges of transition metals are due to the electronic excitation from the $2p^{3/2}$ to $3d^{3/2}$ and $3d^{5/2}$ orbitals and from the $2p^{1/2}$ to $3d^{3/2}$ orbital, respectively. Previous studies have shown that the L_3/L_2 ratio is sensitive to the valence state of Mn.[165,166] The L_3/L_2 ratio plotted as a function of distance from surface to bulk in Figure 6.11 b and e. The L_3/L_2 edge ratios of both particles reveal that the Mn valence remains 4+ in the bulk, as it does in pristine LNMO[167]. However, the (-101) zone axis particle (Figure 6.11 d) shows Mn valence reduced to 3+ within a 3 nm region of the surface. The corresponding O K-edge of bulk and surface are plotted in red and purple, respectively. The pre-peak in O K-edge is due to the transition of 1s electrons to the unoccupied 2p orbitals, which hybridize with the TM 3d orbitals. The decrease in the pre-peak in the (-101) zone axis particle agrees with the reduction of Mn at the surface.[168]

6.2.4 Conclusions

The use of a-STEM/ EELS enabled us to understand the structural and chemical aspects of the materials studied from both bulk and surface perspectives. The complex changes on the material's surface after NH_4F and Al_2O_3 surface co-modification included the formation of "spinel-like" phase, the etched island active material, an amorphous Al_2O_3 coating, and the reduction of surface Mn. After the modification, the first cycle coulombic efficiency, the rate capacity and cycling capacity was improved. These understandings will guide us in designing better cathode materials for lithium ion batteries of the future.

Chapter 6, Part 1, in full, is a reprint of the material "Lithium lanthanum titanium oxides: a fast ionic conductive coating for lithium-ion battery cathodes", Chemistry of Materials, 2012, 24(14), 2744, by Danna Qian, B. Xu, H. -M. Cho, T. Hatsukade, K. J. Carroll, Y. S. Meng, Copyright (2012) American Chemical Society. The dissertation author is the primary investigator and author of the material. Part2, in part, is a reprint of the material "Understanding the role of NH_4^+ and Al_2O_3 surface co-modification on lithium-excess layered oxide $Li_{1.2}Ni_{0.2}Mn_{0.6}O_2$" submitted. The dissertation author is the primary investigator and author.

Figures:

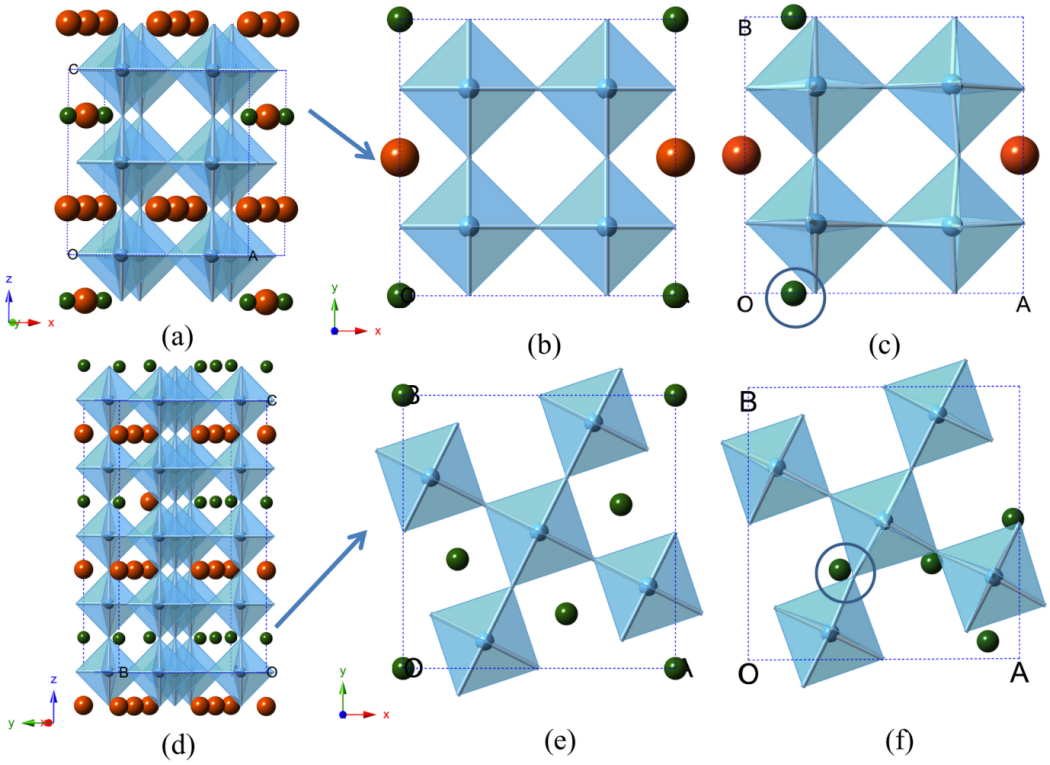

Figure 6.1: Computational model structure of $Li_{0.125}La_{0.625}TiO_3$(a) and $Li_{0.35}La_{0.55}TiO_3$ (d). Planes of interest used in NEB calculation of low lithium concentration (b) and high lithium concentration (e). (c) and (f) are the after relaxation structure of planes in (b) and (e) respectively.

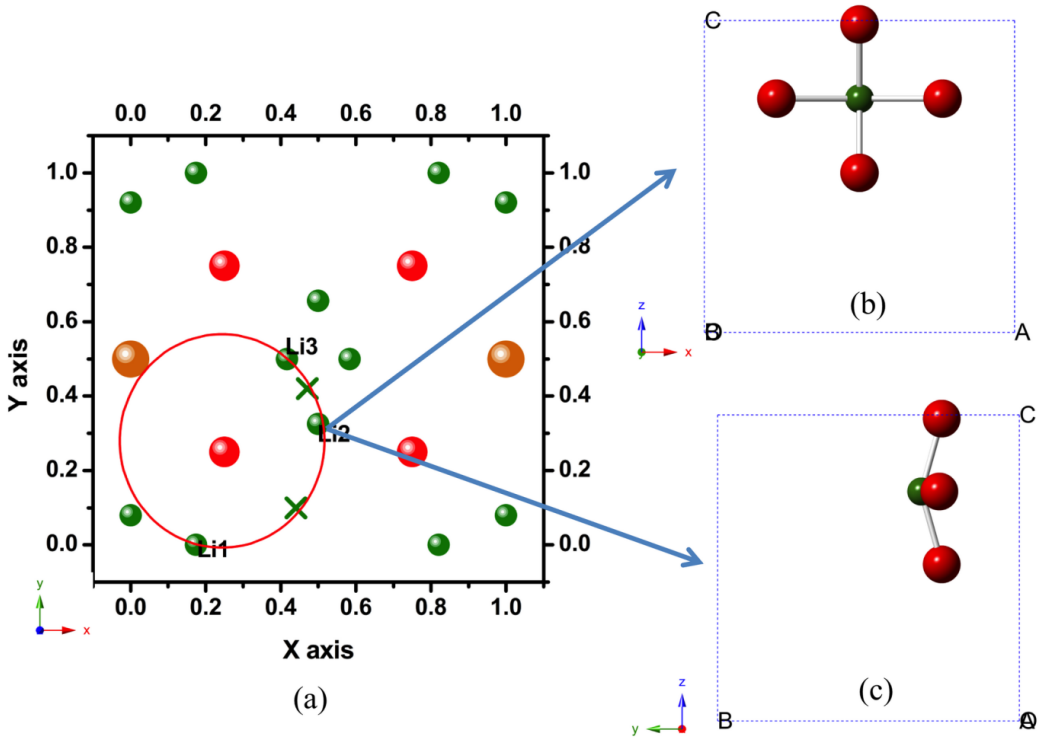

Figure 6.2: (a) x=3/4 plane of low lithium concentration with all equilibrium states and middle images. Two crosses are the images between Li1 and Li2, Li2 and Li3 respectively. (Other images can get from symmetry). (b) (c) Illustration of vertical oxygen square window from different view directions.

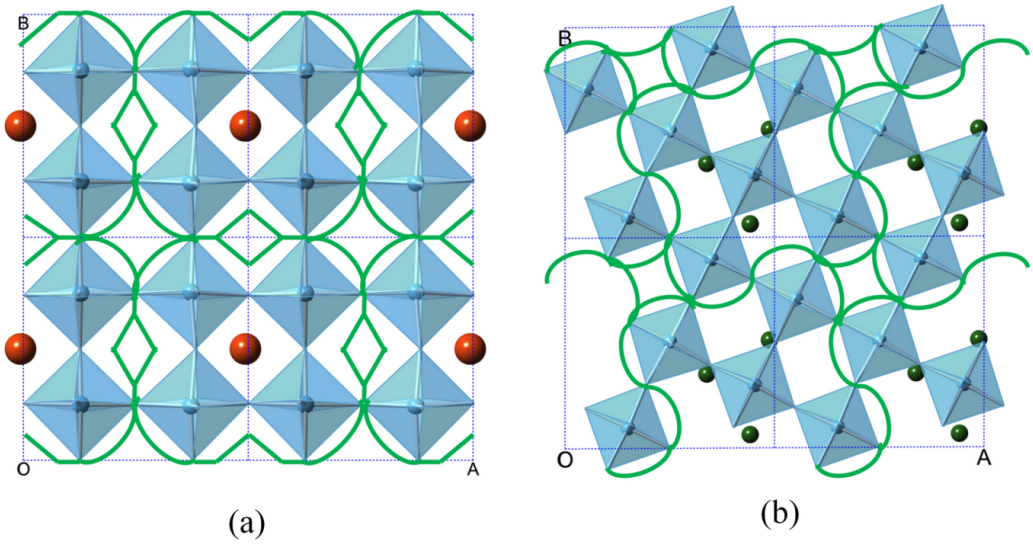

Figure 6.3: Estimated Li diffusion path in La-poor layer (green dash lines) in low lithium concentration scenario (a) and high lithium concentration scenario (b)

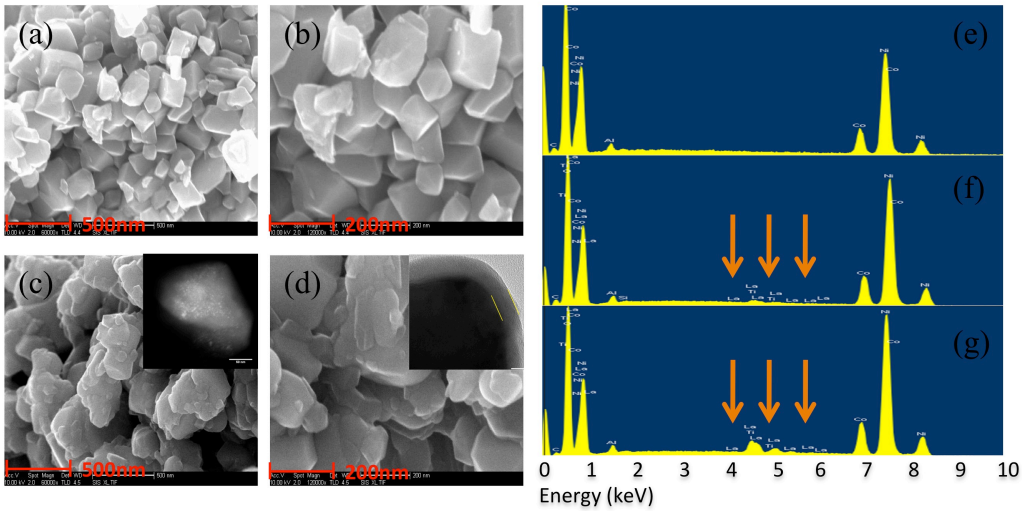

Figure 6.4: Structural characterization of pristine and LLTO coated samples. (a) (b) and (c)(d) are the SEM images of pristine and LLT5, respectively; (e) (f) and (g) are EDS results of pristine, LLT1 and LLT5, respectively. The inset in (c) and (d) is the TEM image of LLT5.

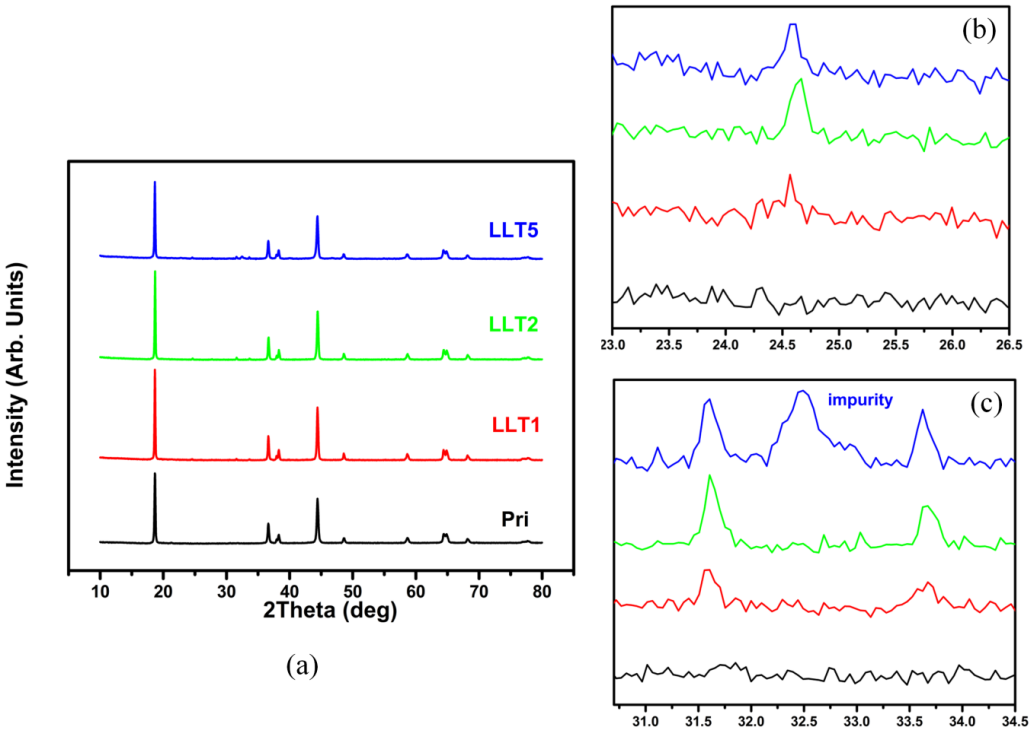

Figure 6.5: (a) XRD results of pristine, LLT1, LLT2, and LLT5. (b) Zoom in of 23° ~ 26.5°. (c) Zoom in of 30.5° ~ 34.5°.

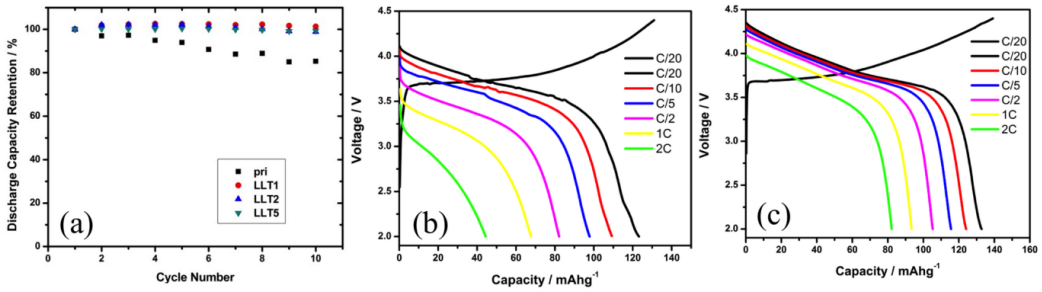

Figure 6.6: Electrochemical cycling and rate capability of pristine and coated electrodes. (a) Cycling retention properties of pristine, LLT1, LLT2 and LLT5. Rate capability of pristine (b) and LLT1 (c).

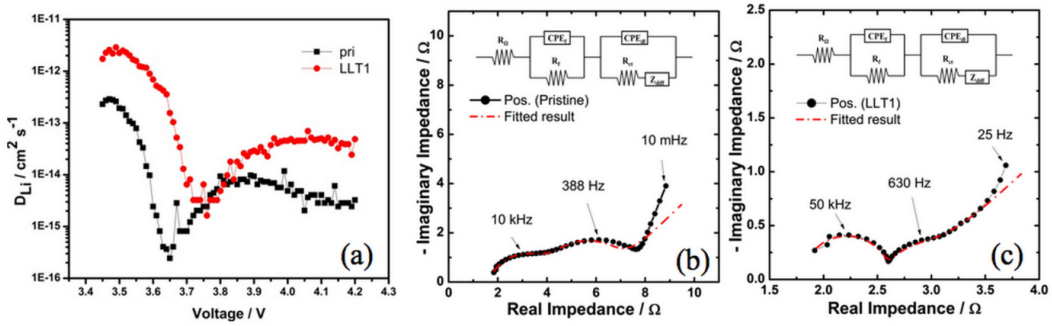

Figure 6.7: (a) Calculated Li ion diffusion coefficient of pristine (black) and LLT1 (red) from PITT tests. Impedance spectra (100kHz – 100mHz) of pristine (b) and LLT1 (c) obtained from the cell at 4.2V. The insets are the equivalent circuit model used to fit the experimental model. Dashed lines are the CNLS fittings of the impedance spectra of the equivalent circuit model.

(a) (b)

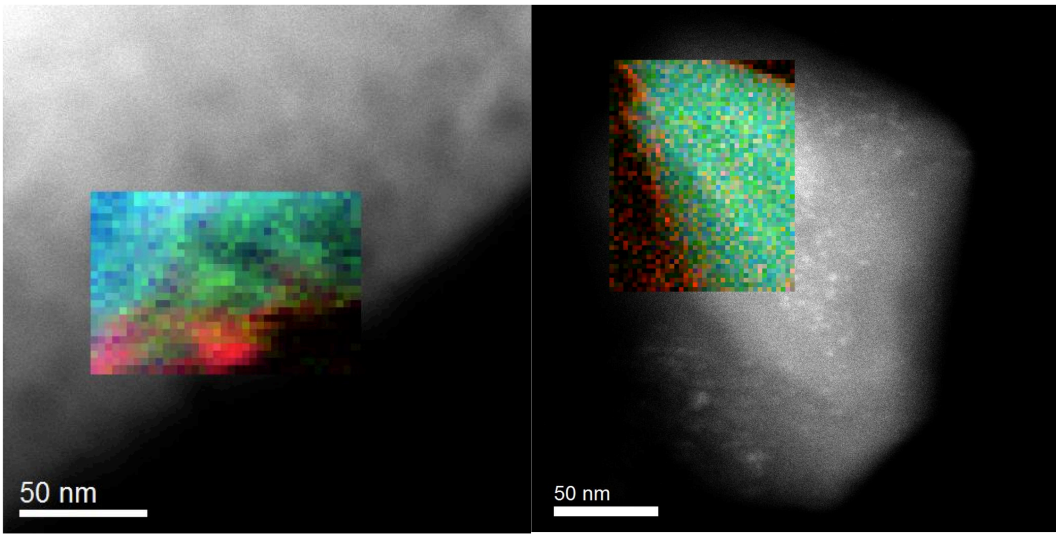

Figure 6.8: EELS mapping of LLT5 (a) before and (b) after cycling. Green: Li; Blue: La; Red: Ti

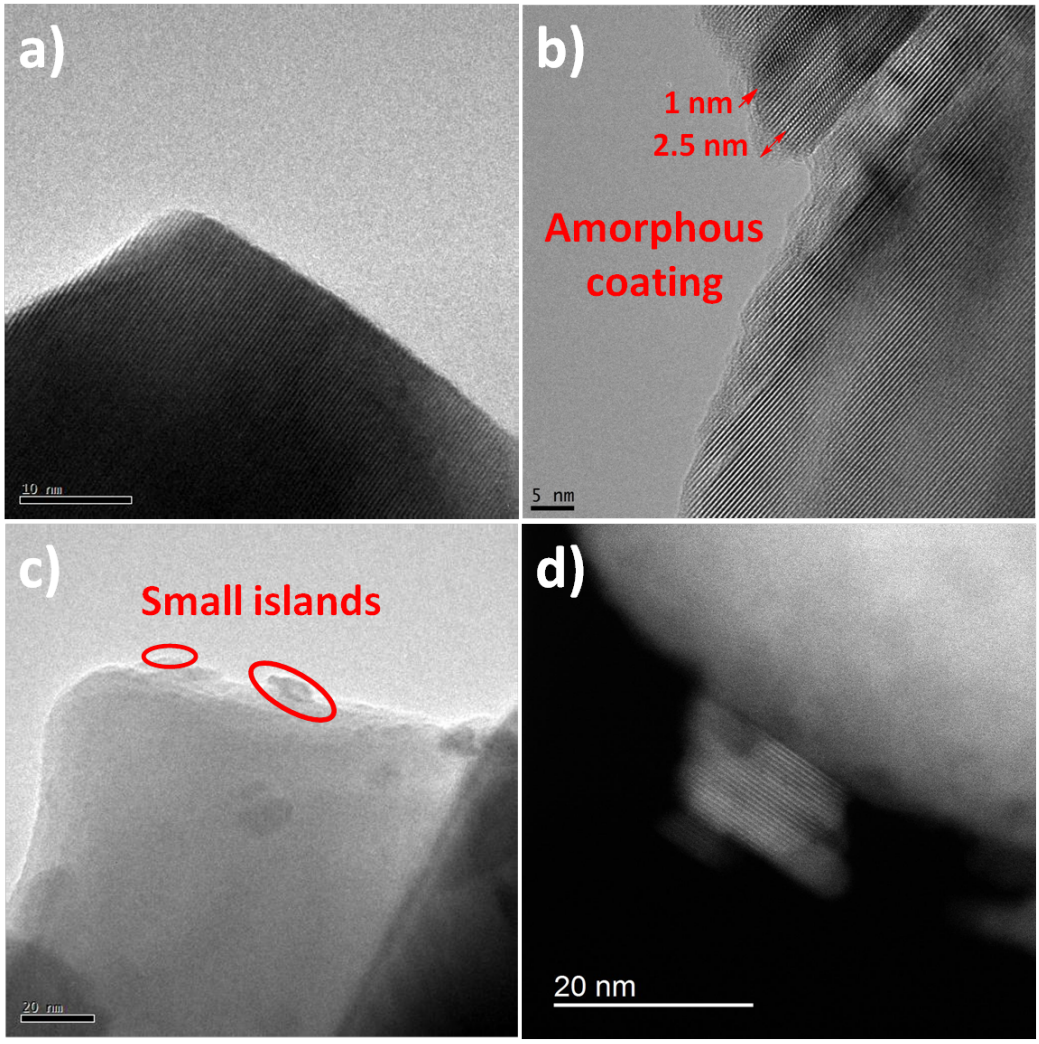

Figure 6.9: The TEM and STEM of LNMO and NALNMO, a) TEM of LNMO, b) and c) TEM of NALNMO, d) STEM of NALNMO.

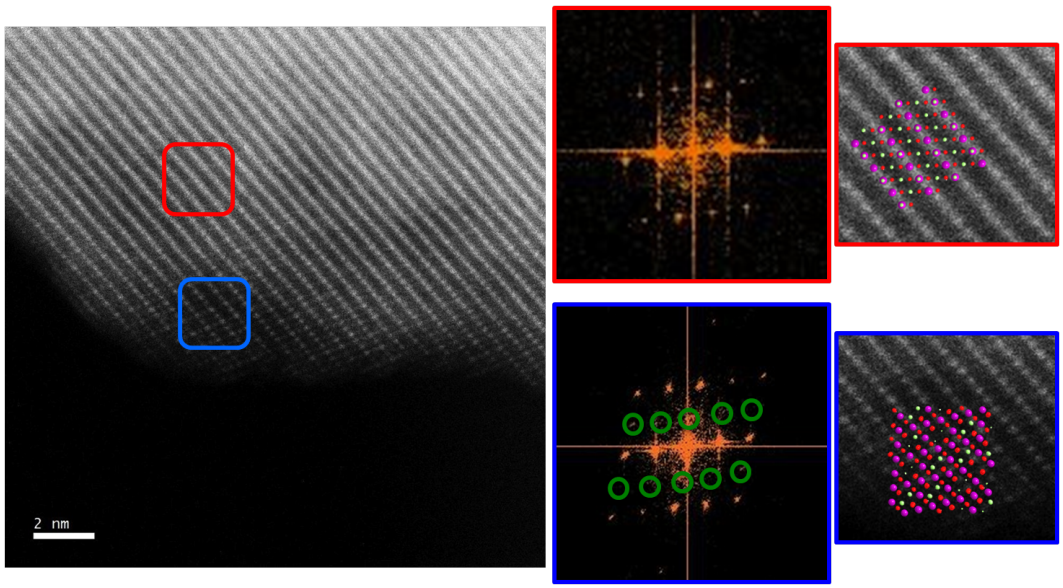

Figure 6.10: High-resolution S/TEM images of the bulk and surface of NALNMO.

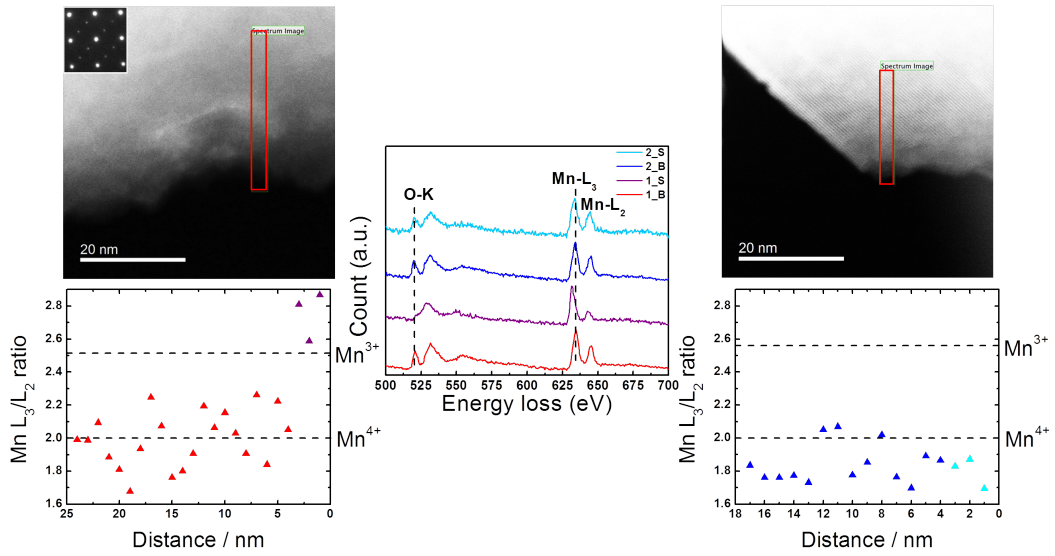

Figure 6.11: The STEM of NALNMO with step scan of Mn EELS L edge and O EELS K edge.

Tables:

Table 6.1: List of the layer sequence of three models and energy values obtained after relaxation

	Layer sequence	**Energies after relaxation (eV)**
Model i	4Li+1 □/ 5La/ 3Li+1La+1 □/ 5La	-822.91028
Model ii	3Li+2 □/ 4La+1Li/ 3Li+2La/ 5La	-822.68657
Model iii	2Li+2La+1 □/ 4La+1Li/ 3Li+1La+1 □/ 4La+1Li	-822.42184

7 STEM/EELS STUDY ON P2-$Na_{2/3}[Fe_{1/3}Mn_{2/3}]O_2$

7.1 Introduction

Lithium ion batteries are receiving intensive attention in the past decade due to the greener transportation demands. Lithium ion batteries exhibit the best performance among all alkaline ion batteries. However, with the increasing market, the limiting resource and high price of the raw material will be the major obstacle. Therefore, sodium ion batteries are making a major return to the center of research due to the cheaper price and broader resources. Sodium, as the second lightest alkaline element next to lithium, is expected to have comparable performances as lithium, enabling them a promising candidate for large-scale applications.

Layered oxides are the most commonly used structures in electrode materials. O3 and P2 structures are the two main groups in sodium ion batteries. O and P represent the sites Na ion resides in, octahedral or prismatic; the number are the repeating layers in the c direction. For example, the P2 type structure, which O forms AABB packing and Na ion resides in prismatic site, delivers higher energy compared to other structures.

Yabuuchi et al. found a new composition of P2-$Na_{2/3}[Fe_{1/2}Mn_{1/2}]O_2$ which can deliver a reversible capacity of 190mAh/g at the voltage window of 1.5V-4.2V with active Fe^{3+}/Fe^{4+} redox, which is comparable to $LiFePO_4$ in lithium ion batteries. In addition, this family of material makes use of earth-abundant elements such as Fe and Mn.

In order to minimize the active Mn^{3+}/Mn^{4+} redox which is associated with Jahn-Teller distortion, a stoichiometry with P2-$Na_{2/3}[Fe_{1/3}Mn_{2/3}]O_2$ was designed. In this study, a systematic STEM/EELS measurement was carried out with pristine, charged and discharged samples. The structure evolution upon cycling as well as the chemical

evolution will be revealed. A better understanding on the reaction mechanism and the optimization process can be engineered.

7.2 Methodology

The compound was synthesized using a solid-state reaction as reported in the previous publication. The phase purity as well as the electrochemical testing protocols is published. The samples tested in this study are pristine, charged to 4.3V and discharged to 1.5V at a rate of 1.2mA/g.

STEM/EELS sample preparation was done by two methods after embedding powders in epoxy resin. One is mechanical grinding, dimpling and polishing the embedded powders to around 40micron thick. This procedure was performed using oil to avoid direct exposure to water. The dimpled specimen was immediately transferred into vacuum chamber of a Fishione 1010 Ion Mill and thinned to electron transparency at a temperature below -100°C. A weak ion beam with 2kV and 3mA was used in the final stage of milling to remove the possible surface damage. The other method is microtoming. A Leica microtome equipped with a gem grade diamond knife to cut thin sections (from 50nm to 100nm). The sections are captured by a normal Cu grid. The as-prepared specimen was stored in vacuum until putting into TEM column for experiment.

The STEM/EELS experiments were performed on an aberration-corrected FEI Titan S 80-300 TEM/STEM with a Gatan Image Filter Quantum-865 operated at 300kV. HAADF-STEM imaging was performed with a probe convergence angle of 30mrad and a large inner collection angle of 65mrad. EELS spectra were collected in STEM mode using a dispersion of 0.25eV per channel and a 5mm aperture.

7.3 Results and Discussions

High resolution HAADF and ABF images were shown in Figure 7.1, with the inset to be the atomic model of the compound P2-$Na_{2/3}[Fe_{1/3}Mn_{2/3}]O_2$. The HAADF image reveals the zone axis to be [010]. With TM (Fe and Mn) being the brighter spots, the layered structure with alternative TM and Na layers is vividly presented. Moreover, from the ABF image in Figure 7.1 (b), the light elements Na and O columns can be distinguishably identified besides the TM columns. Please note that from the HAADF image, the structure is wavy, indicating strain existing in the structure. The wavy characteristics was not observed in any of the LiNiMn cathode materials, possibly due to the mixture of $Fe^{3+/4+}$ and $Mn^{3+/4+}$, both consisting of the Jahn-Teller effect ions Fe^{4+} and Mn^{3+}.

The electron diffraction pattern of the [001] zone axis of pristine is obtained in Figure 7.2 (a). No superstructure diffraction spots present shows the compound does not have any Fe/Mn or Na/vacancy ordering in plane. The superstructure is usually from the ordering of transition metal (TM) oxidation state ordering in the TM layer, which would result in the associated Na/vacancy ordering in the Na layer. The observation is expected due to the mixture of Fe and Mn similar oxidation states. In charged and discharged samples, no superstructure was present during the Na extraction and insertion processes, which is depicted in Figure 7.2 (b) and (c).

A more quantified analysis was done on the EELS of pristine, charged and discharged samples. The L_3 and L_2 edges of transition metals are due to the electronic excitation from the $2p^{3/2}$ to $3d^{3/2}$ and $3d^{5/2}$ orbitals and from the $2p^{1/2}$ to $3d^{3/2}$ orbital, respectively. Previous studies have shown that the L_3/L_2 ratio is sensitive to the valence

state of TM.[165,166] The L_3/L_2 ratio is analyzed and the results are shown in Table 7.1. In pristine material, both Fe and Mn exhibit a mixture of 3+ and 4+. There is 2/3mol of Na in the structure. When charged to 4.3V, all the Mn goes to 4+ leaving a 1/4mol of Na in the structure; while discharged to 1.5V, all the Mn goes to 3+ and there is 1mol of Na. In all the three cases, Fe remains to be a mixture of both 3+ and 4+ but with different portions. In the electrochemical process, all the Mn are active with the 3+ to 4+ redox couple providing 2/3mol of electrons, leaving only ~30% of Fe active.

Even though taking advantage of both redox couples which are earth-abundant elements, as shown in the mechanism, both Mn3+ and Fe4+ have asymmetric e_g electrons, causing severe Jahn-Teller distortion (Figure 7.4). The cyclability of the material can be jeopardized from the distortions. Compared with the literature on the stoichiometry of P2-$Na_{2/3}[Fe_{1/2}Mn_{1/2}]O_2$, our compound showed a better retention upon cycling. The reason may come from the amount of active Fe is smaller in our stoichiometry compared with literature. One possible reason can be that the Mn4+ has higher crystal field stabilization energy than Fe3+.

7.4 Conclusions

P2-$Na_{2/3}[Fe_{1/3}Mn_{2/3}]O_2$ sample was synthesized by a solid state method and investigated using aberration-corrected scanning transmission electron microcopy (STEM) with high-angle annular dark field (HAADF), annular bright field (ABF) and electron energy loss spectroscopy (EELS) techniques. No superstructure was observed for none of the pristine, charged and discharged samples, indicating no ordering for Fe and Mn ions as well as Na ions and vacancies. From the EELS results, both $Fe^{3+/4+}$ and $Mn^{3+/4+}$ are

active during the electrochemical process. Enlightened by the crystal field theory, controlling the percentage of active Fe redox couple would be essential to improve the cyclability and stability of the material during cycling.

Chapter 7, in full, is a reprint of the material "STEM/EELS study of P2-$Na_{2/3}[Fe_{1/3}Mn_{2/3}]O_2$", which is in preparation for submission. The dissertation author is the primary investigator and author.

Figures:

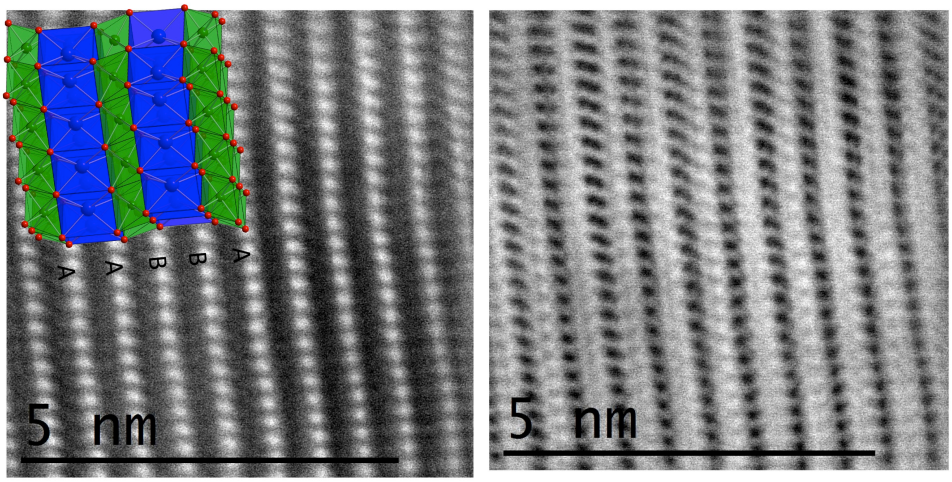

Figure 7.1: HAADF and ABF images of pristine P2-$Na_{2/3}[Fe_{1/3}Mn_{2/3}]O_2$.

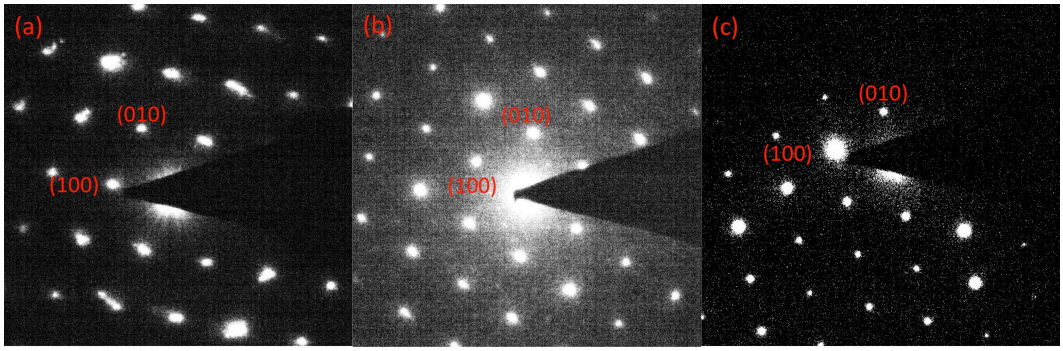

Figure 7.2: ED comparison of pristine, charged and discharged samples.

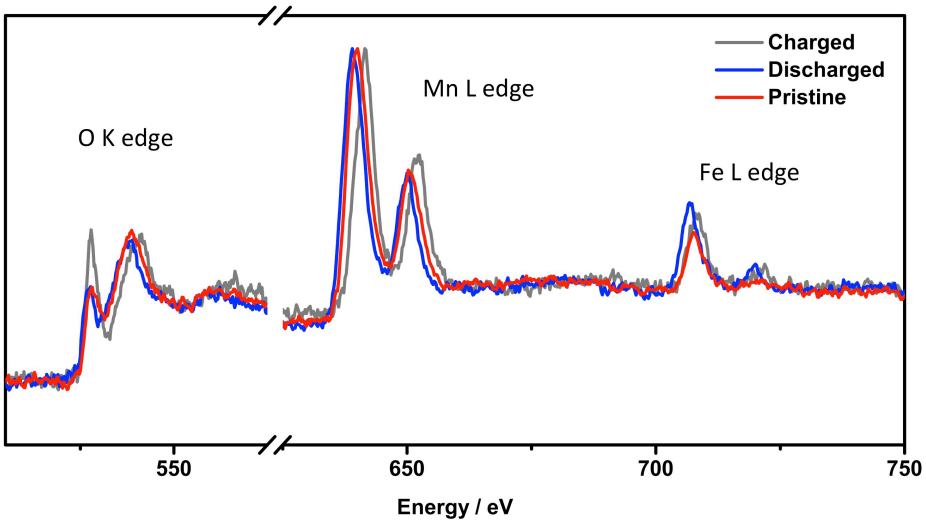

Figure 7.3: EELS spectra comparison of pristine, charged and discharged samples.

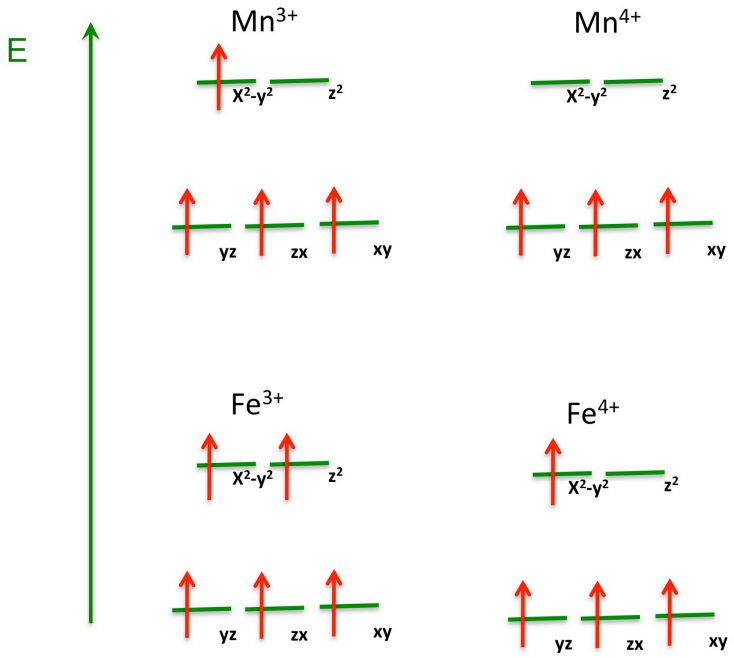

Figure 7.4: Mechanism on the critical role of controlling $Fe^{3+/4+}$ redox couple

Tables:

Table 7.1: EELS quantification of Fe and Mn OS

	Pristine	**Charged**	**Discharged**
Na concentration	2/3	1/4	1
Mn OS	mixture	4+	3+
Fe OS	mixture	mixture	mixture

8 SUMMARY AND FUTURE WORK

8.1 Summary

In this research, a combined approach with both experimental characterizations and first principles calculations is used as the guiding method to understand the surface and interface properties of high-energy high-power cathode materials for AIB system.

In the first part, a surface spin transition phenomenon has been found in LCO using first principles calculations. Different sizes of LCO nanorods have been synthesized and the surface spin transition phenomenon is confirmed applying other characterization techniques including magnetic measurements. This study reveals that the surface electronic properties can be tuned as well as electrochemical properties. The findings shed lights on the controlling of surface magnetic and electronic properties. Consequently, unique magnetic and electronic properties could alter the materials performance in devices, for example, the catalytic process highly depends on the surface electronic properties. OER/ORR measurements were carried out by collaborators in MIT, indicating a much higher activity on the spin-transitioned surfaces.

In the second part, the chemical and structural evolution of Li-excess material during electrochemical cycling has been observed by STEM/EELS. A surface phase transformation from layer to spinel-like accompanied with oxygen vacancy formation has been identified and confirmed. The trend of oxygen vacancy formation versus Li concentration has been carried out computationally. This oxygen vacancy assisted transition metal migration mechanism therefore successfully explained the migration of surface transition metal ions and related phase/structural change nears the material surface.

In the third part, two different coatings have been investigated, one is good ionic conductor LLTO, and the other is AlF_3. The mechanism of the LLTO improved performance has been investigated with multiple techniques. The faster ionic conductivity compensates a new solid-solid interface resistance and results in better rate and cycling performance. It has also been proved that the coating is a continuous effect upon cycling instead of decomposition. STEM/EELS was adopted on the study of AlF_3. Pre-activated Li_2MnO_3 part and small active islands washed away explained the improved electrochemical performance until eighty cycles. These studies help better understanding of the coating mechanisms.

In conclusion, findings in this research has proved a combination of first principles calculations and other high-end characterization techniques provides a throughout understanding of the systems. With the first principles guidance, together adopting sophisticated experimental tools; system optimization can be achieved in a highly efficient way.

8.2 Future work

8.2.1 Surface and interface properties of Na based electrode materials

An alternative to Li chemistry should also be taken into account due to the availability and cost of Li sources. Na chemistry made a major return due to the unlimited sources and cheap prices. The application of Na chemistry would be mainly focused on large-scale application due to the drawbacks on energy densities.

Currently, the cathode materials used in NIB are also intercalation based, and due to the large Na ionic size, P2 (ABBA for the O stacking) framework is the most

commonly used. In the past several years, FeMn, NiMn based P2 as well as Li substituted phases have exhibited excellent performance, comparable to $LiFePO_4$ in LIB. However, there are still urgent needs for mechanism understanding and system optimization in NIB. Similar approaches can be borrowed from LIB.

8.2.2 Computational study on layer/spinel and layer/rocksalt interface

The surface phase transformation has been observed not only in Li-excess family of materials, but also in traditional layered oxides when charging to high voltage. Even though there are still discrepancies on the phase formed, either spinel or rocksalt, a general observation with transition metal migration to Li layer on the surface has been well agreed on. The effect of the spinel/rocksalt surface phase is considered to be an obstruction to the electrochemical performance: blocking the Li diffusion pathway, degrading the voltage profile, poor cycling performance etc.

Understanding the surface phase as well as the interface is essential for either minimizing the negative effect or avoiding the phase transformation. Experimental side, atomic resolution STEM/EELS has been carried out and the chemical information can be obtained. In order to dig deeper into the bonding, electronic properties of the interface, computation is the best approach for atomistic studies.

REFERENCES

(1) Erni, R.; Lazar, S.; Browning, N. D. *Ultramicroscopy* **2008**, *108*, 270.

(2) Haider, M.; Hartel, P.; Muller, H.; Uhlemann, S.; Zach, J. *Philos T R Soc A* **2009**, *367*, 3665.

(3) Kirkland, E. J. *Ultramicroscopy* **2011**, *111*, 1523.

(4) Lupini, A. R.; Krivanek, O. L.; Dellby, N.; Nellist, P. D.; Pennycook, S. J. *Inst Phys Conf Ser* **2001**, 31.

(5) Buban, J. P.; Chi, M. F.; Masiel, D. J.; Bradley, J. P.; Jiang, B.; Stahlberg, H.; Browning, N. D. *J Mater Res* **2009**, *24*, 2191.

(6) Chi, M. F.; Mizoguchi, T.; Martin, L. W.; Bradley, J. P.; Ikeno, H.; Ramesh, R.; Tanaka, I.; Browning, N. *J Appl Phys* **2011**, *110*.

(7) Pennycook, S. J.; Chisholm, M. F.; Lupini, A. R.; Varela, M.; Borisevich, A. Y.; Oxley, M. P.; Luo, W. D.; van Benthem, K.; Oh, S. H.; Sales, D. L.; Molina, S. I.; Garcia-Barriocanal, J.; Leon, C.; Santamaria, J.; Rashkeev, S. N.; Pantelides, S. T. *Philos T R Soc A* **2009**, *367*, 3709.

(8) Shi, X.; Yang, J.; Salvador, J. R.; Chi, M. F.; Cho, J. Y.; Wang, H.; Bai, S. Q.; Yang, J. H.; Zhang, W. Q.; Chen, L. D. *J Am Chem Soc* **2011**, *133*, 7837.

(9) Peng, Y. P.; Nellist, P. D.; Pennycook, S. J. *J Electron Microsc* **2004**, *53*, 257.

(10) Findlay, S. D.; Lugg, N. R.; Shibata, N.; Allen, L. J.; Ikuhara, Y. *Ultramicroscopy* **2011**, *111*, 1144.

(11) Krumeich, F.; Muller, E.; Wepf, R. A. *Micron* **2013**, *49*, 1.

(12) Yu, Z. H.; Muller, D. A.; Silcox, J. *J Appl Phys* **2004**, *95*, 3362.

(13) Egerton, R. F. *Rep Prog Phys* **2009**, *72*.

(14) Krivanek, O. L.; Lovejoy, T. C.; Dellby, N.; Aoki, T.; Carpenter, R. W.; Rez, P.; Soignard, E.; Zhu, J. T.; Batson, P. E.; Lagos, M. J.; Egerton, R. F.; Crozier, P. A. *Nature* **2014**, *514*, 209.

(15) Tang, D. M.; Ren, C. L.; Wang, M. S.; Wei, X. L.; Kawamoto, N.; Liu, C.; Bando, Y.; Mitome, M.; Fukata, N.; Golberg, D. *Nano Lett* **2012**, *12*, 1898.

(16) Shan, Z. W. *Jom-Us* **2012**, *64*, 1229.

(17) Liu, J. Y. *Chemcatchem* **2011**, *3*, 934.

(18) Klein, K. L.; Anderson, I. M.; De Jonge, N. *J Microsc-Oxford* **2011**, *242*, 117.

(19) Park, J.; Zheng, H. M.; Lee, W. C.; Geissler, P. L.; Rabani, E.; Alivisatos, A. P. *Acs Nano* **2012**, *6*, 2078.

(20) Crozier, P. A.; Chenna, S. *Ultramicroscopy* **2011**, *111*, 177.

(21) Chang, H. J.; Kalinin, S. V.; Yang, S.; Yu, P.; Bhattacharya, S.; Wu, P. P.; Balke, N.; Jesse, S.; Chen, L. Q.; Ramesh, R.; Pennycook, S. J.; Borisevich, A. Y. *J Appl Phys* **2011**, *110*.

(22) Yang, Y. C.; Gao, P.; Gaba, S.; Chang, T.; Pan, X. Q.; Lu, W. *Nat Commun* **2012**, *3*.

(23) Zeng, Z.; Liang, W.-I.; Liao, H.-G.; Xin, H. L.; Chu, Y.-H.; Zheng, H. *Nano Lett.* **2014**, *14*, 1745.

(24) Jarvis, K. A.; Deng, Z.; Allard, L. F.; Manthiram, A.; Ferreira, P. J. *Chem. Mater.* **2011**, *23*, 3614.

(25) Jarvis, K. A.; Deng, Z.; Allard, L. F.; Manthiram, A.; Ferreira, P. J. *J. Mater. Chem.* **2012**, *22*, 11550.

(26) Bareño, J.; Balasubramanian, M.; Kang, S. H.; Wen, J. G.; Lei, C. H.; Pol, S. V.; Petrov, I.; Abraham, D. P. *Chemistry of Materials* **2011**, *23*, 2039.

(27) Boulineau, A.; Simonin, L.; Colin, J.-F.; Canévet, E.; Daniel, L.; Patoux, S. *Chem. Mater.* **2012**, *24*, 3558.

(28) Xu, B.; Fell, C. R.; Chi, M.; Meng, Y. S. *Energy & Environmental Science* **2011**, *4*, 2223.

(29) Carroll, K. J.; Qian, D.; Fell, C.; Calvin, S.; Veith, G. M.; Chi, M.; Baggetto, L.; Meng, Y. S. *Physical Chemistry Chemical Physics* **2013**.

(30) Fell, C. R.; Qian, D.; Carroll, K. J.; Chi, M.; Jones, J. L.; Meng, Y. S. *Chem. Mater.* **2013**, *25*, 1621.

(31) Qian, D.; Xu, B.; Chi, M.; Meng, Y. S. *Physical Chemistry Chemical Physics* **2014**, *16*, 14665.

(32) Boulineau, A.; Simonin, L.; Colin, J. F.; Bourbon, C.; Patoux, S. *Nano Lett.* **2013**, *13*, 3857.

(33) Gu, M.; Genc, A.; Belharouak, I.; Wang, D.; Amine, K.; Thevuthasan, S.; Baer, D. R.; Zhang, J.-G.; Browning, N. D.; Liu, J.; Wang, C. *Chem. Mater.* **2013**, *25*, 2319.

(34) Chung, S.-Y.; Choi, S.-Y.; Yamamoto, T.; Ikuhara, Y. *Angewandte Chemie International Edition* **2009**, *48*, 543.

(35) Janssen, Y.; Santhanagopalan, D.; Qian, D.; Chi, M.; Wang, X.; Hoffmann, C.; Meng, Y. S.; Khalifah, P. G. *Chemistry of Materials* **2013**, *25*, 4574.

(36) Lee, J.; Zhou, W.; Idrobo, J. C.; Pennycook, S. J.; Pantelides, S. T. *Physical Review Letters* **2011**, *107*, 085507.

(37) Chen, G. Y.; Song, X. Y.; Richardson, T. J. *Electrochem. Solid State Lett.* **2006**, *9*, A295.

(38) Laffont, L.; Delacourt, C.; Gibot, P.; Wu, M. Y.; Kooyman, P.; Masquelier, C.; Tarascon, J. M. *Chemistry of Materials* **2006**, *18*, 5520.

(39) Ramana, C. V.; Mauger, A.; Gendron, F.; Julien, C. M.; Zaghib, K. *Journal of Power Sources* **2009**, *187*, 555.

(40) Brunetti, G.; Robert, D.; Bayle-Guillemaud, P.; Rouvière, J. L.; Rauch, E. F.; Martin, J. F.; Colin, J. F.; Bertin, F.; Cayron, C. *Chemistry of Materials* **2011**, *23*, 4515.

(41) Wang, F.; Robert, R.; Chernova, N. A.; Pereira, N.; Omenya, F.; Badway, F.; Hua, X.; Ruotolo, M.; Zhang, R.; Wu, L.; Volkov, V.; Su, D.; Key, B.; Whittingham, M. S.; Grey, C. P.; Amatucci, G. G.; Zhu, Y.; Graetz, J. *J. Am. Chem. Soc.* **2011**, *133*, 18828.

(42) Rangan, S.; Thorpe, R.; Bartynski, R. A.; Sina, M.; Cosandey, F.; Celik, O.; Mastrogiovanni, D. D. T. *The Journal of Physical Chemistry C* **2012**, *116*, 10498.

(43) Sina, M.; Nam, K. W.; Su, D.; Pereira, N.; Yang, X. Q.; Amatucci, G. G.; Cosandey, F. *J Mater Chem A* **2013**, *1*, 11629.

(44) Beaulieu, L. Y.; Hewitt, K. C.; Turner, R. L.; Bonakdarpour, A.; Abdo, A. A.; Christensen, L.; Eberman, K. W.; Krause, J. L.; Dahn, J. R. *J Electrochem Soc* **2003**, *150*, A149.

(45) Danet, J.; Brousse, T.; Rasim, K.; Guyomard, D.; Moreau, P. *Phys. Chem. Chem. Phys.* **2010**, *12*, 220.

(46) Gu, M.; Wang, Z.; Connell, J. G.; Perea, D. E.; Lauhon, L. J.; Gao, F.; Wang, C. *ACS Nano* **2013**, *7*, 6303.

(47) Takada, K. *Acta Mater.* **2013**, *61*, 759.

(48) Egerton, R. F.; Li, P.; Malac, M. *Micron* **2004**, *35*, 399.

(49) Buschmann, H.; Dolle, J.; Berendts, S.; Kuhn, A.; Bottke, P.; Wilkening, M.; Heitjans, P.; Senyshyn, A.; Ehrenberg, H.; Lotnyk, A.; Duppel, V.; Kienle, L.; Janek, J. *Phys. Chem. Chem. Phys.* **2011**, *13*, 19378.

(50) Kumazaki, S.; Iriyama, Y.; Kim, K.-H.; Murugan, R.; Tanabe, K.; Yamamoto, K.; Hirayama, T.; Ogumi, Z. *Electrochem. Commun.* **2011**, *13*, 509.

(51) Gao, X.; Fisher, C. A. J.; Kimura, T.; Ikuhara, Y. H.; Kuwabara, A.; Moriwake, H.; Oki, H.; Tojigamori, T.; Kohama, K.; Ikuhara, Y. *J Mater Chem A* **2014**, *2*, 843.

(52) Kim, K. H.; Iriyama, Y.; Yamamoto, K.; Kumazaki, S.; Asaka, T.; Tanabe, K.; Fisher, C. A. J.; Hirayama, T.; Murugan, R.; Ogumi, Z. *J. Power Sources* **2011**, *196*, 764.

(53) Sakuda, A.; Hayashi, A.; Tatsumisago, M. *Chem. Mater.* **2009**, *22*, 949.

(54) Kitaura, H.; Hayashi, A.; Tadanaga, K.; Tatsumisago, M. *J. Electrochem. Soc.* **2010**, *157*, A407.

(55) Ma, C.; Chen, K.; Liang, C.; Nan, C.-W.; Ishikawa, R.; More, K.; Chi, M. *Energy & Environmental Science* **2014**, *7*, 1638.

(56) Ma, C.; Rangasamy, E.; Liang, C.; Sakamoto, J.; More, K. L.; Chi, M. *Angewandte Chemie International Edition* **2014**, n/a.

(57) Liu, X. H.; Zheng, H.; Zhong, L.; Huang, S.; Karki, K.; Zhang, L. Q.; Liu, Y.; Kushima, A.; Liang, W. T.; Wang, J. W.; Cho, J.-H.; Epstein, E.; Dayeh, S. A.; Picraux, S. T.; Zhu, T.; Li, J.; Sullivan, J. P.; Cumings, J.; Wang, C.; Mao, S. X.; Ye, Z. Z.; Zhang, S.; Huang, J. Y. *Nano Lett.* **2011**, *11*, 3312.

(58) Liu, X. H.; Zhong, L.; Huang, S.; Mao, S. X.; Zhu, T.; Huang, J. Y. *ACS Nano* **2012**, *6*, 1522.

(59) Liu, X. H.; Wang, J. W.; Huang, S.; Fan, F.; Huang, X.; Liu, Y.; Krylyuk, S.; Yoo, J.; Dayeh, S. A.; Davydov, A. V.; Mao, S. X.; Picraux, S. T.; Zhang, S.; Li, J.; Zhu, T.; Huang, J. Y. *Nat Nano* **2012**, *7*, 749.

(60) Wang, C. M.; Xu, W.; Liu, J.; Zhang, J. G.; Saraf, L. V.; Arey, B. W.; Choi, D. W.; Yang, Z. G.; Xiao, J.; Thevuthasan, S.; Baer, D. R. *Nano Lett* **2011**, *11*, 1874.

(61) Zhu, Y.; Wang, J. W.; Liu, Y.; Liu, X.; Kushima, A.; Liu, Y.; Xu, Y.; Mao, S. X.; Li, J.; Wang, C.; Huang, J. Y. *Adv. Mater. (Weinheim, Ger.)* **2013**, *25*, 5461.

(62) Wang, F.; Yu, H.-C.; Chen, M.-H.; Wu, L.; Pereira, N.; Thornton, K.; Van der Ven, A.; Zhu, Y.; Amatucci, G. G.; Graetz, J. *Nat Commun* **2012**, *3*, 1201.

(63) Huang, J. Y.; Zhong, L.; Wang, C. M.; Sullivan, J. P.; Xu, W.; Zhang, L. Q.; Mao, S. X.; Hudak, N. S.; Liu, X. H.; Subramanian, A.; Fan, H.; Qi, L.; Kushima, A.; Li, J. *Science* **2010**, *330*, 1515.

(64) Gu, M.; Parent, L. R.; Mehdi, B. L.; Unocic, R. R.; McDowell, M. T.; Sacci, R. L.; Xu, W.; Connell, J. G.; Xu, P.; Abellan, P.; Chen, X.; Zhang, Y.; Perea, D. E.; Evans, J. E.; Lauhon, L. J.; Zhang, J.-G.; Liu, J.; Browning, N. D.; Cui, Y.; Arslan, I.; Wang, C.-M. *Nano Lett.* **2013**, *13*, 6106.

(65) Holtz, M. E.; Yu, Y.; Gunceler, D.; Gao, J.; Sundararaman, R.; Schwarz, K. A.; Arias, T. A.; Abruña, H. D.; Muller, D. A. *Nano Lett.* **2014**, *14*, 1453.

(66) Yamamoto, K.; Iriyama, Y.; Asaka, T.; Hirayama, T.; Fujita, H.; Fisher, C. A. J.; Nonaka, K.; Sugita, Y.; Ogumi, Z. *Angewandte Chemie International Edition* **2010**, *49*, 4414.

(67) Meng, Y. S.; McGilvray, T.; Ming-Che, Y.; Gostovic, D.; Feng, W.; Dongli, Z.; Yintei, Z.; Graetz, J. *Electrochemical Society Interface* **2011**, *20*, 49.

(68) Santhanagopalan, D.; Qian, D.; McGilvray, T.; Wang, Z. Y.; Wang, F.; Camino, F.; Graetz, J.; Dudney, N.; Meng, Y. S. *J Phys Chem Lett* **2014**, *5*, 298.

(69) Okubo, M.; Hosono, E.; Kim, J.; Enomoto, M.; Kojima, N.; Kudo, T.; Zhou, H. S.; Honma, I. *J Am Chem Soc* **2007**, *129*, 7444.

(70) Chen, H.; Grey, C. P. *Advanced Materials* **2008**, *20*, 2206.

(71) Okubo, M.; Kim, J.; Kudo, T.; Zhou, H.; Honma, I. *Journal of Physical Chemistry C* **2009**, *113*, 15337.

(72) Levasseur, S.; Menetrier, M.; Shao-Horn, Y.; Gautier, L.; Audemer, A.; Demazeau, G.; Largeteau, A.; Delmas, C. *Chemistry of Materials* **2003**, *15*, 348.

(73) Kresse, G.; Joubert, D. *Phys. Rev. B: Condens. Matter Mater. Phys.* **1999**, *59*, 1758.

(74) Kresse, G.; Furthmuller, J. *Physical Review B* **1996**, *54*, 11169.

(75) Kresse, G.; Hafner, J. *Phys. Rev. B: Condens. Matter Mater. Phys.* **1994**, *49*, 14251.

(76) Liechtenstein, A. I.; Anisimov, V. I.; Zaanen, J. *Phys. Rev. B: Condens. Matter Mater. Phys.* **1995**, *52*, R5467.

(77) Wang, L.; Maxisch, T.; Ceder, G. *Physical Review B* **2006**, *73*.

(78) Scherrer, P. *Gottinger Nachrichten* **1918**, *2*, 98.

(79) Kramer, D.; Ceder, G. *Chemistry of Materials* **2009**, *21*, 3799.

(80) Daheron, L.; Dedryvere, R.; Martinez, H.; Menetrier, M.; Denage, C.; Delmas, C.; Gonbeau, D. *Chemistry of Materials* **2008**, *20*, 583.

(81) Ohzuku, T.; Makimura, Y. *Chemistry Letters* **2001**, 642.

(82) Daheron, L.; Martinez, H.; Dedryvere, R.; Baraille, I.; Menetrier, M.; Denage, C.; Delmas, C.; Gonbeau, D. *Journal of Physical Chemistry C* **2009**, *113*, 5843.

(83) Carlier, D.; Ménétrier, M.; Grey, C. P.; Delmas, C.; Ceder, G. *Physical Review B* **2003**, *67*, 174103.

(84) Kim, J.; Middlemiss, D. S.; Chernova, N. A.; Zhu, B. Y. X.; Masquelier, C.; Grey, C. P. *J Am Chem Soc* **2010**, *132*, 16825.

(85) Mali, G.; Meden, A.; Dominko, R. *Chemical Communications* **2010**, *46*, 3306.

(86) Kikkawa, S.; Miyazaki, S.; Koizumi, M. *J. Solid State Chem.* **1986**, *62*, 35.

(87) Chen, H.; Wu, L.; Zhang, L.; Zhu, Y.; Grey, C. P. *J Am Chem Soc* **2011**, *133*, 262.

(88) Suntivich, J.; May, K. J.; Gasteiger, H. A.; Goodenough, J. B.; Shao-Horn, Y. *Science* **2011**, *334*, 1383.

(89) Suntivich, J.; Gasteiger, H. A.; Yabuuchi, N.; Nakanishi, H.; Goodenough, J. B.; Shao-Horn, Y. *Nat Chem* **2011**, *3*, 546.

(90) Suntivich, J.; Hong, W. T.; Lee, Y.-L.; Rondinelli, J. M.; Yang, W.; Goodenough, J. B.; Dabrowski, B.; Freeland, J. W.; Shao-Horn, Y. *The Journal of Physical Chemistry C* **2014**, *118*, 1856.

(91) Grimaud, A.; May, K. J.; Carlton, C. E.; Lee, Y.-L.; Risch, M.; Hong, W. T.; Zhou, J.; Shao-Horn, Y. *Nat Commun* **2013**, *4*.

(92) Grimaud, A.; Carlton, C. E.; Risch, M.; Hong, W. T.; May, K. J.; Shao-Horn, Y. *The Journal of Physical Chemistry C* **2013**, *117*, 25926.

(93) Qian, D.; Hinuma, Y.; Chen, H.; Du, L.-S.; Carroll, K. J.; Ceder, G.; Grey, C. P.; Meng, Y. S. *J. Am. Chem. Soc.* **2012**, *134*, 6096.

(94) Ferreira, P. J.; la O', G. J.; Shao-Horn, Y.; Morgan, D.; Makharia, R.; Kocha, S.; Gasteiger, H. A. *J Electrochem Soc* **2005**, *152*, A2256.

(95) Wang, Z. L.; Yin, J. S.; Jiang, Y. D. *Micron* **2000**, *31*, 571.

(96) Yoon, W. S.; Iannopollo, S.; Grey, C. P.; Carlier, D.; Gorman, J.; Reed, J.; Ceder, G. *Electrochemical and Solid State Letters* **2004**, *7*, A167.

(97) Meng, Y. S.; Ceder, G.; Grey, C. P.; Yoon, W. S.; Jiang, M.; Breger, J.; Shao-Horn, Y. *Chemistry of Materials* **2005**, *17*, 2386.

(98) Lu, Z. H.; MacNeil, D. D.; Dahn, J. R. *Electrochemical and Solid State Letters* **2001**, *4*, A191.

(99) Lu, Z. H.; Dahn, J. R. *J. Electrochem. Soc.* **2002**, *149*, A815.

(100) Lei, C. H.; Bareno, J.; Wen, J. G.; Petrov, I.; Kang, S. H.; Abraham, D. P. *Journal of Power Sources* **2008**, *178*, 422.

(101) Fell, C. R.; Carroll, K. J.; Chi, M. F.; Meng, Y. S. *J Electrochem Soc* **2010**, *157*, A1202.

(102) Breger, J.; Jiang, M.; Dupre, N.; Meng, Y. S.; Shao-Horn, Y.; Ceder, G.; Grey, C. P. *J. Solid State Chem.* **2005**, *178*, 2575.

(103) Thackeray, M. M.; Kang, S. H.; Johnson, C. S.; Vaughey, J. T.; Benedek, R.; Hackney, S. A. *Journal of Materials Chemistry* **2007**, *17*, 3112.

(104) Robertson, A. D.; Bruce, P. G. *Electrochemical and Solid State Letters* **2004**, *7*, A294.

(105) Jiang, M.; Key, B.; Meng, Y. S.; Grey, C. P. *Chemistry of Materials* **2009**, *21*, 2733.

(106) Armstrong, A. R.; Holzapfel, M.; Novak, P.; Johnson, C. S.; Kang, S. H.; Thackeray, M. M.; Bruce, P. G. *J. Am. Chem. Soc.* **2006**, *128*, 8694.

(107) Liu, J.; Manthiram, A. *Journal of Materials Chemistry* **2010**, *20*, 3961.

(108) Myung, S. T.; Izumi, K.; Komaba, S.; Sun, Y. K.; Yashiro, H.; Kumagai, N. *Chemistry of Materials* **2005**, *17*, 3695.

(109) Park, B. C.; Kim, H. B.; Myung, S. T.; Amine, K.; Belharouak, I.; Lee, S. M.; Sun, Y. K. *Journal of Power Sources* **2008**, *178*, 826.

(110) Hong, J.; Lim, H. D.; Lee, M.; Kim, S. W.; Kim, H.; Oh, S. T.; Chung, G. C.; Kang, K. *Chemistry of Materials* **2012**, *24*, 2692.

(111) Gu, M.; Belharouak, I.; Genc, A.; Wang, Z. G.; Wang, D. P.; Amine, K.; Gao, F.; Zhou, G. W.; Thevuthasan, S.; Baer, D. R.; Zhang, J. G.; Browning, N. D.; Liu, J.; Wang, C. M. *Nano Lett* **2012**, *12*, 5186.

(112) Xu, B.; Fell, C. R.; Chi, M. F.; Meng, Y. S. *Energy & Environmental Science* **2011**, *4*, 2223.

(113) Fell, C. R.; Chi, M. F.; Meng, Y. S.; Jones, J. L. *Solid State Ionics* **2012**, *207*, 44.

(114) Pennycook, S. J. *Ultramicroscopy* **1989**, *30*, 58.

(115) James, E. M.; Browning, N. D. *Ultramicroscopy* **1999**, *78*, 125.

(116) Kresse, G.; Joubert, D. *Phys Rev B* **1999**, *59*, 1758.

(117) Kresse, G.; Furthmuller, J. *Comp Mater Sci* **1996**, *6*, 15.

(118) Kresse, G.; Hafner, J. *Phys Rev B* **1994**, *49*, 14251.

(119) Perdew, J. P.; Burke, K.; Wang, Y. *Physical Review B* **1996**, *54*, 16533.

(120) Hinuma, Y.; Meng, Y. S.; Kang, K. S.; Ceder, G. *Chem. Mater.* **2007**, *19*, 1790.

(121) Wang, L.; Maxisch, T.; Ceder, G. *Chem. Mater.* **2007**, *19*, 543.

(122) Fell, C. R.; Qian, D.; Carroll, K. J.; Chi, M.; Jones, J.; Meng, Y. S. *Chem. Mater.* **2013**.

(123) Van der Ven, A.; Ceder, G. *Electrochemical and Solid State Letters* **2000**, *3*, 301.

(124) Reed, J.; Ceder, G. *Chemical Reviews* **2004**, *104*, 4513.

(125) Inaguma, Y.; Itoh, M. *Solid State Ionics* **1996**, *86-8*, 257.

(126) Inaguma, Y.; Katsumata, T.; Itoh, M. *Electrochemistry* **2000**, *68*, 534.

(127) Inaguma, Y.; Katsumata, T.; Itoh, M.; Morii, Y. *J. Solid State Chem.* **2002**, *166*, 67.

(128) Inaguma, Y.; Katsumata, T.; Itoh, M.; Morii, Y.; Tsurui, T. *Solid State Ionics* **2006**, *177*, 3037.

(129) Inaguma, Y.; Matsui, Y.; Shan, Y. J.; Itoh, M.; Nakamura, T. *Solid State Ionics* **1995**, *79*, 91.

(130) Stramare, S.; Thangadurai, V.; Weppner, W. *Chem. Mater.* **2003**, *15*, 3974.

(131) Harada, Y.; Hirakoso, Y.; Kawai, H.; Kuwano, J. *Solid State Ionics* **1999**, *121*, 245.

(132) Inaguma, Y.; Chen, L. Q.; Itoh, M.; Nakamura, T.; Uchida, T.; Ikuta, H.; Wakihara, M. *Solid State Commun.* **1993**, *86*, 689.

(133) Lee, J. m.; Kim, S. h.; Tak, Y.; Yoon, Y. S. *J. Power Sources* **2006**, *163*, 173.

(134) Abe, T.; Sagane, F.; Ohtsuka, M.; Iriyama, Y.; Ogumi, Z. *J Electrochem Soc* **2005**, *152*, A2151.

(135) Hara, M.; Nakano, H.; Dokko, K.; Okuda, S.; Kaeriyama, A.; Kanamura, K. *Journal of Power Sources* **2009**, *189*, 485.

(136) Catti, M. *Chem. Mater.* **2007**, *19*, 3963.

(137) Catti, M. *J. Phys. Chem. C* **2008**, *112*, 11068.

(138) Dudarev, S. L.; Botton, G. A.; Savrasov, S. Y.; Humphreys, C. J.; Sutton, A. P. *Phys. Rev. B: Condens. Matter Mater. Phys.* **1998**, *57*, 1505.

(139) Setyawan, W.; Gaume, R. M.; Feigelson, R. S.; Curtarolo, S. *IEEE Trans. Nucl. Sci.* **2009**, *56*, 2989.

(140) Lang, J. K.; Baer, Y.; Cox, P. A. *J. Phys. F: Metal Phys* **1981**, *11*, 121.

(141) Henkelman, G.; Jonsson, H. *J. Chem. Phys.* **2000**, *113*, 9978.

(142) Chowdhury, M. R.; Barnston, A. G.; Guard, C.; Duncan, S.; Schroeder, T. A.; Chu, P. S. *Weather* **2010**, *65*, 263.

(143) Cho, H. M.; Park, Y. J.; Yeon, J. W.; Shin, H. C. *Electron. Mater. Lett.* **2009**, *5*, 169.

(144) Okumura, T.; Ina, T.; Orikasa, Y.; Arai, H.; Uchimoto, Y.; Ogumi, Z. *J. Mater. Chem.* **2011**.

(145) Fourquet, J. L.; Duroy, H.; Crosnier-Lopez, M. P. *J. Solid State Chem.* **1996**, *127*, 283.

(146) Xia, H.; Lu, L.; Ceder, G. *J. Power Sources* **2006**, *159*, 1422.

(147) Barsoukov, E.; Macdonald, J. R. *Impedance spectroscopy : theory, experiment, and applications*; 2nd ed.; Wiley-Interscience: Hoboken, N.J., 2005.

(148) Kang, K. S.; Meng, Y. S.; Breger, J.; Grey, C. P.; Ceder, G. *Science* **2006**, *311*, 977.

(149) Lee, Y. J.; Lee, Y.; Oh, D.; Chen, T.; Ceder, G.; Belcher, A. M. *Nano Lett.* **2010**, *10*, 2433.

(150) Myung, S. T.; Cho, M. H.; Hong, H. T.; Kang, T. H.; Kim, C. S. *J. Power Sources* **2005**, *146*, 222.

(151) Myung, S. T.; Izumi, K.; Komaba, S.; Yashiro, H.; Bang, H. J.; Sun, Y. K.; Kumagai, N. *J. Phys. Chem. C* **2007**, *111*, 4061.

(152) Robertson, A. D.; Bruce, P. G. *Electrochemical and Solid-State Letters* **2004**, *7*, A294.

(153) Zheng, J. M.; Zhang, Z. R.; Wu, X. B.; Dong, Z. X.; Zhu, Z.; Yang, Y. *Journal of The Electrochemical Society* **2008**, *155*, A775.

(154) Wu, Y.; Manthiram, A. *Solid State Ionics* **2009**, *180*, 50.

(155) Zheng, J. M.; Li, J.; Zhang, Z. R.; Guo, X. J.; Yang, Y. *Solid State Ionics* **2008**, *179*, 1794.

(156) Liu, J.; Wang, Q.; Reeja-Jayan, B.; Manthiram, A. *Electrochemistry Communications* **2010**, *12*, 750.

(157) Liu, J.; Reeja-Jayan, B.; Manthiram, A. *J Phys Chem C* **2010**, *114*, 9528.

(158) Martha, S. K.; Nanda, J.; Kim, Y.; Unocic, R. R.; Pannala, S.; Dudney, N. J. *Journal of Materials Chemistry A* **2013**, *1*, 5587.

(159) Fu, Q.; Du, F.; Bian, X.; Wang, Y.; Yan, X.; Zhang, Y.; Zhu, K.; Chen, G.; Wang, C.; Wei, Y. *Journal of Materials Chemistry A* **2014**, *2*, 7555.

(160) Kang, S.-H.; Thackeray, M. M. *Electrochemistry Communications* **2009**, *11*, 748.

(161) Li, J. C.; Baggetto, L.; Martha, S. K.; Veith, G. M.; Nanda, J.; Liang, C. D.; Dudney, N. J. *Adv Energy Mater* **2013**, *3*, 1275.

(162) Kim, I. T.; Knight, J. C.; Celio, H.; Manthiram, A. *Journal of Materials Chemistry A* **2014**.

(163) Kang, S. H.; Thackeray, M. M. *J. Electrochem. Soc.* **2008**, *155*, A269.

(164) Verde, M. G.; Liu, H. D.; Carroll, K. J.; Baggetto, L.; Veith, G. M.; Meng, Y. S. *Acs Appl Mater Inter* **2014**, *6*, 18868.

(165) Kurata, H.; Colliex, C. *Physical Review B* **1993**, *48*, 2102.

(166) Riedl, T.; Gemming, T.; Wetzig, K. *Ultramicroscopy* **2006**, *106*, 284.

(167) Fell, C. R.; Qian, D. N.; Carroll, K. J.; Chi, M. F.; Jones, J. L.; Meng, Y. S. *Chemistry of Materials* **2013**, *25*, 1621.

(168) Carroll, K. J.; Qian, D.; Fell, C.; Calvin, S.; Veith, G. M.; Chi, M. F.; Baggetto, L.; Meng, Y. S. *Physical Chemistry Chemical Physics* **2013**, *15*, 11128.